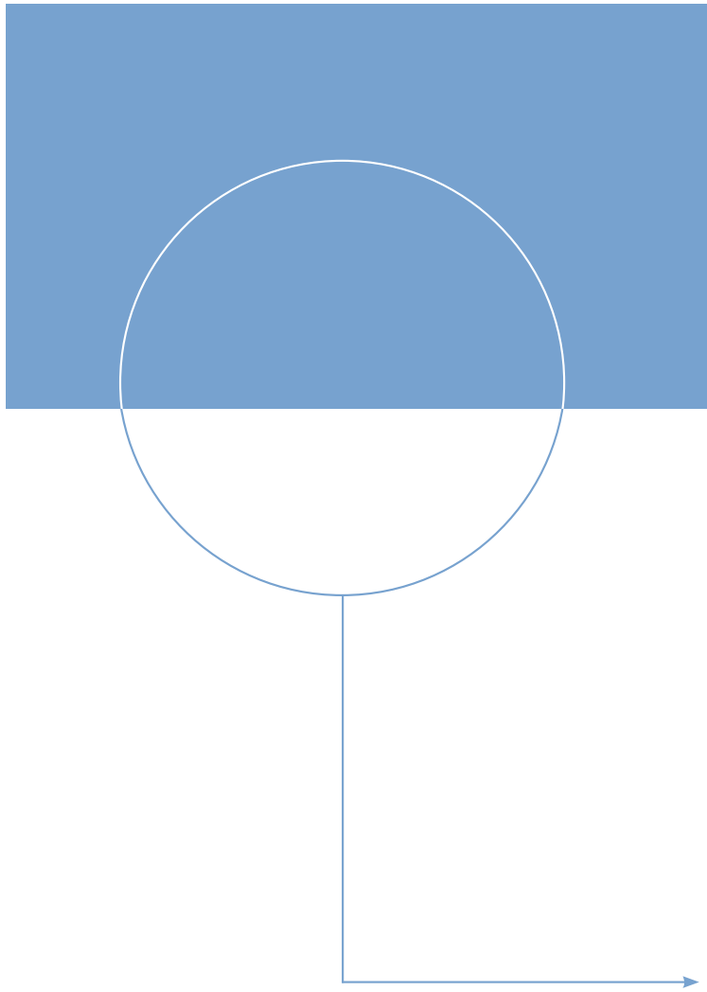

Master's thesis

2021

Gine Kirkebøen Støren

NTNU
Norwegian University of
Science and Technology
Faculty of Engineering
Department of Energy and Process Engineering

Gine Kirkebøen Støren

Signature investigation of typical faults on a Francis turbine

February 2021

NTNU
Norwegian University of
Science and Technology

NTNU
Norwegian University of
Science and Technology

NTNU

Norwegian University of
Science and Technology

Signature investigation of typical faults on a Francis turbine

Gine Kirkebøen Støren

Energy and Environmental Engineering
Submission date: February 2021
Supervisor: Ole Gunnar Dahlhaug
Co-supervisor: Bjørn Winther Solemslie
Ingrid Vilberg

Norwegian University of Science and Technology
Department of Energy and Process Engineering

Norges teknisk-
naturvitenskapelige universitet
NTNU

Fakultet for ingeniørvitenskap
Institutt for energi- og prosessteknikk

NTNU

EPT-P-2020

MASTEROPPGAVE
for
Gine Kirkebøen Støren
Høst 2020

Identifisering av typiske feil på en Francis turbin
Signature investigation of typical faults on a Francis turbine

Bakgrunn
De fleste store vannkraftverk ble bygget i perioden 1950 til 1990 og turbinene begynner i dag å vise tretthets symptomer blant annet gjennom sprekkdannelser i løpehjul. Turbinene har i tillegg blitt operert mer fleksibelt i senere tid og større variasjoner er ventet i fremtiden. Denne fleksible operasjonen av turbinene byr på driftstekniske problemer og høyere risiko for skader og havari. Dagens rutiner for å avdekke skader er gjennom visuelle inspeksjoner under stopp av aggregatet og ved å gjennomføre NDT-prøver på spesielle deler av løpehjulet. Det benyttes ingen måleteknikk for å identifisere dannelse av skader under drift. Dersom ulike feilmekanismer kan detekteres på et tidlig tidspunkt vil mulige havarier kunne unngås og en mer optimal planlegging av vedlikehold og oppgraderingsprosjekter gjennomføres.

Målsetting
Undersøke hvordan typiske feilmekanismer kan identifiseres med tilgjengelige målinger på Francis løpehjulet på Vannkraftlaboratoriet.

Oppgaven bearbeides ut fra følgende punkter:

1. Litteraturstudie
   a. Feilmekanismer på en Francisturbin
   b. Aktuelle måleteknologier og metoder for feildeteksjon
2. Software
   a. Labview skal benyttes for målinger i laboratoriet
   b. Matlab skal benyttes til evaluering av resultater
3. Forberedelser i laboratoriet
   a. Statisk og dynamisk kalibrering for instrumentene som skal brukes i test-riggen
   b. Modellturbin blir instrumentert med trykk-, vibrasjon- og lydsensorer
4. Målinger på Vannkraftlaboratoriet
   a. Gjennomføre målinger på modellturbin i normal og skadet tilstand
   b. Evaluering av måleresultater
   c. Gjennomføre prosedyren flere ganger under en tenkt naturlig utvikling av skaden(e)

---- " ---

Belastningen på prosjektet utgjør 30 studiepoeng.

Besvarelsen redigeres mest mulig som en forskningsrapport med innholdsfortegnelse, et sammendrag på norsk, konklusjon, litteraturliste, etc. Ved utarbeidelsen av teksten skal kandidaten legge vekt på å gjøre teksten oversiktlig og velskrevet. Med henblikk på lesing av besvarelsen er det viktig at de nødvendige henvisninger for korresponderende steder i tekst, tabeller og figurer anføres på begge steder. Ved bedømmelsen legges det stor vekt på at resultatene er grundig bearbeidet, og at de oppstilles tabellarisk og/eller grafisk på en oversiktlig måte og diskuteres utførlig.

Det forutsettes at kandidaten på eget initiativ etablerer et tilfredsstillende kontaktforhold med faglærer og eventuelle veileder(e).

Risikovurdering av kandidatens arbeid skal gjennomføres i henhold til instituttets prosedyrer. Risikovurderingen skal dokumenteres og inngå som del av besvarelsen. Hendelser relatert til kandidatens arbeid med uheldig innvirkning på helse, miljø eller sikkerhet, skal dokumenteres og inngå som en del av besvarelsen. Hvis dokumentasjonen på risikovurderingen utgjør veldig mange sider, leveres den fulle versjonen elektronisk til veileder og et utdrag inkluderes i besvarelsen.

I henhold til "Utfyllende regler til studieforskriften for teknologistudiet/sivilingeniørstudiet" ved NTNU § 20, forbeholder instituttet seg retten til å benytte alle resultater og data til undervisnings- og forskningsformål, samt til fremtidige publikasjoner.

Leveringsfrist: 22 Januar 2021

☒ Arbeid i Vannkraftlaboratoriet
☐ Feltarbeid

Institutt for energi- og prosessteknikk, 28. August 2020

Ole Gunnar Dahlhaug
Faglærer/veileder

Medveiledere: Bjørn Winther Solemslie
Ingrid Vilberg

Preface

This thesis is a result of the author's work as a master student at the Waterpower Laboratory, Department of Energy and Process Engineering (EPT) at the Norwegian University of Science and Technology (NTNU) in Trondheim, Norway. The necessary resources for this project have been financed by HydroCen, the Norwegian Research Centre for Hydropower Technology.

Gine Kirkebøen Støren

Gine Kirkebøen Støren
Trondheim, January 2021

Abstract

The recent entry of intermittent energy sources on the grid in the regime of a market-driven electricity production, necessitates new operational strategies for hydropower production. Hydraulic turbines are more frequently being operated outside their optimal operating range, with rapid load changes and more starts and stops. The flexible pattern of operation, exposes the turbine to higher dynamic loads and increases the risk of fatigue damage. Especially fatigue crack growth is a concern for Francis runners, and both new and old runners have experienced problems related to this the past years. However, it is challenging to detect cracks during operation with the current monitoring system, based on measuring vibrations of stationary parts. Hence, routine inspections during production stop often reveal cracks of critical sizes, which are costly to repair and require additional downtime. New methods for monitoring the appearance of cracks during operation are therefore of interest.

This thesis has investigated how a typical fault occurring on a Francis model runner can be identified during operation. The measurements have been performed on the Francis turbine test rig at the Waterpower Laboratory at NTNU. A crack was manually created on the trailing edge of one runner blade, in the t-joint between the blade and the shroud. To simulate a real situation of a fatigue crack growth, the crack length was extended in stages following a semi-elliptical path, and resulted in a fully realised shark-bite shaped fragment being cut out of the blade. The turbine was instrumented with several pressure sensors and accelerometers, and steady-state measurements were conducted for different operating points and heads between each stage. By analysing the data in the time and frequency domains, the changes in pressure and vibration signatures with crack development were investigated.

The results revealed a change in the pressure signature after the fragment was

detached from the blade. In the time series, a local reduction in static pressure occurred for each runner revolution, in accordance with the damaged blade. The pressure reduction increased with higher loads, but remained unaffected by the head. A combination of local flow effects in the channel and a redistribution of the loads of the damaged blade, is believed to be the cause. In the frequency spectra, a rapid increase in the amplitude of the rotational frequency occurred, probably a consequence of a hydraulic imbalance caused by the damaged runner. The vibration sensors did not capture any change in overall vibration levels, whereas in the frequency spectra, an increase in side-bands around the blade passing frequency occurred. Neither the pressure nor the vibration sensors measured any obvious changes during the crack growth, before the fragment was detached.

Based on the observed results, the transferability to a prototype has been discussed.

Sammendrag

En økende mengde ikke-regulerbare energikilder på strømnettet og høy priskonkurranse på elektrisitet, har ført til endrede driftsstrategier for vannkraftverk de siste årene. Vannturbiner opereres i større grad utenfor deres beste driftspunkt, med raske lastendringer og hyppigere stanser og oppstarter. Dette utsetter turbinene for større dynamiske belastninger og øker risikoen for utmattingskader og havari. Spesielt Francisløpehjul har utfordringer knyttet til dette hvor både nye og eldre løpehjul har begynt å vise tegn på tretthetssymptomer, i hovedsak gjennom sprekkdannelse. Det er utfordrende med dagens overvåkningssystem å identifisere sprekker på løpehjul under drift, og større sprekkdannelser blir derfor oftere avslørt under rutineinspeksjoner ved stans, som krever tid og betydelige økonomiske ressurser å reparere. Metoder for å overvåke sprekkdannelse under drift er derfor av økende interesse.

I denne oppgaven har det blitt undersøkt hvordan en typisk feilmekanisme på et Francis modell løpehjul kan identifiseres ved hjelp av målinger under drift. Testene har blitt utført på Francisriggen på Vannkraftlaboratoriet på NTNU. En tenkt realistisk sprekk har blitt gjenskapt manuelt på avløpskanten på et av bladene, i krysset mellom ringen og kanten. Sprekklengden økte i flere steg, langs en semi-elliptisk kurve innover i bladet, og resulterte i et løsrevet bruddstykke. Trykksensorer og akselerometre ble installert på turbinen, og stasjonære målinger for ulike driftspunkt og ulike fallhøyder ble gjennomført for hvert steg. Ved å analysere dataen i tid og frekvensdomenet ble det undersøkt hvordan trykk- og vibrasjonssignaturene endret seg med sprekkutviklingen.

Resultatene avslørte en endring i trykksignaturen etter at bruddstykket ble fjernet. I tidssignalet ble det observert en lokal trykkreduksjon for hver løpehjulsrotasjon sammenlignet med tidligere sprekksteg. Trykkreduksjonen viste seg å øke med driftspunkt, men forble uendret med økende fallhøyde. En kombinasjon av

lokale strømningseffekter i kanalen, og en omfordeling av belastningene på det ødelagte bladet, antas å være årsaken. Fra frekvensanalysen ble det observert en tydelig økning i amplituden til rotasjonsfrekvensen, trolig som følge av en økt hydraulisk ubalanse skapt av det ødelagte bladet. I vibrasjonssignaturen ble det identifisert en økning i sidebånd rundt bladpasseringsfrekvensen. Hverken trykk eller vibrasjonssensorene målte noen tydelige endringer under selve sprekkdannelsen før bruddstykket ble fjernet.

Basert på de observerte resultatene har overførbarheten til prototyper blitt diskutert.

Acknowledgements

For an energy engineering student with a passion for hydropower, the project has been very engaging, and I look back on an exciting and challenging semester. The combination of practical and theoretical work has given me valuable knowledge and experiences for future work. However, I would never have accomplished this work without the assistance and contribution of a number of people and I take this opportunity to gratefully acknowledge them.

First of all, I am very grateful for my supervisors Ole Gunnar Dahlhaug, Bjørn W. Solemslie and Ingrid Vilberg, for valuable discussions and their belief in this project. You have all encouraged me and given me support during the project. I would especially like to thank Bjørn, for his contribution on so many levels in this project, always providing understanding and guidance to all my questions. This work could never have been done without you, and I wish you all the best of luck in your new job.

I would never have accomplished the practical part of this work without the enormous assistance from the technicians in the laboratory. Halvor Haukvik, Trygve Opland and Joar Grilstad, you have all played special parts of my project, and I am deeply grateful for your clever and creative technical solutions.

I am grateful to Magne Tveit Bolstad for helping me with the 3D-drawings of the cutting-templates, which was fundamental for the progressing of the project. I would also like to thank associate professor Chiraq Trivedi and PhD Igor Iliev for sharing their clever thoughts and ideas on this project.

A big thank you to all the students and academic staff at the Waterpower Laboratory who have contributed to the friendly and inclusive working environment. A special thanks to PhD candidate Johannes Kverno and research assistant Jan-Karl Escher for spending hours with me in the lab during measurements and for fruitful

discussions.

Finally, I am deeply thankful for the support from my family and friends, and especially Thomas. Thank you for your endless patience and inspiration.

Contents

List of Tables

List of Figures

List of Symbols

Latin Symbols

A	Area	m^2
B	Shape factor	$-$
c	Absolute velocity	m/s
c_m	Meridionial velocity component	m/s
c_u	Tangential velocity component	m/s
D	Runner outlet diameter	m^2
E	Specific energy	J/kg
e_i	Absolute uncertainty	$-$
f	Frequency	Hz
f_{bp}	Blade passing frequency	Hz
f_{gv}	Guide vane frequency	Hz
f_i	Relative uncertainty	$\%$
f_{max}	Highest frequency in the signal	Hz
f_n	Rotational frequency	Hz
f_{re}	Rheingans frequency	Hz
f_{res}	Resolution frequency	Hz

f_{vs}	Vortex shedding frequency	Hz
F_s	Sampling frequency	Hz
g	Acceleration of gravity	m/s^2
H	Head	m
j	Harmonic number	$-$
m	Harmonic number	$-$
N	Number of samples	$-$
N_{ed}	Speed factor	$-$
n	Rotational speed	rad/s
p	Pressure	Pa
Pw	Power	W
p_{atm}	Atmospheric pressure	Pa
$\overline{p}$	Average pressure	Pa
$\tilde{p}_E$	Fluctuating pressure as percentage of specific energy	$\%$
Q	Volume flow	m^3/s
Q_{ed}	Discharge factor	$-$
Re	Reynolds number	$-$
St	Strouhaul Number	$-$
S_x	Standard deviation	$-$
t	Blade thickness	mm
$t_{\alpha/2}$	Student t-value	$-$
u	Peripheral velocity	m/s
w	Relative velocity	m/s
$\bar{x}$	Mean value	$-$
x_i	Measured value	$-$

z_{gv}	Number of guide vanes	$-$
z_r	Number of runner blades	$-$

Greek Symbols

α	Significance level	$-$
β	Outlet angle	$^\circ$
ε	Strain	$-$
η_h	Hydraulic efficiency	$-$
π	Constant	$-$
ρ	Density	kg/m^3
σ	Stress	MPa
σ_u	Ultimate tensile strength	N/m^2
σ_y	Yield strength	N/m^2
τ_f	Friction torque	Nm
τ_g	Generator torque	Nm
ω	Angular velocity	rad/s

Abbreviation

BEP	Best Efficiency Point
CFD	Computational Fluid Dynamics
DAQ	Data Acquisition
DC	Direct Current
DFT	Discrete Fourier Transform
DPL	Deep Part Load
DT	Draft Tube
FFT	Fast Fourier Transform
FL	Full Load

GV Guide Vane

HL High Load

IEC International Electrotechnical Commission

LE Leading Edge

ND Nodal Diameter

NTNU Norwegian University of Science and Technology

PL Part Load

RPM Revolutions Per Minute

RSI Rotor Stator Interaction

RSS Root-Sum-Square

SCADA Supervisory Control and Data Acquisition

TE Trailing Edge

Chapter I

Introduction

1.1 Background

A continuously evolving energy market necessitates new operational strategies for hydropower production. Traditionally, hydropower plants have been operated close to their design conditions, providing steady operation and high efficiency [15]. With the comprehensive entry of intermittent renewable energy sources, such as solar and wind, into the electrical grid, there is an increasing need for flexible energy sources to stabilize the grid frequency. Hydropower has the advantageous of being a robust power supply with short response time. As a result, hydropower plants are more frequently being used to balance the sudden changes in the energy production [8, 16, 17]. At the same time, significant variations in the electricity prices encourage power companies to maximize production when the prices are high, leading to an increased peak load production [18]. Hence, today's operating regime is more flexible than before, characterized by more frequent starts and stops and sudden load changes.

Variable operation outside design conditions, exposes turbine runners to high dynamic loads and fatigue damage. At the same time, there is an increased focus on producing thinner and more lightweight runner blades to achieve higher efficiency and reduce costs [8]. However, these are more susceptible to deterioration under higher stresses. Especially fatigue crack growth is a concern for Francis runners, and several cases in both new and old runners have been reported the past years [9, 10, 19–23]. If a crack is not detected in time, it may cause severe damage to the whole machine.

Monitoring systems are normally installed in hydropower plants to ensure safe operation of the machine and to detect possible failures during operation [16]. Generally, monitoring is done by measuring temperatures and vibrations in the

stationary parts, with alarms based on critical thresholds. However, the effect of crack growth can be difficult to identify with the current monitoring system, even for more severe damages [19, 24]. As a consequence, routine inspections during stop often reveal cracks of critical sizes, which require additional downtime and are costly to repair [9]. It is therefore relevant to investigate methods for detecting damages and crack formation on a runner during operation with extended measurements. Such methods could contribute to optimize maintenance planning and reduce the need for downtime.

1.2 Objectives

This work will investigate how a typical fault on the Francis-99 model runner can be identified from experimental measurements during operation.

To obtain the objective, a crack will manually be created on the trailing edge of one runner blade, in the t-joint between the blade and the shroud. To simulate a real situation of fatigue crack growth, the crack length will be extended in several stages along a semi-elliptical path, finally resulting in a detached shark-bite shaped fragment. To acquire data, the turbine will be instrumented with accelerometers and pressure sensors, and measurements will be conducted during each stage. From analysing the measurements in the time and frequency domains, the pressure and vibration signatures during the crack growth will be investigated. Based on this, the following questions will be discussed to evaluate the applicability of the findings, and to further understand the behaviour of a turbine when damaged:

- At what stage in the crack growth can it be identified?
- Which physical parameter measured at what location on the turbine is most sensitive to the crack growth?
- How can physical phenomena be related to the characteristic signatures?

1.3 Previous and ongoing work

Significant work has been carried out in the area of on-line fault detection on rotating machinery, but investigations on hydraulic turbines are rather limited [25]. Part of this may be because hydropower components are characterized by unique designs, high reliability and long lifetime, which results in a lack of sufficient fault data and knowledge of fault modes to develop models for fault detection [26]. However, the extended use of digital systems in the hydropower industry in recent years and innovation projects, such as Monitor X, has put this on the

agenda and highlighted the economic and technical benefits of early detection of faults [27]. A review by Støren et al. presents current methods for on-line fault detection on hydropower components ranging from physical models to more advanced data-driven methods based on artificial intelligence and machine learning [28]. Common to these methods, is that they are based on the normal behaviour of the system, where real measured values are continuously being compared and deviations are identified. Valentin et al. experimentally investigated the detection of different hydraulic phenomena occurring on a Francis turbine with an extended use of sensors, ranging from accelerometers, pressure sensors, microphones and strain gauges [16]. The results demonstrated how monitoring systems could easily be improved with convenient sensors, locations and analysing techniques.

The dynamic behaviour of Francis turbines has been widely studied, and the understanding of how dynamic loads affect the performance of Francis runners has been improved the past decades [4, 8, 15, 29]. However, these studies are normally focusing on the intact runner, and studies of the dynamic behaviour when it comes to cracks or other damages are limited. Zhang et al. numerically investigated the change in dynamical behaviour of a Francis runner suffering from a crack [30]. By creating a crack on one blade, the changes in modal behaviour and force responses with increasing crack-length were evaluated, by exciting different frequencies. The analysis revealed only small deviations in natural frequencies for different crack lengths, which resulted in limited force responses to be captured by the artificial monitoring system. Similar observations were found by Georgievskaia, who numerically simulated a crack on a Francis runner blade and found that only negligible changes in natural frequencies and dynamic behaviour of the blade occurred during the crack development, because of high structural rigidity of the turbine [31].

Several failure investigations on prototypes have indicated challenges with crack monitoring on runner blades. Zhang et al. conducted a failure investigation on a Francis turbine after the monitoring system captured a sudden increase in vibrations [19]. During the investigation, a crack of critical size was identified. A similar result was found in a failure investigation reported by Egusquiza et al., where a crack developed through the runner blade and caused a part to break off during operation before the monitoring system detected a change [22]. Egusquiza et al. analysed vibration monitoring data from 15 years of a Francis turbine suffering from crack growth, and only small changes in the monitoring system were observed [24]. Generally, when the crack is of a critical size or has caused part of the blade to break off, the monitoring system identifies an increase in the overall vibration levels. However, during the crack formation, the runner vibrations are normally too small to produce substantial deformations that can be captured by the traditional monitoring system.

Chapter II

Theoretical Background

■ This chapter is divided into five main sections and presents the main concepts that will be discussed in the thesis. Section 2.1.1, 2.2 and 2.4 are based on the author's specialisation project "Analytics of data from hydropower turbines for anomality and condition predictions" [32], with minor alterations.

2.1 Francis turbines

The Francis turbine is the most commonly used turbine due to its high efficiency and wide range of application, ranging from heads from 30 m to 700 m [33]. The hydraulic energy from the flowing water is transferred into mechanical torque on the shaft through the runner, combining a radial inflow with an axial outflow [34]. The Francis turbine is a reaction turbine, where both kinetic and potential energy is extracted from the water. Firstly, the change in direction of the water flow trough the channels between the runner blades, transfer impulse forces [35]. Secondly, the pressure decreases gradually as the water flows from the inlet to the outlet of the runner, and the runner is therefore completely filled with water. Apart from the runner, several other components are essential to support the energy conversion.

A typical Francis turbine with its main components is shown in Figure 2.1. The water flows from the penstock into a **spiral casing**, that distributes the water evenly around the circumference. The flow is then deflected by fixed **stay vanes**, followed by adjustable **guide vanes**, which can open and close to control the flow and ensure the correct angle towards the runner blades. In the **runner**, the total energy extraction occurs which is transferred to the rotating **shaft**. From the runner outlet the flow enters the **draft tube**, which connects the runner to the tailrace and converts

the remaining kinetic energy in the water into pressure energy.

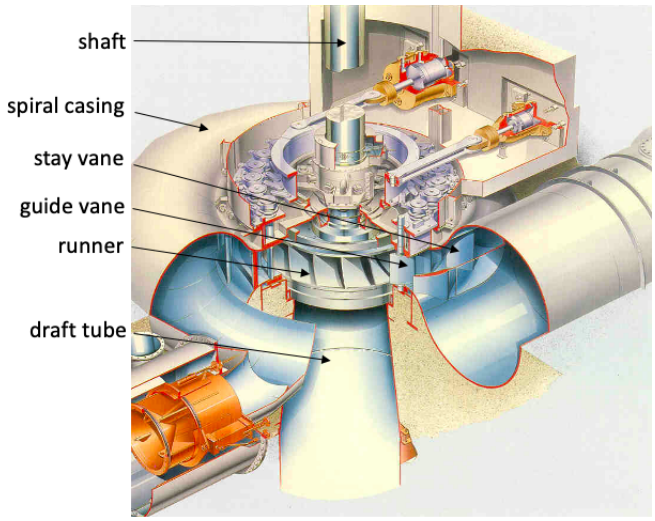

Figure 2.1: Illustration of a typical Francis turbine with its main components (Source: Kværner Energy AS)

A Francis runner consist of a hub, a shroud and several blades connecting them. A section view of the Francis-99 model runner is shown in Figure 2.2. The runner is of splitter blade design, consisting of blades of full and half length. The blades' cross-sections are shaped like thin air-foils, so when water flows over, a low pressure side will be produced on one side, denoted the suction side (SS), and a high pressure side on other, denoted the pressure side (PS).

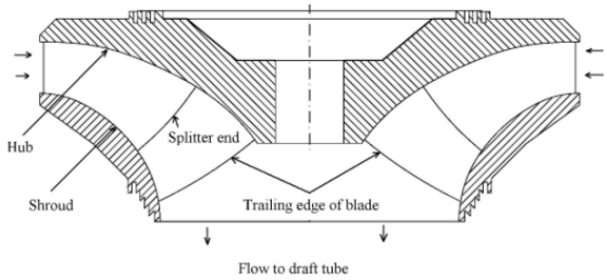

Figure 2.2: Section view of the Francis-99 model runner [2]

2.1.1 Turbine performance and hill-diagram

A hill-diagram shows the performance of a model turbine over the whole theoretical operating range [3]. Figure 2.3 illustrates a typical hill-diagram for a Francis model turbine. Constant isolines of hydraulic efficiency are shown for different discharge and speed ranges, and the horizontal lines denoted with α are constant guide vane openings. By using reduced scales of discharge, Q_{ed}, and speed, N_{ed}, one can compare similar geometrical turbines, i.e. transpose from model to prototype. The grey area in the figure indicates where the producer is guaranteed to operate the turbine safely.

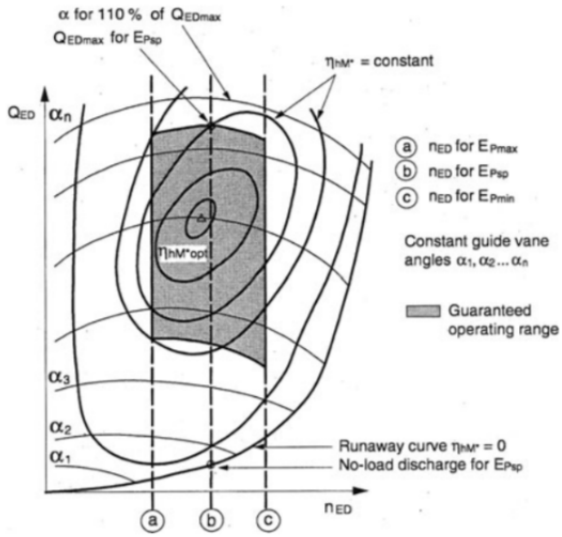

Figure 2.3: Illustration of a Hill-diagram for a model Francis turbine [3]

The discharge factor Q_{ed} and the speed factor N_{ed} are calculated according to Equation 2.1 and 2.2.

$$N_{ED} = \frac{n \cdot D}{\sqrt{E_h}} \tag{2.1}$$

$$Q_{ED} = \frac{Q}{D^2 \cdot \sqrt{E_h}} \tag{2.2}$$

where n denotes the runner rotational speed, D denotes the runner outlet diameter, Q denotes the discharge and E_h denotes the specific hydraulic energy. E_h is obtained by applying the Bernoulli principle along a streamline from the turbine inlet to the draft tube outlet, and can be calculated according to IEC60193:

$$E_h = g \cdot H = \frac{\Delta p}{\rho} + \frac{Q_1/A_1^2 - Q_2/A_2^2}{2} \tag{2.3}$$

where H denotes the turbine head, p denotes pressure, ρ denotes the water density and A denotes area. The hydraulic efficiency is calculated as the produced power divided by the available hydraulic power in the water:

$$\eta_h = \frac{\omega \cdot (\tau_f + \tau_g)}{E_h \cdot \rho \cdot Q} \tag{2.4}$$

where ω denotes the angular velocity, τ_f denotes the friction torque from the shaft bearing and τ_g denotes the generator torque.

2.2 Pressure pulsations

Pressure pulsations are flow phenomena that occurs inside the turbine during operation. The pulsations can either be of stochastic or deterministic nature, and appears from different sources and with varying intensities over the operating range. Pressure pulsations expose the turbine to vibrations and dynamic stresses, and thereby increase the risk of fatigue damages.

2.2.1 Rotor-Stator Interaction

Rotor-Stator Interaction (RSI) refers to the pulsations that arises from the interaction between the rotating runner blades and the stationary vanes. In a Francis runner, the pressure difference between the pressure side (PS) and suction side (SS) of the blade, results in a varying pressure field that moves with the runner [33]. In addition, a non-uniform flow field will leave the guide vanes, causing the runner to be subjected to a varying pressure field [29]. The combination of these two effects is illustrated in Figure 2.4.

Seen from the stationary frame of reference, a guide vane will be exposed to a pulse each time a runner blade passes. The frequency depends on the number of runner blades, Z_r, and the rotational frequency, $f_n = n/60$, where n denotes the rotational speed. j denotes the harmonic number and for $j = 1$, the frequency is referred to as the blade passing frequency.

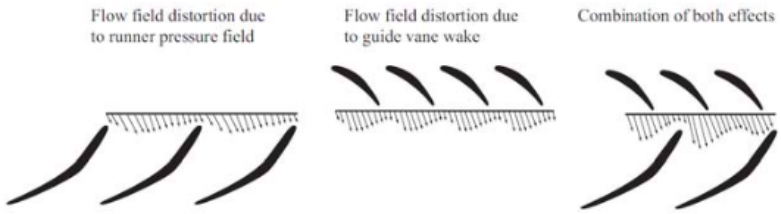

Figure 2.4: Velocity field at the runner inlet [4]

$$f_{bp,j} = Z_r \cdot f_n \cdot j \tag{2.5}$$

Likewise, seen from the rotational runner, a pressure pulse will be induced each time a runner blade passes a guide vane. This frequency depends on the number of guide vanes, Z_{gv}, and the rotational frequency f_n. m denotes the harmonic number and for $m = 1$, the frequency is referred to as the guide vane frequency.

$$f_{gv,m} = Z_{gv} \cdot f_n \cdot m \tag{2.6}$$

Depending on the combination of Z_r and Z_{gv}, the interference between the runner blades and the guide vanes occurs at a certain phase shift and time lag around the periphery of the runner [36]. This is illustrated in Figure 2.5, where two runner blades are excited in phase and induce a vibration mode with 2 nodal diameters (ND=2).

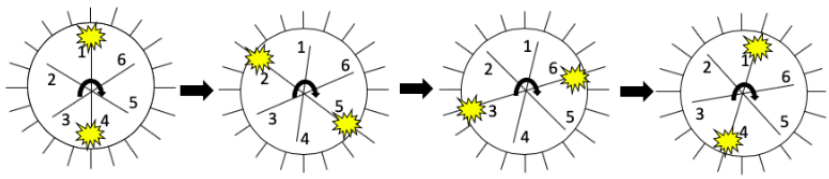

Figure 2.5: Snapshots of hydraulic interference between a rotating runner with $Z_r = 6$ and the stationary guide vanes with $Z_{gv} = 20$.

The shape of the overall pressure field created by RSI is determined by Equation 2.7, where k is the number of ND, and m and j are the number of harmonics of respective f_{gv} and f_{bp}.

$$k = m \cdot Z_{gv} \pm j \cdot Z_r \tag{2.7}$$

The RSI frequencies occur at all operating points, and the amplitudes tend to increase with smaller distance between the guide vanes and runner blades [37]. Consequently, the pulsations will be more pronounced at high load when the guide vane angle is at maximum.

2.2.2 Draft tube pressure pulsations

When a Francis turbine operates outside its design point, a swirling component will occur in the draft tube. This can be seen from the velocity triangles in Figure 2.6, which shows the relationship between the absolute velocity of the water c, the peripheral velocity of the runner u, and the relative velocity to the water w, with respect to the runner. The absolute velocity can be decomposed as c_m and c_u, the meridional and tangential component, respectively. In a Francis runner, the blades are fixed, thus the outlet angle β and u are constant, while w increases with increasing flow through the runner. As a consequence, when operating at part load (Q<$Q*$) and high load (Q>$Q*$), a tangential component in the water leaving the runner will occur. This give rise to the swirling component in the draft tube, which is associated with losses and unused energy [8].

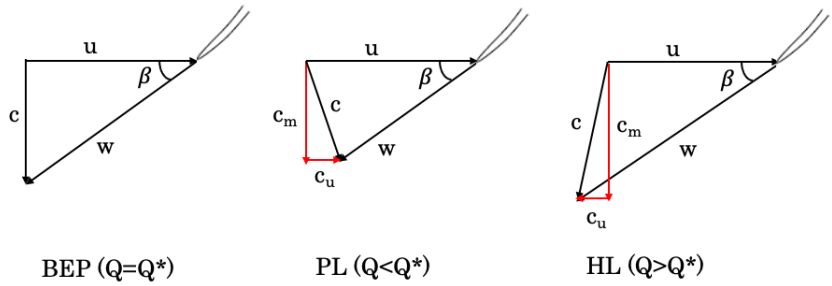

Figure 2.6: Velocity triangles at the runner outlet when operating at Best Efficiency Point (BEP), Part load (PL) and High Load (HL)

When a swirling flow enters the draft tube, it will separate into two flow patterns. The centrifugal forces will cause the primary fluid transport to move in the outer region, while a stagnation zone, or dead water core, develops in the central region [37]. If the swirl is severe enough, an abrupt change in the flow structure may occur in the central region, and a reverse flow can develop [5]. This is referred to as vortex breakdown, and is illustrated in Figure 2.7.

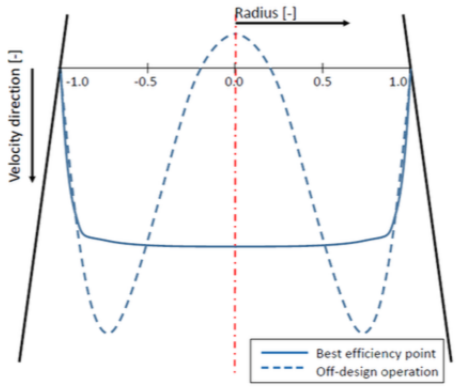

Figure 2.7: Axial velocity profiles in the draft tube at best efficiency point and off-design conditions [5]

At part load, the swirling component will move in the same direction as the rotating runner, and a helical shaped vortex filament can be observed at the interface between the two flow fields [37]. This is referred to as the rotating vortex rope, and will rotate around the axis of the draft tube and generate a low frequency pulsation. The frequency of the pulsation is called the Rheingans frequency and can be estimated by Equation 2.8 [37]. If cavitation is present in the low pressure region, the rope can becomes visible.

$$f_{re} \simeq 0.278 \cdot f_n \tag{2.8}$$

At overload, the swirling component will rotate in the opposite direction of the runner, and a pulsating cavitated vortex core may occur. Usually this condition is stable and the amplitude is normally not dominating, unless it coincides with natural frequencies in the system and large pressure pulsations may fluctuate [15].

2.2.3 Vortex shedding

Vortex shedding, also called Von Karman vortices, is a flow phenomenon that appears downstream a structure situated in a flow [4]. In a hydraulic turbine, Von Karman vortices will typically originate from the trailing edge of the stay vanes, guide vanes and runner blades. The vortices are initiated at the separation point, alternating between the pressure and suction side, which results in a swirling component fluctuating downstream with the wake, as illustrated in Figure 2.8. Consequently, the component is subjected to a vibration pulsating with the frequency of

the formation of the swirls [37]. The Vortex shedding frequency can be estimated with Equation 2.9,

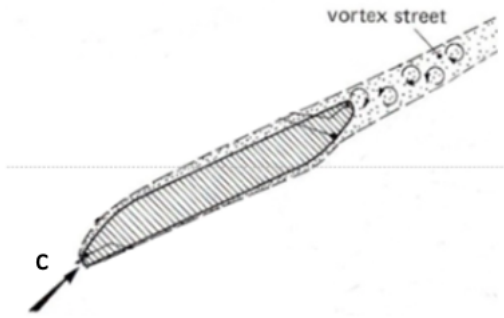

Figure 2.8: Flow condition around a vane [6]

$$f_{vs} = \frac{St \cdot c}{t} \tag{2.9}$$

where St denotes the Strouhaul number, c the velocity of the water, and t the thickness of the vane. The Strouhaul number depends on the shape of the vane and the Reynolds number. An empirical formula has been developed by Brekke for estimating the Vortex shedding frequency for a Francis runner [38]:

$$f_{vs} = 190 \cdot \frac{B}{100} \cdot \frac{c}{t + 0.56} \tag{2.10}$$

where B denotes the shape factor dependent on the trailing edge geometry. The Vortex Shedding is a high-frequency phenomena and may cause vibrations and noise [38]. It is therefore important that the frequency does not coincides with the natural frequency of the body producing it, to avoid resonance and cracking of vanes.

2.3 The effect of dynamic loads on materials

In this section, basic theory of material properties and failure of materials is presented. These topics are not directly applied in the further work, but are considered necessary for the reader to understand the concepts leading to crack growth.

2.3.1 Deformation and stress

When an external load is applied to a body, it will induce a mechanical stress, σ. Stress describes the distribution of internal forces within a body and, for a given stress, the body will response with some deformation, denoted the strain ε. Loads can be applied to a body as tension, compression or shear, and the magnitude may be constant over time or fluctuating periodically.

The relationship between stress and strain for a specific material can be obtained with a stress-strain curve [39]. Figure 2.9 shows a typical curve for steel alloy. In the initial region, for small strain values, the strain is proportional to the stress by a material constant called Young's modulus. In this region, the material behaves elastically and deformations are fully reversible. If the material is stressed beyond its yield strength, σ_y, the material will deform permanently. In this plastic region, the stress-strain relationship is no longer linear and only a small increase in stress will cause large deformation [39]. Stress will continue to increase until it reaches the ultimate tensile strength, σ_u, which is the maximum stress a material can withstand. If the material is held at this point, fracture will occur.

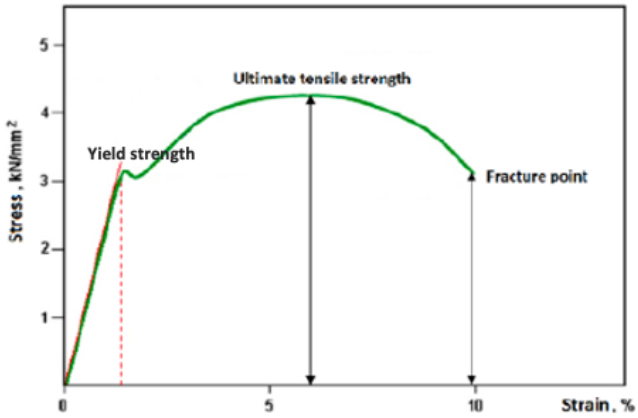

Figure 2.9: Illustration of a stress-strain curve for steel alloy [7]

2.3.2 Fatigue crack growth

Fracture can occur in components that are subjected to repeated cyclic loads even though the stress levels are considerably lower than σ_y and σ_u of the material. This failure mode is called fatigue, and is estimated to be the cause of $90^{\%}$ of all failures in metals [39, 40].

An important parameter characterizing a material response to fatigue is the fatigue life, which indicates the number of cycles necessary to cause fracture at a specific stress level [20, 40]. For a given uncracked material, this can be predicted with a stress-cycle (S-N) curve, obtained from experiments conducted on test samples for specific loading conditions. Figure 2.10 shows an example of a S-N curve, which presents the relation between the magnitude of a given stress amplitude and the number of cycles before failure. It is normal to differentiate between low-cycle fatigue (LCF) and high-cycle fatigue (HCF). LCF corresponds to a short fatigue life ($<10^4$ cycles) with corresponding high stress amplitude [41]. While for HCF, a larger number of cycles ($>10^5$ cycles) are required to produce fatigue. In addition to stress amplitude, fatigue life is dependent on the mean stress [8]. An increased mean stress will give a smaller number of cycles until failure, even with constant stress amplitude. Prediction of fatigue life using S-N approaches is not suitable for materials with existing defects, which is typical in welded structures. In this cases, Linear Elastic Fracture Mechanics methods should be applied, and these methods are well described in [39, 40].

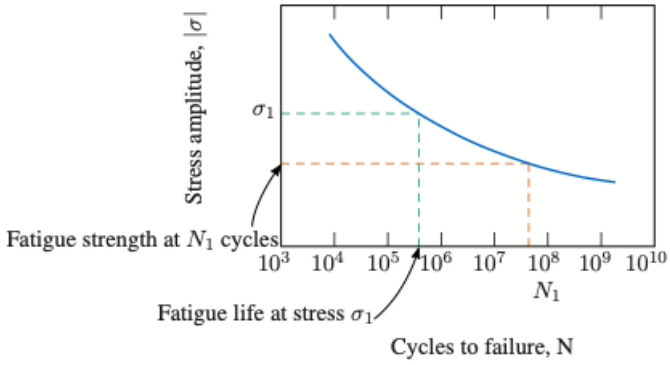

Figure 2.10: Example of a S-N curve for a non-ferrous alloy [8]

A fatigue crack damage can generally be divided into three main stages [20, 41]. First, the crack will initiate. In this stage micro-structural changes will cause permanent deformation to a small number of grains in the material, and microscopic cracks will start to grow. This will normally occur in regions where high stress concentrations and material defects coincide [40]. Further, if the material continues to be exposed to cyclic loading, the crack will grow to a macroscopic size, propagating incrementally with each cycle. Finally, when the crack growth has reached a critical size it results in a complete fracture. The crack growth rate is highly dependent of mechanical, micro-structural and environmental factors [9, 41].

Fatigue on Francis runners

Francis runners are subjected to both static and dynamic loads and the fatigue life is considered to be a combination of LCF from start and stop-cycles and HCF from pressure pulsations and transient operation [9, 40]. In addition, Francis turbines are normally a welded construction, where several hot formed blades are welded to the hub and shroud [40]. As a consequence, the runner could be prone to residual stresses from possible welding discontinuities and material defects, in addition to construction and assembly of the runner, which could also affect the fatigue life.

The majority of the studies reporting Francis turbine failures evidenced that the crack normally initiates at the trailing edge (TE) of a runner blade, in the welded joint close to the shroud, as a result of the combination of high stresses and possible welding discontinuities [9, 10, 17, 40]. From there, it normally follows a semi-elliptic curvature along the shroud, and when reaching a critical size, part of the blade may break off. Figure 2.11(a) and 2.11(b) show two crack growths occurring on the TE of Francis runner blades. Figure 2.11(c) illustrates a so-called shark-bite fatigue failure, where a crack caused part of the blade to break off during operating.

2.4 Signal processing and analysing techniques

Pressure pulsations and vibrations occurring on a turbine result from several independent flow phenomena at different frequencies, and the measurement signal will be a composition of these. As the runner degrades, characteristics of the signal in time and frequency domain may change. Features in time domain such as the mean and amplitude give an overview of the overall vibration and pressure levels, while in the frequency domain, the signal is decomposed into its different frequency components which allows for identification of the various components and their sources [37].

2.4.1 Data acquisition

An analog signal is a continuous signal that shows how a physical quantity varies with time. For a computer to store and process the data, it is necessary to digitize the analog signal, by means of taking "snapshots" [42]. Only the samples are stored, and all information between them are lost. The rate at which the samples are registered is called the sampling frequency, F_s. To give a correct reconstruction of the measured analog signal, F_s must be at least twice as big as the highest frequency occurring in the signal. This is referred to as the Nyquist theorem and is given in Equation 2.11.

$$F_s \geq 2 \cdot f_{max} \tag{2.11}$$

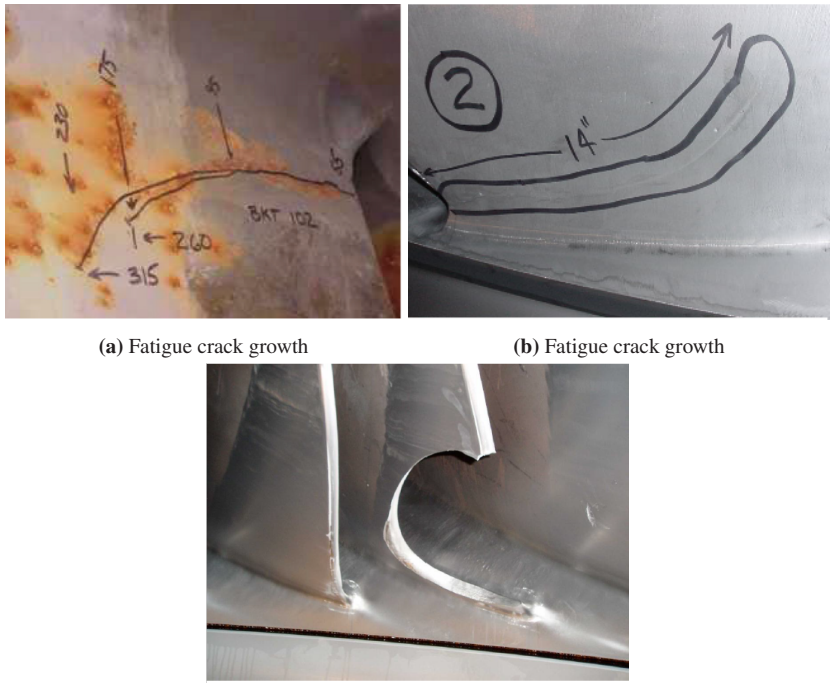

(a) Fatigue crack growth **(b)** Fatigue crack growth

(c) Shark-bite fatigue failure

Figure 2.11: Three cases of fatigue damage occurring on the TE of a Francis runner blade reported by Liu et al. (a)[9], Cotou et al. (b) [10] and Fjærvold (c) [11]

If the sampling frequency is too low, the frequency will fold back and appear as a low-frequency component in the digital spectrum [42]. This phenomenon is referred to as aliasing and is illustrated in Figure 2.12, where the samples are taken every 0.67 s, giving a sampling frequency of 1.5 Hz times the original frequency. As a consequence the reconstructed signal becomes different from the original.

When sampling complex signals consisting of several frequencies, it may be challenging to identify the highest frequency. The higher the sampling rate, the more data storage is required. However, to avoid the ambiguities resulting from aliasing, a sufficiently high sampling rate should be selected. Gogstad suggests a sampling frequency of ten times the highest expected frequency to be sufficient [5].

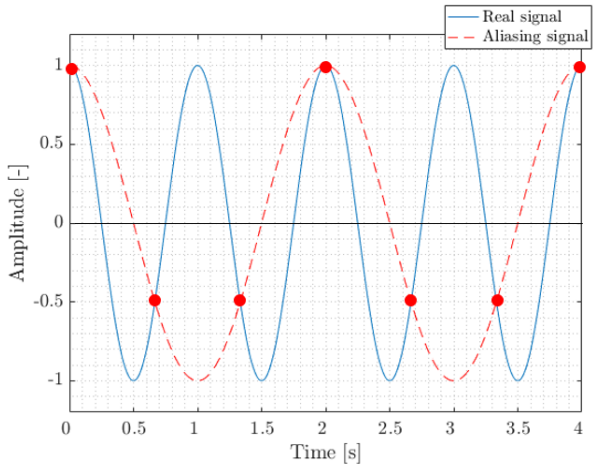

Figure 2.12: Illustration of aliasing, where the sampling frequency is 1.5 Hz times the original frequency.

2.4.2 Amplitude analysis

When describing the intensity of pulsations, the peak-to-peak value of the signal is normally used [37]. The peak-to-peak value shows the total variation in the signal, and give an impression of the amplitudes of the pressure pulsations and vibrations independent of frequencies [5]. According to IEC60193, the peak-to-peak value is defined as the variation which contains a certain percentage of the sampled signal, to filter out non-physical spikes [3]. Consequently, the value will depend on the chosen percentage level and IEC60193 recommends 97%. The histogram method is a statistical method to calculate the peak-to-peak value and is recommended by Döfler et al. [37]. Figure 2.13(a) shows a histogram plot of a pressure time series. The peak-peak value is the width of the interval where 1.5% of the lowest and highest value have been omitted. The respective time series with the upper and lower bound is shown in Figure 2.13(b)

2.4.3 Frequency analysis

Discrete Fourier Transform

The Fourier transform converts a signal in the time domain $f(t)$ into the frequency domain $F(\omega)$, where the signal is separated into its different frequency components [42]. Because the signal is discrete, the Discrete Fourier transform (DFT) is used, where the sequence length N, taken at sampling frequency F_s, is transferred to the

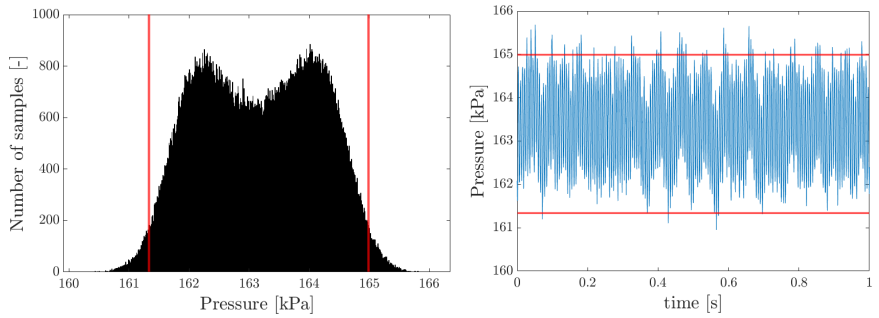

(a) Histogram plot **(b)** Time series

Figure 2.13: Illustration of histogram plot (a) and time series (b) with upper and lower bound based on a 97% confidence level. Pressure data is taken from a sensor in the vaneless space (PGV2) at BEP, from the conducted measurements

frequency domain. Direct computation with DFT is highly inefficient, therefore the Fast Fourier transform (FFT) is generally applied, which reduces the number of operations significantly.

Spectral leakage and Window functions

FFT is sensitive to noise and gaps in the sampled signal as it assumes the signal to be periodic and that it repeats itself infinitely in a cyclic manner [12]. These assumptions are rarely valid for experimental measurements, and the discontinuity will result in power spreading in the spectrum. Different weighting functions, called windows, can be applied to compensate for this. In case of a Hann window, it starts near zero, rises to a maximum at the center and decreases towards zero again, as illustrated in Figure 2.14(a). Consequently, by multiplying the signal with the window in time domain, the discontinuity is removed [12]. However, multiplication in time domain implies time shift in the frequency domain, thus give rise to several sidelobes, as seen in Figure 2.14(b). These sidelobes are undesirable and distort the signal by smearing out the peaks in the spectrum, causing spectral leakage [42].

Different windows with different frequency characteristics can be applied depending on the nature of the data set. To obtain sufficient frequency resolution, the width of the main lobe should be minimized. This can be done by increasing the length of the window, i.e., the number of samples N, as seen from Equation 2.12. Some well known window functions are Hann, Hamming, Flat top, and Blackman Harris. According to IEC60193, the Hann window is recommended for analysing pressure pulsations [3].

$$F_{res} = \frac{f_s}{N} \tag{2.12}$$

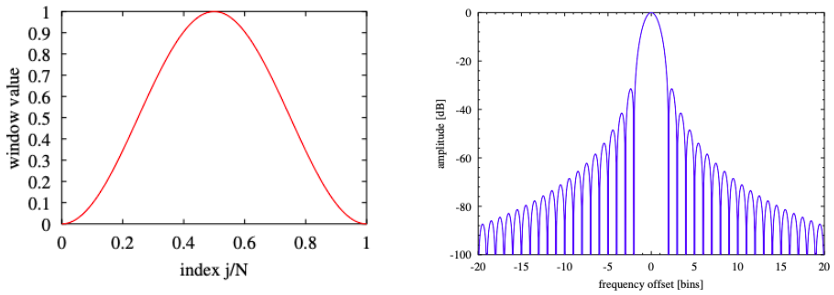

(a) Time domain **(b)** Frequency domain

Figure 2.14: The Hann window in time domain (a) and frequency domain (b) [12]

The Power Welch Method

By computing the FFT of the windowed data segment directly, the estimated power spectrum will be slightly noisy due to high variance in the amplitudes [12, 42]. The Welch method can be used to improve accuracy. The method returns the estimated power spectrum, called a periodogram, by dividing the sampled data into overlapping segments. Each block is multiplied with a window before FFT is applied. Further, the resulting periodograms are averaged over all windows, which reduces the variance of the amplitudes [42]. The method is illustrated in Figure 2.15. In other words, an increased window length will improve the frequency resolution, but give greater amplitude variance. Good accuracy and low variance will therefore require long data samples.

Harmonics

When interpreting the results from frequency analysis, it is important to be aware of harmonics in the signal. When a signal is periodic but not perfectly based on sine waves, harmonics may occur in the transformation [5]. These harmonics are physical fluctuations in the system, with a frequency that is an integer multiple of the original frequency [4].

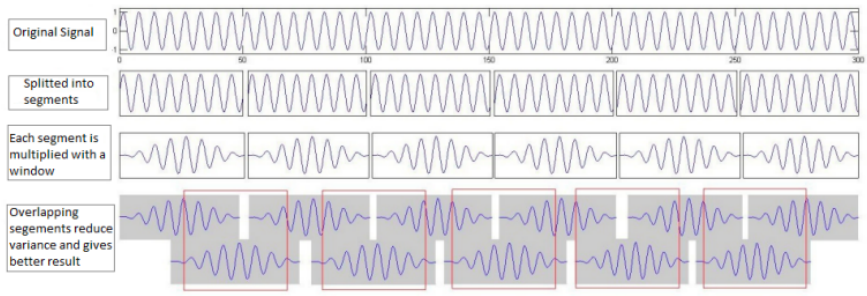

Figure 2.15: Illustration of the Power Welch method using overlapping segments, [13]

2.5 Uncertainty analysis

All measurements of a physical value will involve some level of uncertainty. It is therefore essential to examine the different sources of errors, when evaluating the quality of the obtained measurement. The true size of the error is not known, but it can be estimated with statistical tools. In this way, the range within which the actual value of the physical property is expected to lie, can be found, with a certain probability. According to IEC60193 this probability should be set to 95% confidence interval [3]. The error in the measurement of a quantity is defined as the difference between the measurement and the true value of the quantity [43]. The types of errors are normally divided into spurious errors, systematic errors and random errors.

Spurious errors

Spurious errors typically arise from human mistakes or failure in the measuring equipment [44]. In some experiments one or more measured values appear to be out of line with the rest of the data. Such wild and outlier data points should be disregarded.

Random errors

Random errors are caused by small, independent influences which prevents the instrument from giving the same output readings when measuring the same physical quantity over time [45]. In addition, small independent variations in external properties such as temperature and atmospheric pressure can also affect the repeatability of the measurement system [44].

Random errors are of stochastic nature and the distribution approaches a normal

distribution when the sample size increases towards infinity [44]. However, in cases of smaller samples size and when investigating the error in the measurement of a single, constant physical property, the distribution of the measurement around the mean can be estimated by the Student t-distribution [45], which has a higher variance than the normal distribution. The confidence interval of the mean value of a measurement, $\bar{X}$, with a certain confidence level is calculated with Equation 2.13 and Equation 2.14.

$$\bar{X} \pm \frac{t_{\alpha/2} \cdot S_x}{\sqrt{N}} \tag{2.13}$$

here N denotes the number of samples and $t_{\alpha/2}$ is Student t-coefficient based on the chosen confidence interval 1-α and N, and S_x is the standard deviation. The standard deviation of a number of observations is defined as

$$S_x = \sqrt{\frac{\sum_{N=1}^{\infty}(x_i - \bar{x})^2}{n-1}} \tag{2.14}$$

where x_i denotes the measured value and $\bar{x}$ denotes the mean. Both Equation 2.13 and Equation 2.14 get smaller when N increases, thus an increased number of measurements will reduce the random error.

Systematic errors

Systematic errors may be due to poorly calibrated instruments, hysteresis, or lack of linearity in the instrument [44]. Such errors are consistent and repeatable, thus cannot be reduced by increasing the number of measurements. To identify the magnitude of the systematic errors, the complete measuring process needs to be analysed, including the calibration method and the random errors during calibration.

Systematic and random uncertainty needs to be evaluated with the same level of confidence to be combined [45]. Finally, the total uncertainty (e_t) is found by combining the systematic uncertainty (e_s) and the random uncertainty (e_r) with the Root Sum Square (RSS).

$$e_t = \pm\sqrt{e_s^2 + e_r^2} \tag{2.15}$$

Chapter III

Experimental Setup and Method

■ This chapter gives a description of the facilities, instrumentation and measurement procedures used for the study. The second part shows methods used for post-processing the data. Part three present the calibration methods and uncertainty evaluation related to the instruments. Finally, a description of the damage case is presented.

3.1 Francis model test rig

The measurements were conducted on the Francis model test rig located at the Waterpower Laboratory at NTNU. The test rig holds international standard for model testing according to IEC60193 [3]. It consists of an upper reservoir, a pipe system, a high and a low pressure tank, a turbine and a generator. In the basement there is a lower reservoir with two centrifugal pumps, that can be operated in both series and parallel.

The Francis test rig can be operated in either an open, closed or a semi-closed loop, which allows the rig to run in a wide range of operating conditions. In the open loop configuration illustrated in Figure 3.1(a), the water is pumped to the upper floor of the laboratory and flows through the u-formed open channel allowing for a maximum head of 16 meter. Higher heads can be achieved by operating the rig in a closed-loop, where the water is pumped directly to the high pressure tank, that acts as an imaginary reservoir of the system. The water from the turbine is directly led back to the pumps in the basements through pipes without forming any free surfaces.

For the measurements in this study, a semi-closed loop configuration was used, as illustrated in Figure 3.1(b). The upstream pressure was regulated with the centrifugal pumps in the basement, whereas the downstream pressure was closed to atmospheric pressure. It was possible to lower the pressure below atmospheric pressure in the draft tube tank to further increase the head, but for this test the water level was open to atmospheric pressure. After the draft tube tank, the water flowed back to the basement reservoir instead of going directly to the pumps, as in the case of a closed-loop. The procedure for operating the semi-closed loop is attached in Appendix D.

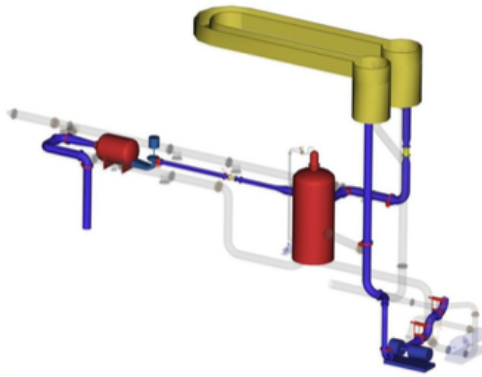

(a) Open loop

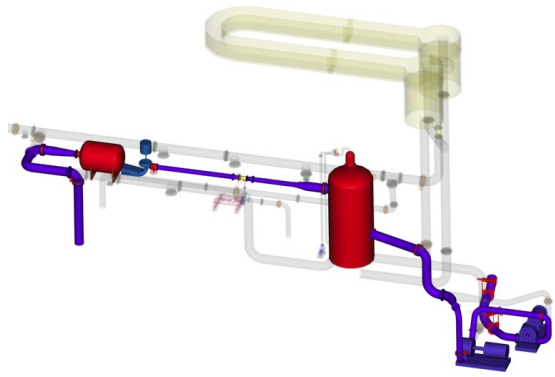

(b) Semi-closed loop

Figure 3.1: Illustration of open loop configuration (a) and semi-closed loop (b) in the Francis model test rig.

The Francis-99 model runner was used for the measurements and is shown in Figure 3.2. The runner is a reduced scale (1:5.1) model, based on the main parameters from Tokke power plant in Norway [1]. The runner consist of 30 runner blades, where 15 are of full length and 15 are of half-length. The runner inlet and outlet diameters are 0.63 m and 0.347 m, respectively. The number of guide vanes is 28, and the spiral casing consists of 14 stay vanes.

The turbine is installed with a vertical shaft and a DC generator of 352 kW is located above. The generator can also operate as a motor in pumping mode. A DC converter is connected to the generator and the power grid, allowing to adjustment the speed and torque of the generator. An Interactive Graphical SCADA system (IGSS) in the control room is used to regulate the valves and the pumps in the basements, and the guide vane angles are changed with a switch.

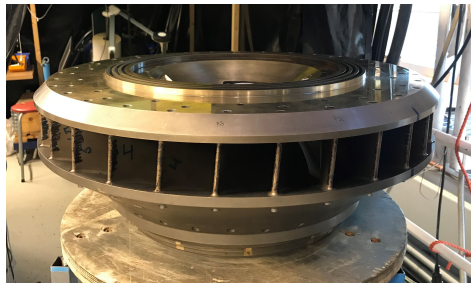

Figure 3.2: The Francis-99 model runner

3.2 Instrumentation

3.2.1 Sensors

To acquire data for the study, nine pressure sensors and three accelerometers were installed on the rig prior to the measurement. These sensors and their location were selected to detect the hydraulic phenomena occurring in a turbine during operation, and with a view to convenient and subsequent installation on prototypes. In addition, signals related to the operating conditions of the machine were acquired from sensors permanently installed on the rig. All sensors used for the measurements are listed in Table 3.1.

Pressure sensors

Pressure sensors were mounted in the stationary domain of the turbine to measure pressure pulsations. Both static sensors and dynamic sensors were utilized, where both consist of a sensing element, a diaphragm, that respond to a force applied

by the water pressure. The static sensors rely on the piezo-resistive effect, where the electrical resistance changes when the diaphragm deforms. For the dynamic sensors, a given force results in a corresponding electrical charge across the diaphragm, according to the piezo-electric effect. The dynamic sensors only measure changes in pressure over time.

One static sensor was installed at the inlet before the spiral casing (PIN) and one at the top-cover of the turbine (PTC). Three sensors (PGV1-3) were mounted in the vaneless space, between the stationary guide vanes and the runner blades. Two pairs of sensors were mounted on the transparent draft tube cone in two horizontal planes, 180° from each other. On the upper plane, close to the runner outlet, two static sensors were installed (PDT1-2), while on the lower plane, two dynamic sensors were used (PDT3-4). Figure 3.3 and Figure 3.4 show schematic illustrations of the pressure sensors and their locations.

All sensors, except from PDT1 and PDT2, were flush-mounted to obtain direct contact with the water in the channel, in accordance with IEC60193 [3]. PDT1 and PDT2 were recessed so a small water column was present between the sensors and inner wall of the draft tube cone.

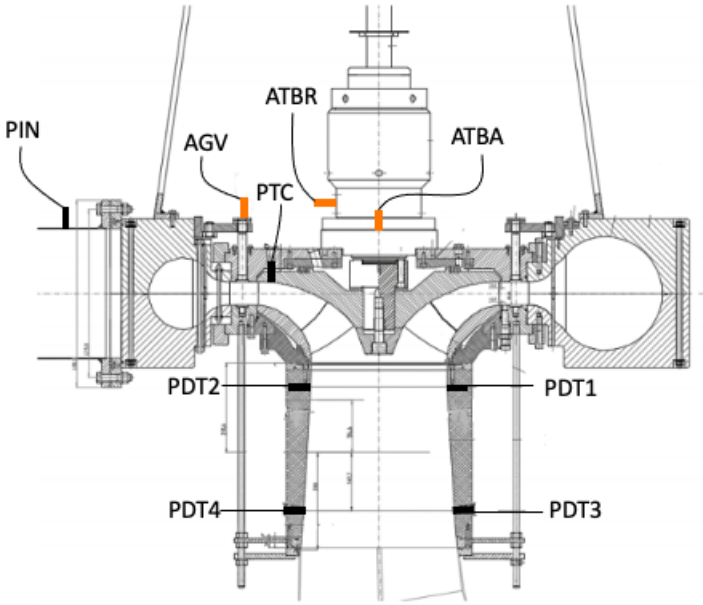

Figure 3.3: Location of the pressure sensors and accelerometers used for the experiment.

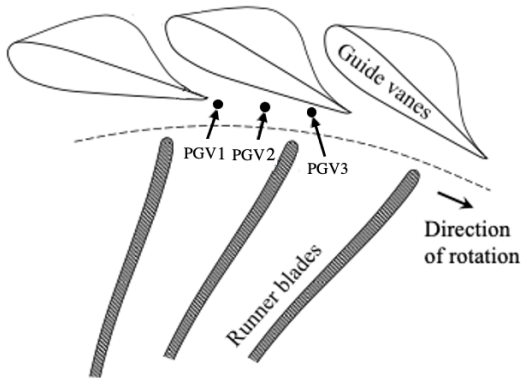

Figure 3.4: Location of the pressure sensors in the vaneless space

Accelerometers

The accelerometers were of Bruel & Kjær, type 4397, and utilizes the piezo-electric effect to measure the vibration (dynamic acceleration) of the structure. Two accelerometers were mounted on the turbine bearing, one in radial direction (ATBR) and one in axial direction (ATBA). In addition, one accelerometer was mounted on the guide vane shaft (AGV) in the axial direction.

Operating point sensors

The sensors measuring the operating conditions are permanently installed on the Francis rig and their location can be seen in Figure 3.5. An electromagnetic flow meter (QIN) and a temperature probe (TIN) are mounted at the turbine inlet pipe to measure the discharge and the water temperature, respectively. The differential pressure between the inlet and outlet of the turbines is measured by two pressure sensors (PPIN, PDP). The generator torque and friction torque are measured by two respective load cells (WGT, WFT).

On top of the shaft, a magnetic rotary encoder (ZRS) is located to measure the rotational speed, giving one pulse per revolution. Similar type of encoder is used to measure the guide vane angle (ZGV) on top of the ring. In addition, there exist a position sensor (ZRP) on top of the shaft to relate the rotational speed to the angular position of the runner. The sensor is a digital encoder and a digital-to-analog converter (DAC) that converts the digital position signal to an analog ± 10V saw tooth signal, where one saw tooth represents one revolution of the runner.

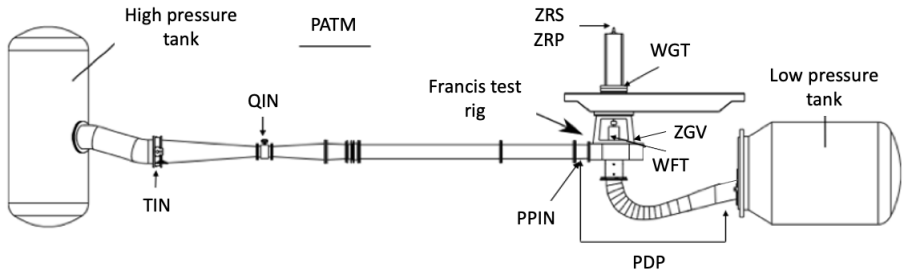

Figure 3.5: Operational sensors permanently installed on the Francis rig

Sensor	Description	Type/Full scale range	Output signal
PIN	Inlet spiral casing	Kulite HKM 375/7barg	mV
PTC	Upper turbine cover	Kulite HKM 375/7barg	mV
PGV1	Vaneless space	Kulite XTE 190/3.5bara	mV
PGV2	Vaneless space	Kulite XTE 190/3.5bara	mV
PGV3	Vaneless space	Kulite XTE 190/3.5bara	mV
PDT1	Draft tube cone, upper plane	Kulite HEM 375/1.7bara	mV
PDT2	Draft tube cone, upper plane	Kulite HEM 375/1.7bara	mV
PDT3	Draft tube cone, lower plane	Kistler 701A/250bara	pC
PDT4	Draft tube cone, lower plane	Kistler 701A/250bara	pC
ATBR	Turbine bearing (radial direction)	B&K 4397	pC
ATBA	Turbine bearing (axial direction)	B&K 4397	pC
AGV	Guide vane shaft	B&K 4397	pC
TIN	Inlet temperature	Pt100	Ω
QIN	Inlet pipe flow	Khrone 250 mm	V
PPIN	Inlet pipe pressure	Fuji-Electronics FKCW36	mA
PDP	Differential pressure inlet outlet	Fuji-Electronics FKCW36	mA
WGT	Generator torque	Load cell	mV
WFT	Friction torque	Load cell	mV
ZRS	Runner speed	P+F FSS58N	V
ZRP	Runner angular position	Digital encoder	V
ZGV	Guide vane position	Multiturn absolute encoder	V
PATM	Barometer	Vaisala PTB220	

Table 3.1: Summary of the sensors used in the measurement

3.2.2 Signal recording system

The data recording was made using National Instrument (NI) hardware. The equipment specifications are presented in Table 3.2. The pressure sensors and accelerometers were connected to a common 8-slot chassis of type NI-cDAQ-9178.

The static pressure sensors mounted at the inlet, in the vaneless space and upper draft tube cone were piezo-resistive transducers, and were connected to an analog input bridge module, NI-9237. The dynamic pressure sensors on the lower draft tube cone were piezo-electric and returned an output signal in terms of electrostatic charge. Therefore, it was necessary to amplify and convert the signal, using a charge amplifier, to the desired voltage to bar relation. The Kistler charge amplifiers are shown in Figure 3.6, and where in turn connected to a NI-9239 analog input module on the cDAQ device. The accelerometers were conditioned and digitized using a NI-9234 module for sound and vibration.

Hard ware	Type
Data acquisition chassis	NI-cDAQ-9178
Bridge analog input module	NI-9237
Analog input module	NI-9239
Dynamic signal acquisition module	NI-9234
Charge amplifier	Kistler 5015

Table 3.2: Signal recording equipment

Figure 3.6: Kistler charge amplifiers

The data was recorded using an adapted LabVIEW program. To ensure sufficient data resolution and reconstruction of all frequencies, the sampling rate for the

current measurements was set to 5120 Hz. This resulted in a TDMS-file with all the raw data that was further imported to Matlab for post-processing.

3.3 Measurement procedure

Five operating points were selected to study the behaviour of the machine. The points were similar to the operating points conducted in the HiFrancis project [1], in addition to two points on the upper and lower range. The operating points, with corresponding guide vane angles, are given in Table 3.3. All measurement points were taken at constant rotational speed corresponding to $n_{ED} = 0.18$ for a given head. The machine was operating at these points long enough to ensure stable conditions, before the measurement point was recorded for 60 seconds. The procedure was repeated for heads of 12 m, 18 m, 24 m and 30 m.

Nomenclature	Description	α
DPL	Deep part load	4°
PL	Part load	6.7°
BEP	Best efficiency point	10°
HL	High load	12.4°
FL	Full load	14°

Table 3.3: Operating points

3.4 Post processing methods

The experimental work conducted in this project resulted in extensive data to process. The raw data from each measurement were transferred to Matlab and organized in a large structure array for post-processing.

The pressure signals have been normalized based on Equation 3.1 and 3.2, as recommended by IEC60193 [3]. $\tilde{p}$ denotes the measured pressure a given time, $\overline{p}$ denotes the average pressure at the corresponding location, ρ denotes the density of the water and $E = gH$ is the specific energy at BEP. Thereby, it is possible to compare pressure fluctuations from different sensors, heads and operating points.

$$\tilde{p}_E = \frac{\tilde{p} - \overline{p}}{(\rho \cdot E)_{BEP}} \tag{3.1}$$

$$\tilde{p}_{Erms} = \frac{\tilde{p}_E}{\sqrt{2}} \tag{3.2}$$

Resampling of the signal

Due to difficulties in setting the rotational speed on the DC-generator, small speed variations occurred during the measurements, as shown in Figure 3.7(d). These variations will smear out the rotational speed-dependent frequencies in the frequency domain, causing reduced frequency resolution and increased amplitude variance. To remove these effects, the pressure signals were resampled at a fixed rate in the position signal from the position sensor (ZRP) in accordance to Agnalt [46].

The raw signal from the position sensor is illustrated in Figure 3.7(a), where one saw tooth represents one rotation of the runner. The voltage signal was further smoothed out and converted to degrees, as seen in 3.7(b). Further on, a continuous position vector was created from the saw tooth signal by adding $360°$ to each drop, illustrated in 3.7(c). The built-in resample function in Matlab was used and the measurands were interpolated to a fixed number of equally spaced sample points per revolution from the continuous position vector in 3.7(c). The rotational speed was then calculated by the first derivative of the position vector. Figure 3.8 shows the time domain signal and the resampled position domain signal.

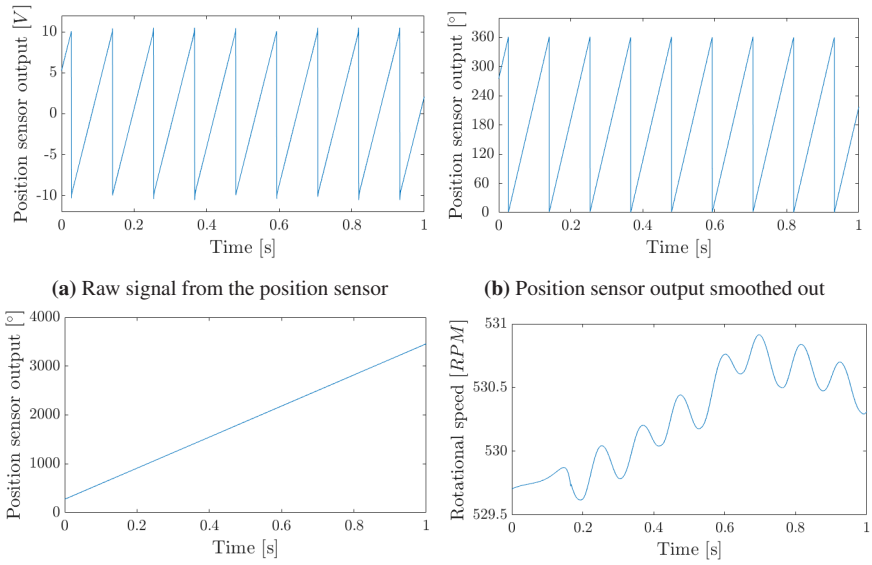

(a) Raw signal from the position sensor

(b) Position sensor output smoothed out

(c) Continuous position vector

(d) RPM variation in one second

Figure 3.7: Processing of the position sensor signal in the resampling process.

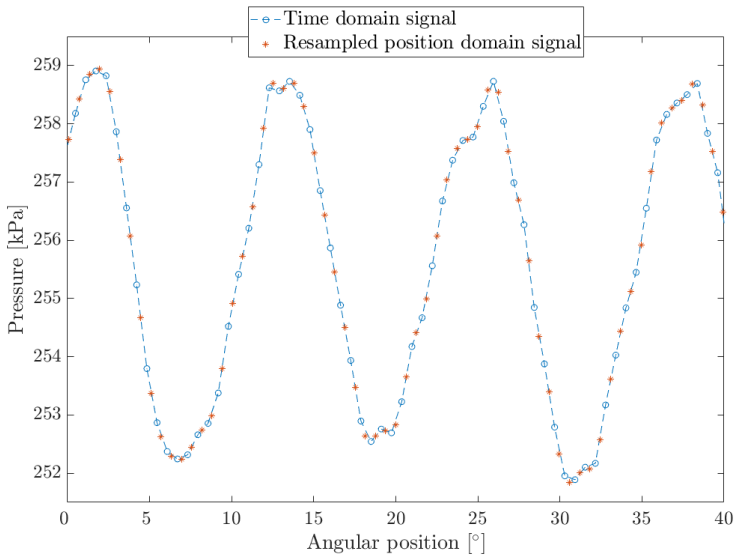

Figure 3.8: Time domain signal and resampled position domain signal

To validate the resampling process, frequency analyses of the time domain signal and the resampled position domain signal were compared for the first harmonic of the blade passing frequency, $f_{bp} = 30f_n$. As described in subsection 2.4.3, a longer window length will improve the frequency resolution, but give higher amplitude variance. Thus, to demonstrate the effect from resampling the signal, the FFT-comparison is shown for two cases; one with high amplitude accuracy, and one with high frequency resolution. In Figure 3.9(a), the frequency analysis are done with 50 flat-top windows with 50% overlap, as this window function is known to give good amplitude predictions [12], which is identified from the figure for both signals. In Figure 3.9(b), a single hanning window is used, to demonstrate the case with a high frequency resolution. The resolution is improved for the resampled signal and the amplitude remains unchanged. However, due to the speed variations in the time domain data, the blade passing frequency is smeared out and the amplitude accuracy is thereby reduced. This indicates that after resampling the signal, both the frequency resolution and the accuracy of the amplitudes are greatly improved. On the contrary, the resampling process will cause the speed-independent frequencies to be smeared out in the spectrum. However, as the speed-dependent frequencies were of greatest interest in this study, the resampled pressure signals were further evaluated.

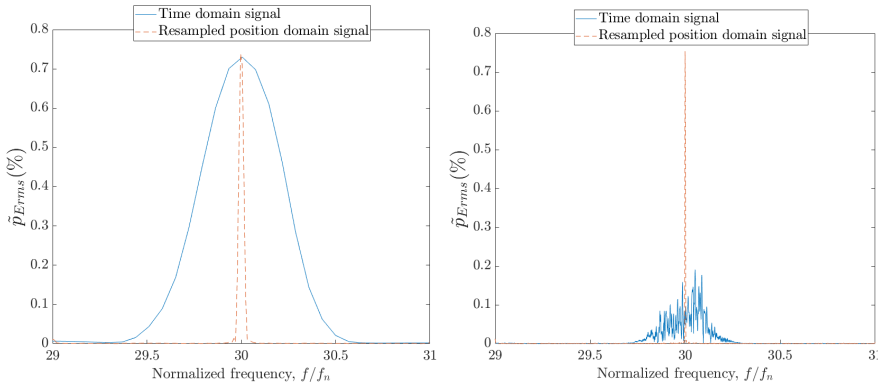

Figure 3.9: FFT comparison of time domain data and resampled position domain data for the blade passing frequency measured by PGV3. In (a), 40 windows are used to show the case of high amplitude accuracy, while in (b), a single window is used to show the case of high frequency resolution. Both cases demonstrates the unaffected amplitude accuracy for the resampled signal.

Pressure variation relative to damaged blade

An angular reference system is used to show the angular distance between the damaged blade and the stationary sensors during rotation. This representation is used to efficiently point out where in the pressure signals the damaged blade passes each specific sensor. First, the reference position of the trailing edge of the damaged blade was found, by using the signal from the speed sensor. Then the angles of the sensors were calculated and related to this reference position. The sensors upstream of the runner were adjusted for the wrap angle, $\alpha_{wrap} = 70.18°$, which is the angular difference from the trailing edge to the leading edge of the blade. Details of the process and the calculated sensor angles are given in appendix B.1. Finally, all runner revolutions, which corresponds to 530 when operating at H=30m, were combined, and the mean pressure was calculated for a constant angle step. The standard deviations was also calculated which indicates an upper and lower band of the pressure variation. Thereby, information about the signal of both stochastic and systematic quantities can be investigated [1].

Frequency analysis

To analyse the frequency content in the pressure and vibration signals, the Power Welch Method was used with a Hann-window and 50% overlap, as recommended

by IEC60193 [3]. The number of windows and thus the window length, were set to obtain a high frequency resolution with as low amplitude variance as possible. This resulted in 8 windows, giving a frequency resolution of $f_{res} = 0.133$ Hz, found from Equation 2.12.

3.5 Calibration and uncertainty

The static pressure sensors were calibrated prior to the measurement in their expected pressure range with a dead weight manometer. This method is considered to be the primary calibration method for pressure measurements according to IEC60193 [3]. Two dead weight manometers of different range were utilized, allowing for calibration of both low and high pressure ranges. To ensure accuracy, the sensors were calibrated with the whole measurement chain planned for the experiment. The setup for the static calibration with the dead weight tester in the low pressure range is shown in Figure 3.10.

Figure 3.10: Experimental setup for the static calibration (low pressure range)

By applying a known weight to the piston with a defined area, the respective pressure is obtained with Newtons second law. In this way, with a known input weight and the corresponding output voltage, the calibration curve can be determined using linear regression. To obtain repeatability and minimize errors due to hysteresis, weights in the expected pressure range were applied during both on- and off-load, in two series. The calibration reports of the static pressure sensors are given in appendix C.2.

The focus of this work has been to investigate trends, rather than absolute values. As a consequence, the operational sensors were not calibrated prior to the

measurements. In order to operate the rig and repeat the operating points for all measurement series, the calibration constants found by Langleite in spring 2020, were assumed to be valid. The calibration constants and corresponding systematic uncertainty evaluation for the operational sensors can be found in [47].

The variables of interest in this study, such as pressure and vibration amplitudes, are of dynamic properties. Thus, static calibration may not be valid to evaluate these [46]. For the sensors that are flush-mounted, the uncertainty related to hole size, cavities and transmission tubes will be negligible. The time and frequency response are therefore only related to the dynamic properties of the sensor diaphragm and the data acquisition system. Furthermore, it is stated by the producers that all pressure sensors and the measurement chain have natural frequencies above 30 kHz. Because the frequencies of interest and the largest system frequencies are below 1.2% of resonance, it is assumed that the uncertainty due to the dynamic behaviour can be neglected, and only the uncertainty from repeatability and hysteresis from static calibration remains [48]. The combined uncertainty from repeatability and hysteresis was found from the producer sheets and is stated to be 0.5% of full scale output (FSO) for the static pressure sensors. The relative uncertainties of the amplitudes measured by the accelerometer and the dynamic pressure sensors are stated by the producer to be 1.2% and 0.5%, respectively. Documentation of the pressure sensors and the accelerometers are attached in appendix C.1.

3.6 Damage description

The crack was developed to simulate a realistic crack growth, that typically occur on Francis runners. It was initiated on the trailing edge of one blade, in the t-joint between the blade and the shroud. It followed a semi-elliptical path along the shroud, resulting in a fully realised detached shark-bite shaped fragment. The crack was extended in 8 stages from the normal situation, by the respective lengths that are given in Table 3.4. An additional stage was included with an enlarged opening. A detailed view of the crack propagation stages are shown in Figure 3.11. In the following sections, the terminology that will be applied to describe the different crack propagation stages is as listed:

- Stage 0: Normal condition
- Stage 1-7: Crack growth
- Stage 8: Detached fragment
- Stage 9: Enlarged opening of the detached fragment
- Stage 1-9: Damaged blade

Stage	1	2	3	4	5	6	7	8
Crack length [mm]	15	30	50	72	95	115	140	170

Table 3.4: Total crack lengths

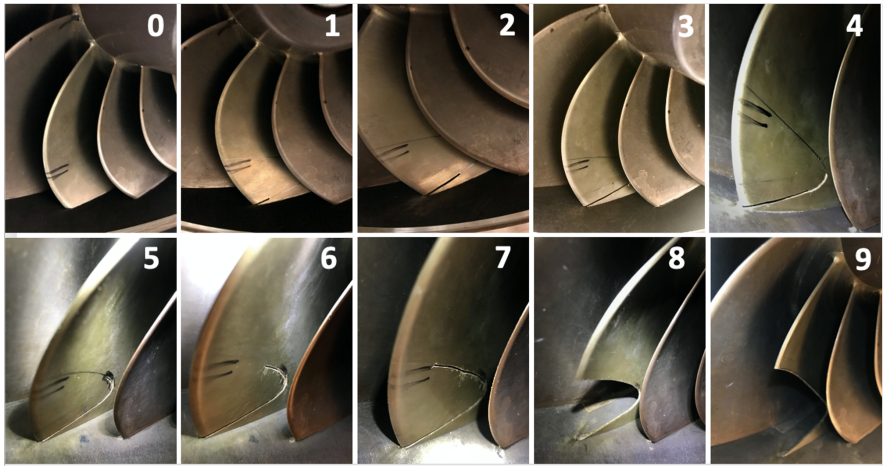

Figure 3.11: Crack propagation stages: 0 indicates normal condition, 1-7 show the crack growth, 8 indicates a fully realised detached fragment and 9 shows an enlarged opening of the detached fragment.

Stage 4-7 represent an unnatural crack development for a case of fatigue in a material. However, the stages were included to investigate whether a potential fracture would extend and detach a fragment during the measurements. Figure 3.12 shows 3D-drawings of the two cases at stage 8 and 9. In stage 8, the opening width corresponds to $1/3$ of the TE arc length, while in stage 9 the width is equal to $1/2$ of the TE arc length.

The blade and splitters of the Francis-99 runner are fastened to the hub and shroud using bolts, instead of welded. Therefore, a new manufactured blade was ordered to avoid destroying the reference runner. The new blade turned out to be 260 gram lighter than the reference blade, due to the use of another brass alloy. Figure 3.13(a) shows lab-technician Opland assembling the new blade.

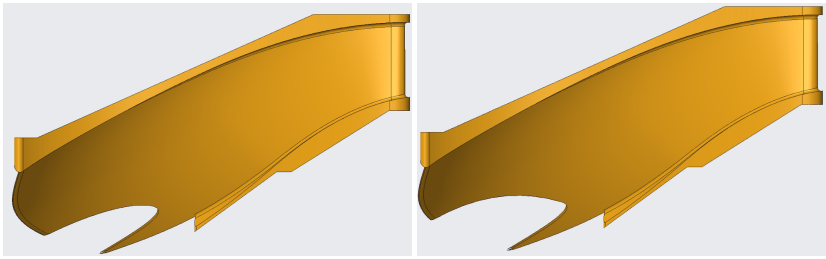

(a) Stage 8 **(b)** Stage 9

Figure 3.12: 3D drawings of stage 8 in (a) and stage 9 in (b)

A dremel, which is a small and corded rotary tool, with a 1 mm ball nose cutter, was used to manually cut the stages. This allowed for high precision without disassembling the runner between each measurement. 3D-printed templates were made for each stage to ensure correct form and length. Between each measurement, the transparent draft tube cone was disassembled and the runner blade was cut for the following stage, as shown in Figure 3.13(b).

(a) Opland assembling the new blade **(b)** Haukvik cutting the second stage

Chapter IV

Results

■ In this chapter, the experimental results for all crack propagation stages are presented. The first and second section show the pressure and vibration signature analysis in time domain. The third section presents the frequency analysis for both pressure and vibration sensors. Section four shows the evolution of the turbine performance with crack growth. Finally, a comparison with the reference Francis-99 runner blade is presented in section five.

4.1 Pressure signature in time domain

This section presents the results from the pressure measurements in time domain for different crack propagation stages. The measurements are shown for selected sensors, with focus on those that exhibit a trend. Pressure data from the remaining sensors can be found in appendix A.1. Unless otherwise stated, the presented data is shown for BEP at $H = 30$ m.

4.1.1 Pressure fluctuations for different crack propagation stages

The raw pressure data measured by the sensors PTC, PGV2 and PDT1 is presented in Figure 4.1 - 4.3. 10 runner revolutions from stage 0, 7, 8 and 9 are shown. No significant changes are observed in the signals during stage 1-6, thus these stages are omitted.

At stage 8 and 9, a local change in static pressure can be recognized in every revolution for all sensors. This is most prominent in the vaneless space (PGV2), where it corresponds to a distinct reduction in static pressure.

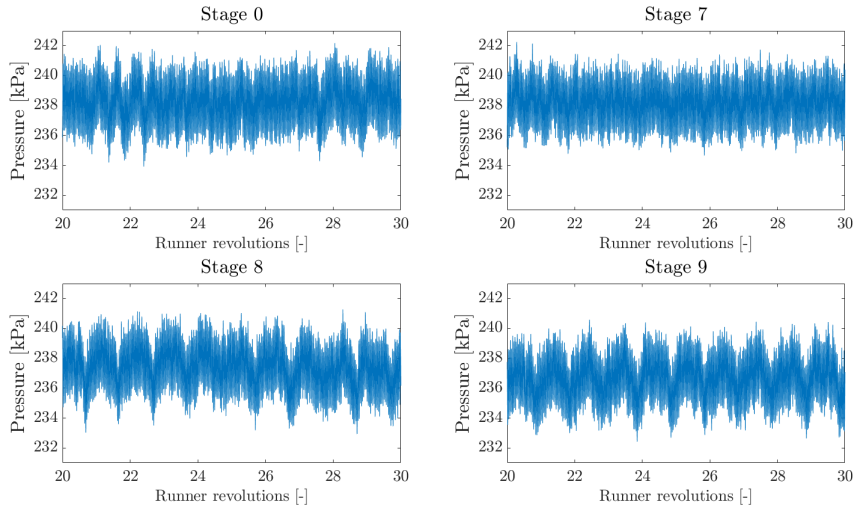

Figure 4.1: Raw pressure data measured by PTC at BEP and H=30 m. 10 runner revolutions from stage 0, 7, 8 and 9 are shown

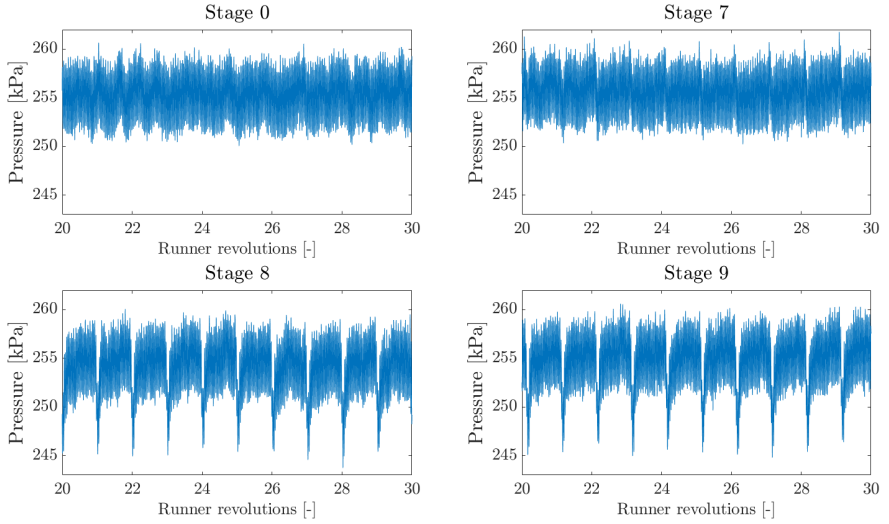

Figure 4.2: Raw pressure data measured by PGV2 at BEP and H=30 m. 10 runner revolutions from stage 0, 7, 8 and 9 are shown

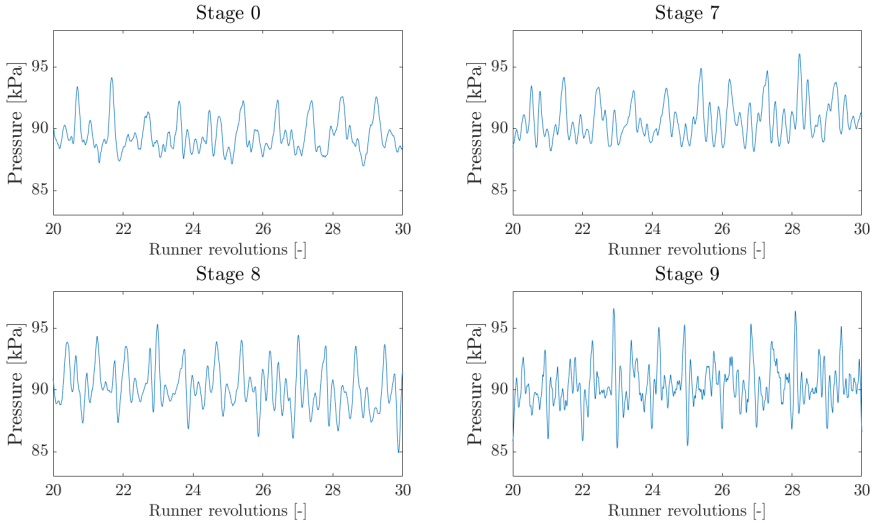

Figure 4.3: Raw pressure data measured by PDT1 at BEP and H=30 m. 10 runner revolutions from stage 0, 7, 8 and 9 are shown

To further evaluate the pressure change relative to the damaged blade, the data was resampled and the positions of the pressure sensors were found, as described in section 3.4. The following figures present the average runner revolution, with added and subtracted standard deviations, for 530 full revolutions. The pressure signals were normalized based on Equation 3.1.

Vaneless space, PGV1-PGV3

The results from PGV1, PGV3 and PGV3 are presented for crack propagation stage 0, 3, 5, 7, 8 and 9 in Figure 4.4 - 4.6. The red dotted line indicates where the LE of the damaged blade passes the respective sensors. As the pressure distribution in the vaneless space is related to the blade channel pressure, each channel is shown on the x-axis. Due to the splitter blade design, the two channels next to the damaged blade corresponds to channel (-1, -2) and (1, 2), where those denoted with "-" are the preceding channels, and "+" are the succeeding channels.

Several trends become prominent when examining an average runner revolutions. Firstly, it appears that the local reduction in static pressure at stage 8 and 9 occurs simultaneously as the damaged blade passes the three sensors. The static pressure is further reduced from stage 8 to stage 9, where on the latter stage the average reduction corresponds to $\sim 2.3\%$, $\sim 3\%$ and $\sim 2.7\%$ of the specific energy for

PGV1, PGV2 and PGV3, respectively. Secondly, a small rise in static pressure is observable in the two channels preceding the damaged blade (-1, -2). Thirdly, the blade passing frequency $f_{bp}/f_n = 30$ is present for all sensors.

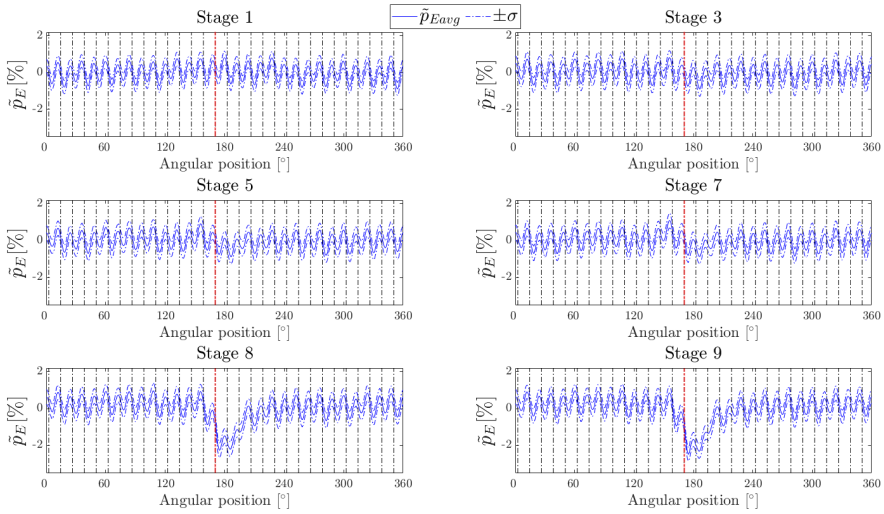

Figure 4.4: Average runner revolution at stage 0, 3, 5, 7-9, measured by PGV1 (BEP, H=30m). The red line indicates where the damaged blade (LE) passes the sensor.

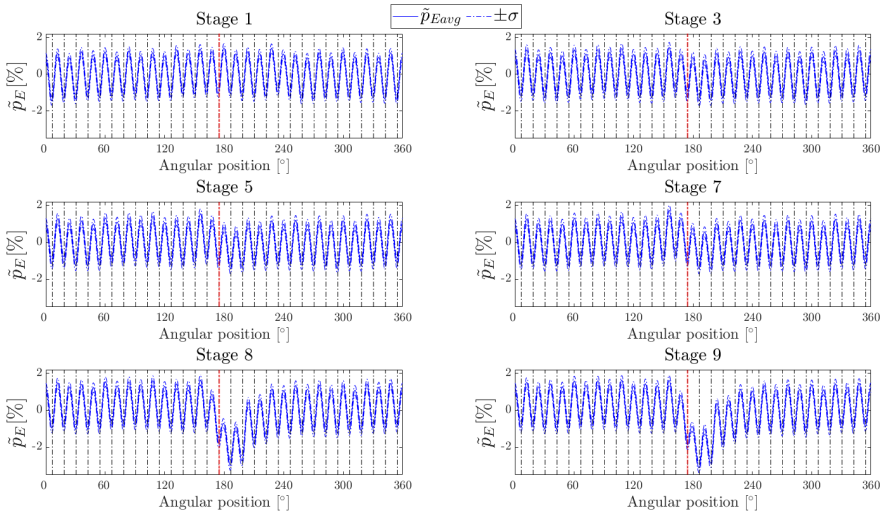

Figure 4.5: Average runner revolution at stage 0, 3, 5, 7-9, measured by PGV2 (BEP, H=30m). The red line indicates where the damaged blade (LE) passes the sensor.

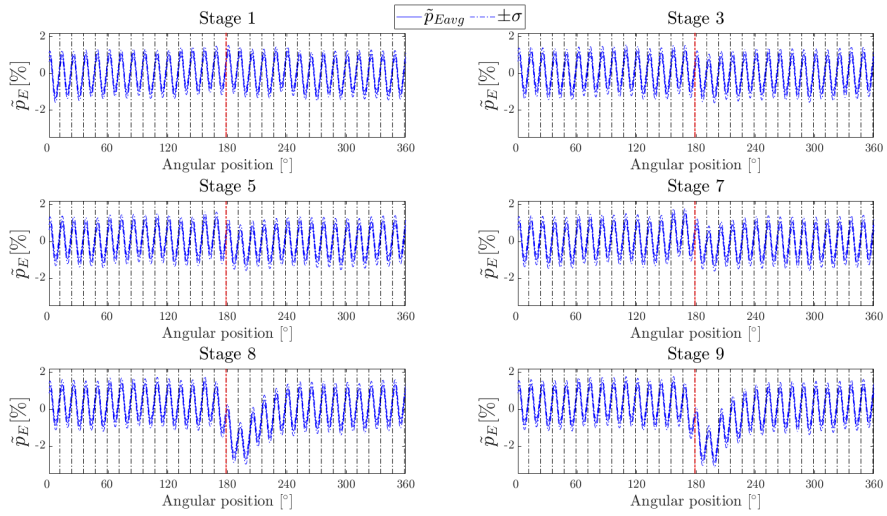

Figure 4.6: Average runner revolution at stage 0, 3, 5, 7-9, measured by PGV3 (BEP, H=30m). The red line indicates where the damaged blade (LE) passes the sensor.

In Figure 4.7, the average runner revolutions at stage 9 are presented in the same plot. The stars indicate where the LE of the damaged blade passes the respective sensors. The x-axis shows the angular position of the damaged blade.

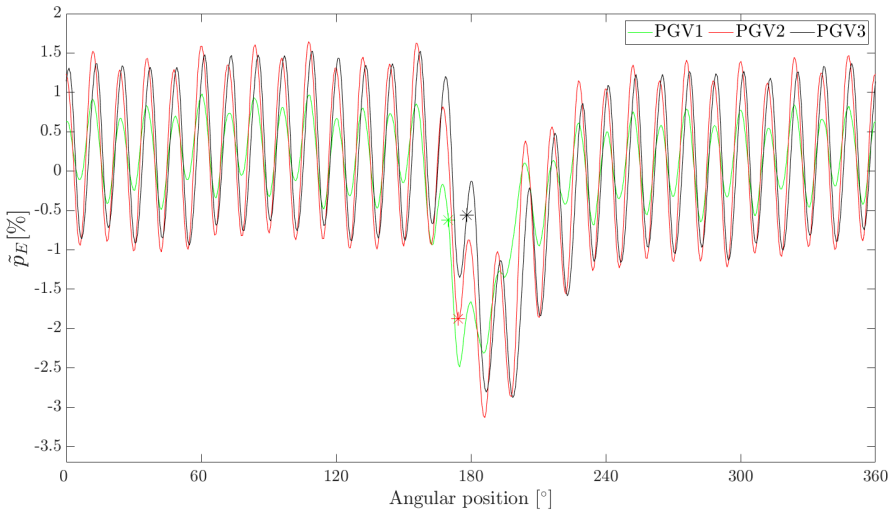

Figure 4.7: Comparison of the average runner revolutions at stage 9 for PGV1, PGV2 and PGV3 (BEP and H=30 m). The three stars indicate where the LE of the broken blade passes the respective sensors.

Upper turbine cover, PTC

The averaged runner revolutions measured by PTC at stage 0, 3, 5, 7, 8 and 9 are presented in Figure 4.8. The red dotted line indicates where the LE of the damaged blade passes the respective sensor.

A small reduction in the static pressure in every revolution can be identified in stage 8 and 9, in accordance to the position to the broken blade. This reduction corresponds to $\sim 1.3\%$ of the specific hydraulic energy. The blade passing frequency f_{bp} is also identified. The pressure signal exhibit no changes during the crack growth in stage 1-7.

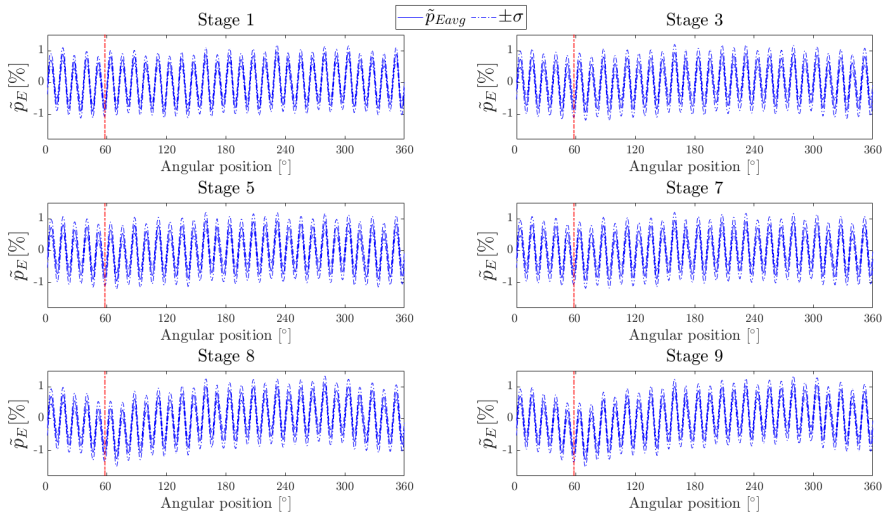

Figure 4.8: Average runner revolution at stage 0, 3, 5, 7-9, measured by PTC (BEP, H=30 m). The red line indicates where LE of the broken blade passes the sensor.

Upper draft tube cone, PDT1

In Figure 4.9, the averaged runner revolutions at stage 0, 3, 5, 7, 8 and 9, measured by PDT1 are presented. The red dotted line indicates where the TE of the damaged blade passes the sensor.

A local change in static pressure is evident at stage 8 and 9, corresponding to a rapid reduction followed by an increase. The reduction equals to $\sim 1.5\%$ of the specific hydraulic energy. Also note the high variance in the pressure signal at all stages.

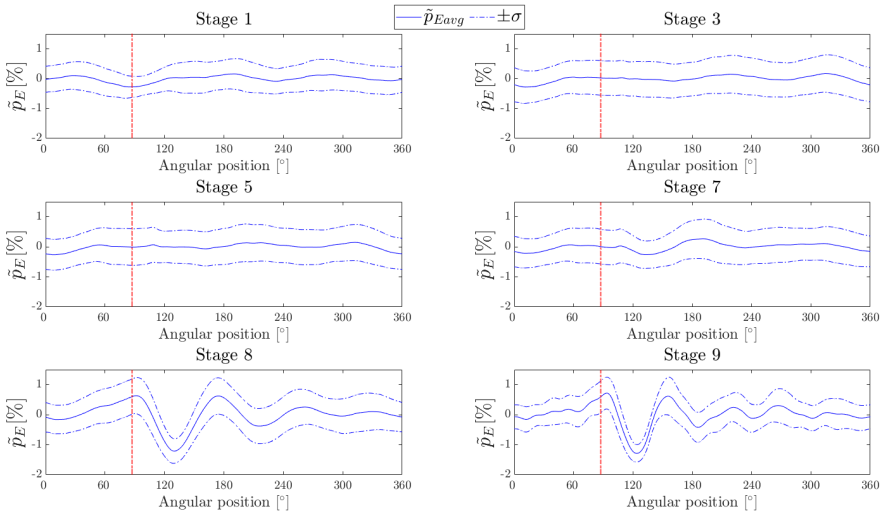

Figure 4.9: Average runner revolution at stage 0, 3, 5 and 7-9, measured by PDT1 (BEP, H=30 m). The red line indicates where TE of the broken blade passes the sensor.

4.1.2 Variation with operating point

To evaluate how the pressure signature varies over the operating range, the pressure fluctuation at stage 9 is compared for the five operating points. Figure 4.10 and 4.11 presents the average runner revolution measured by PGV2 and PDT1, respectively. Note the increase in the local pressure reduction towards higher loads for both sensors.

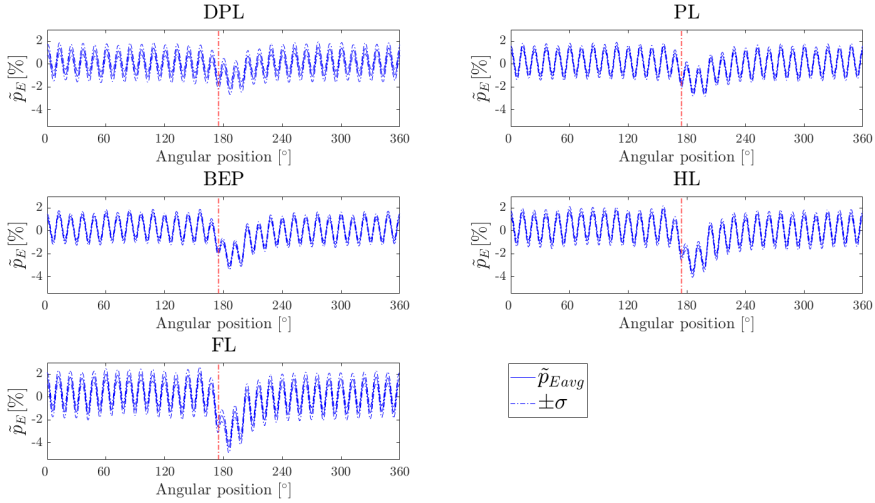

Figure 4.10: Pressure variation with operating point, measured by PGV2 at stage 9, H=30m. The red dotted line indicates where the damaged blade (LE) passes the sensor.

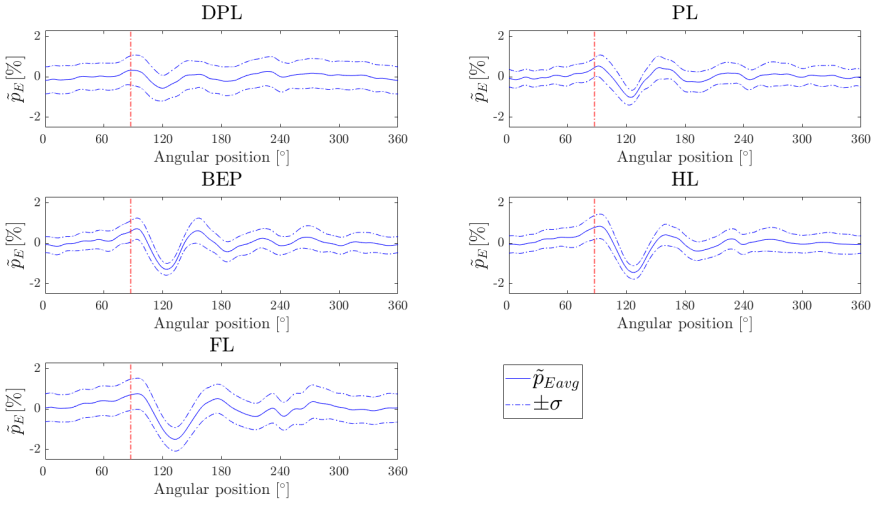

Figure 4.11: Pressure variation with operating point, measured by PDT1 at stage 9, H=30m. The red dotted line indicates where the damaged blade (TE) passes the sensor.

The local reduction in static mean pressure, $\Delta\tilde{p}_E[\%]$ measured by the pressure sensors at stage 8 and 9, for the different operating points at H=30m are summarized in Table 4.1. The values are based on the average from 530 runner revolutions and is presented with 2 decimals.

	$\Delta\tilde{p}_E[\%]$				
	DPL	PL	BEP	HL	FL
PIN	0.00/ 0.00	0.00/ 0.00	0.00/ 0.00	0.00/ 0.00	0.00/ 0.00
PTC	1.10/ 1.14	1.20/ 1.22	1.27/ 1.29	1.38/ 1.39	1.52/ 1.56
PGV1	1.86/ 1.88	1.96/ 2.01	2.26/ 2.49	3.39/ 3.56	4.01/ 4.32
PGV2	2.19/ 2.21	2.48/ 2.56	2.99/ 3.13	3.63/ 3.75	4.23/ 4.40
PGV3	2.03/ 2.06	2.30/ 2.39	2.72/ 2.88	3.47/ 3.63	4.17/ 4.33
PDT1	0.53/ 0.56	0.89/ 1.01	1.21/ 1.29	1.35/ 1.44	1.48/ 1.49
PDT2	0.38/ 0.38	0.77/ 0.74	1.13/ 1.15	1.28/ 1.32	1.40/ 1.45
PDT3	0.00/ 0.00	0.00/ 0.00	0.00/ 0.00	0.00/ 0.00	0.00/ 0.00
PDT4	0.00/ 0.00	0.00/ 0.00	0.00/ 0.00	0.00/ 0.00	0.00/ 0.00

Table 4.1: Local reduction in static pressure $\Delta\tilde{p}_E[\%]$ at stage 8/stage 9. The values are shown for all pressure sensors and all operating points at H=30m.

4.1.3 Variation with head

Figure 4.12 and 4.13 present the pressure signature at stage 9 for different heads, measured by PGV2 and PDT1, respectively. The local pressure reduction is recognizable for all heads. Notice the low frequency variation occurring at 18 m both in the vaneless space and upper draft tube cone.

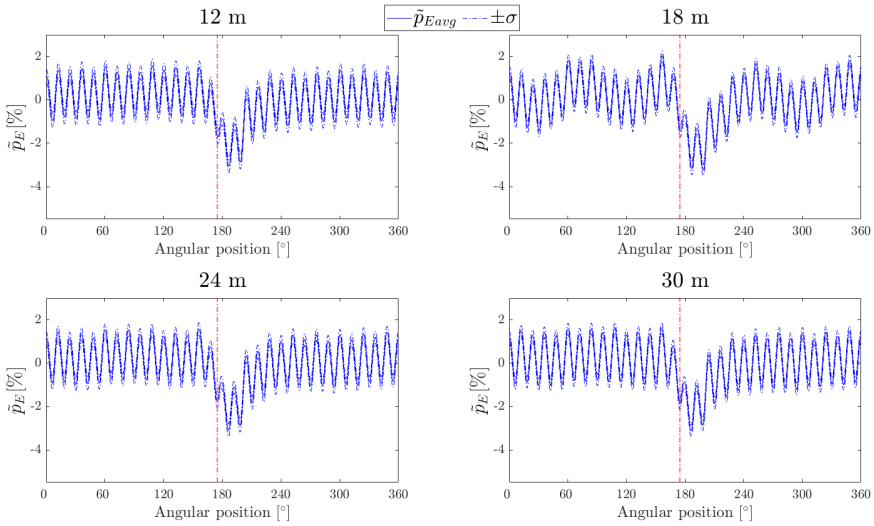

Figure 4.12: Pressure variation with head, measured by PGV2 at stage 9, BEP. The red dotted line indicates where the damaged blade (LE) passes the sensor.

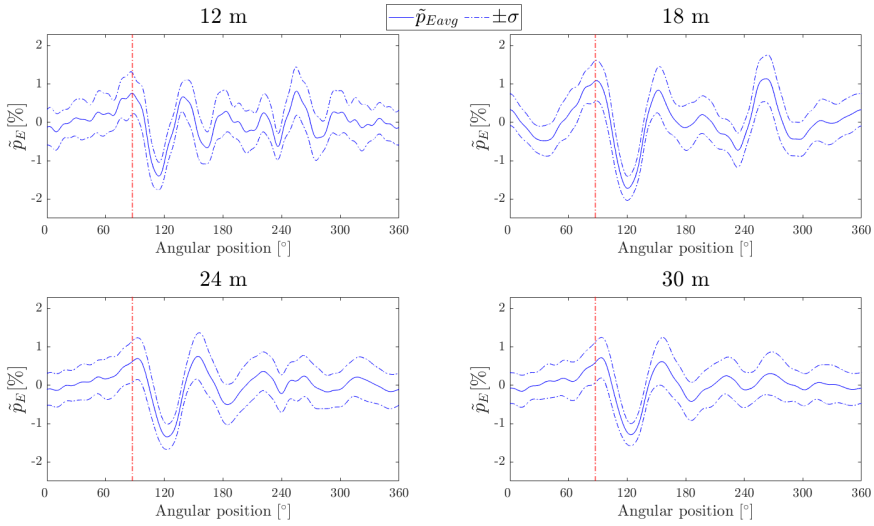

Figure 4.13: Pressure variation with head, measured by PDT1 at stage 9, BEP. The red dotted line indicates where the damaged blade (TE) passes the sensor.

4.1.4 Peak-to-peak analysis

To assess how the intensity of the pressure pulsations is affected by the damaged blade, the peak-to-peak values are compared. Figure 4.14 shows the peak-to-peak variation measured by PTC, PGV2, PDT1 and PDT3, at stage 0, 6, 7, 8 and 9. The peak-peak values are calculated from the histogram method, containing 97% of the sampled signal, and are normalized based on Equation 3.1. The discharge at the operating points are normalized based on the measured discharge at BEP. Only negligible changes in peak-peak values are observed between stage 1-5, thus these stages are omitted.

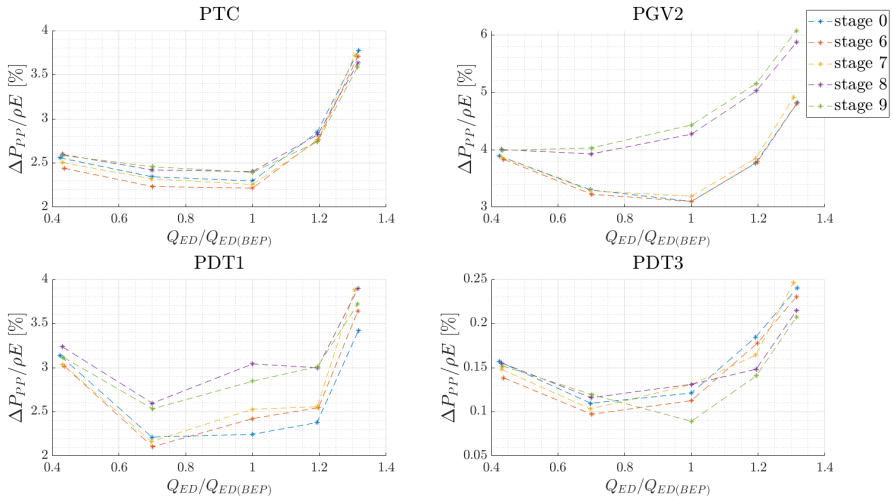

Figure 4.14: Normalized peak-peak values at stage 0 and 6-9. The values are shown for PTC, PGV2, PDT1 and PDT3.

4.2 Vibration signature in time domain

The vibration measurements in time domain measured by the two accelerometers on the turbine bearing in axial and radial direction, are presented in Figure 4.15 and 4.16. Measurements from stage 0, 7, 8 and 9 are shown. All 530 total runner revolutions are overlaid, and the signals are plotted with grey dots in a scatter plot.

No major changes can be observed in the overall vibration levels between the stages. Note the blade passing frequency, f_{bp}, which is present for both sensors and most prominent in the radial direction.

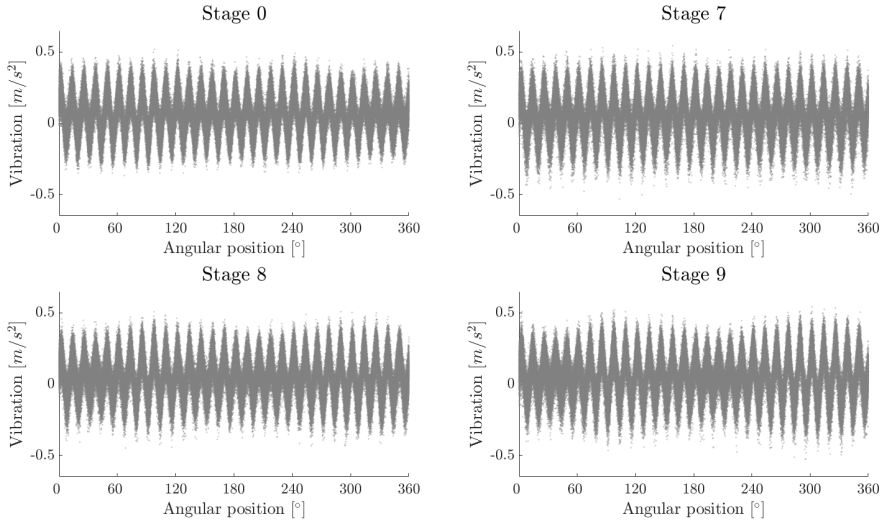

Figure 4.15: Vibration measurements of ATBR (radial direction) at BEP and H=30m. 530 runner revolutions are overlaid and shown for stage 0, 7, 8 and 9.

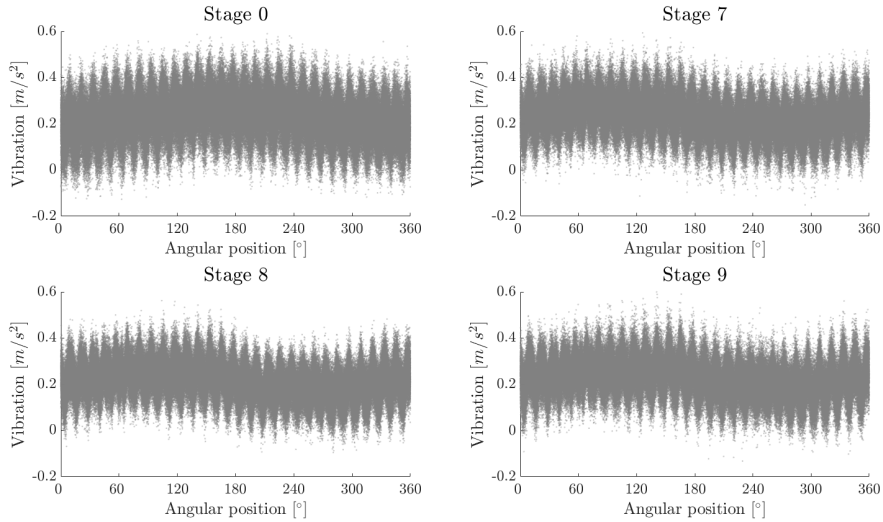

Figure 4.16: Vibration measurements of ATBA (axial direction) at BEP and H=30m. 530 runner revolutions are overlaid and shown for stage 0, 7, 8 and 9.

The variation of the vibration response measured by ATBR at stage 9 is presented for different heads in Figure 4.17.

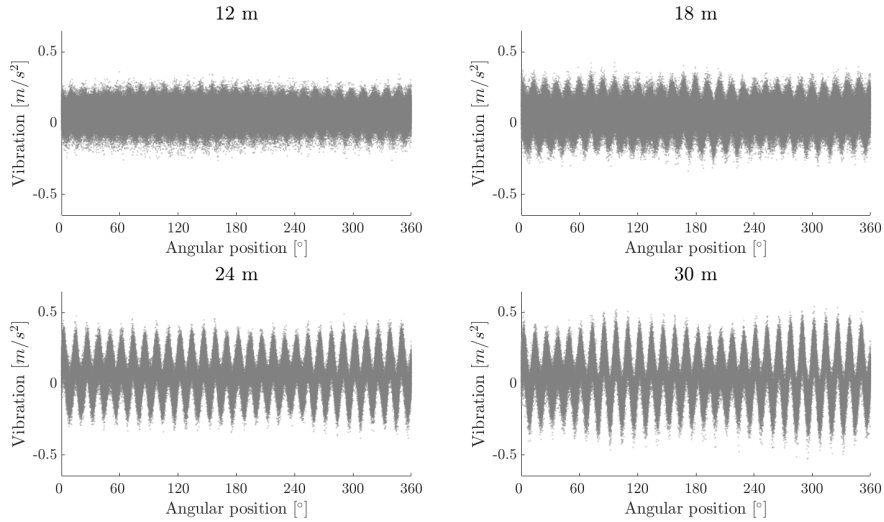

Figure 4.17: Vibration response of ATBR (radial direction) for different heads at stage 9 and BEP

4.3 Signature analysis in frequency domain

Frequency analysis has been performed to investigate how the frequency components are affected by the crack growth. The data from all stages (0-9) are structured together at a given operating point. The data is resampled as described in section 3.4, and the frequencies are normalized based on the rotating frequency at the given operating point. The analyses are shown for H=30m, with an average rotational speed of 530 rpm.

Pressure sensors

Figure 4.18 - 4.21 present the frequency spectra measured by the pressure sensors PTC, PGV2, PDT1 and PDT3, respectively. The amplitudes are normalized based on Equation 3.2 and presented on a logarithmic scale, log_{10}(normalized amplitude). The color-legend presented in Figure 4.18 applies to all figures. Frequency spectra from the omitted sensors can be found in appendix A.1.

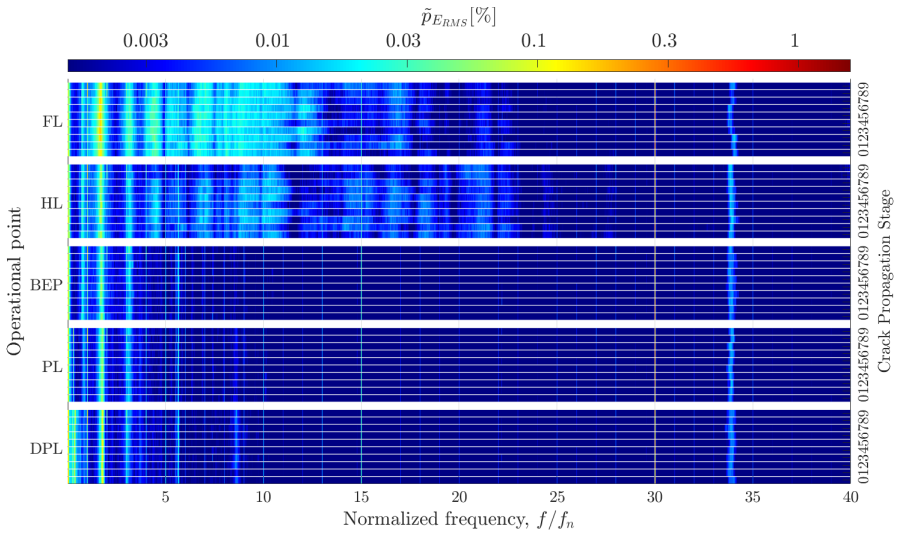

Figure 4.18: Frequency analysis measured by PTC at H=30m. Data from all crack propagation stages (0-9) are structured together at a given operating point.

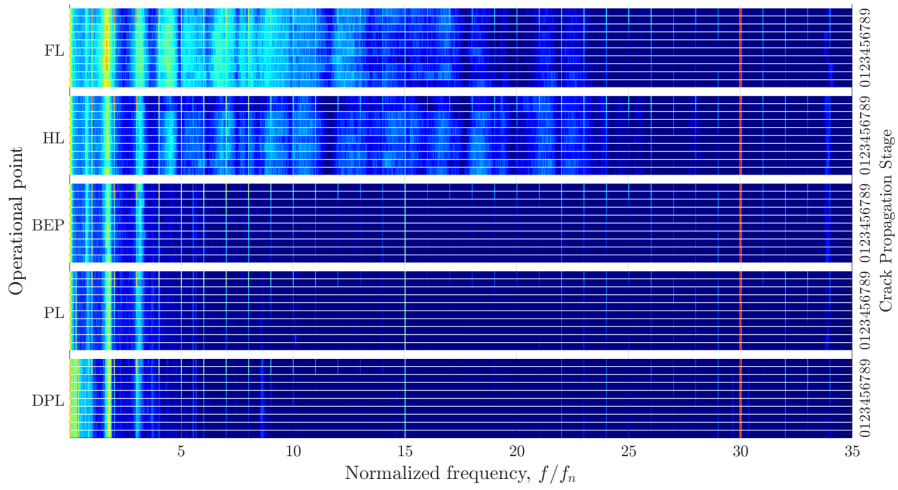

Figure 4.19: Frequency analysis measured by PGV2 at H=30m. Data from all crack propagation stages (0-9) are structured together at a given operating point.

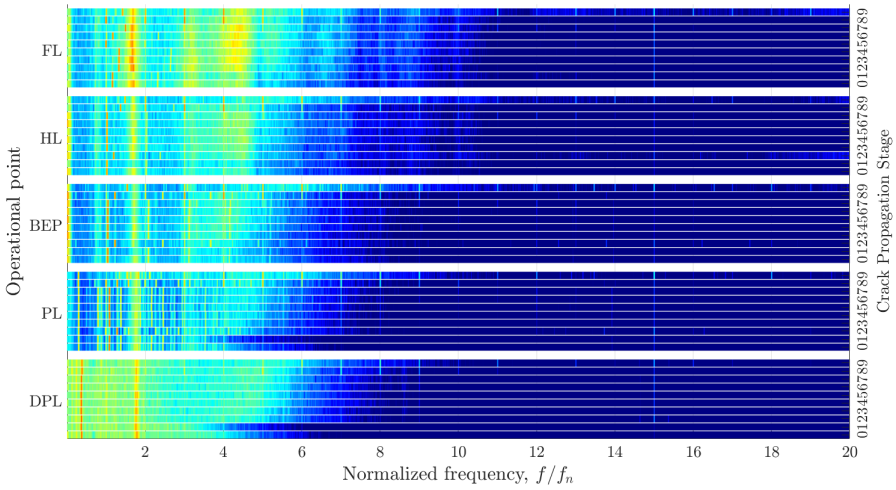

Figure 4.20: Frequency analysis measured PDT1 at H=30m. Data from all crack propagation stages (0-9) are structured together at a given operating point.

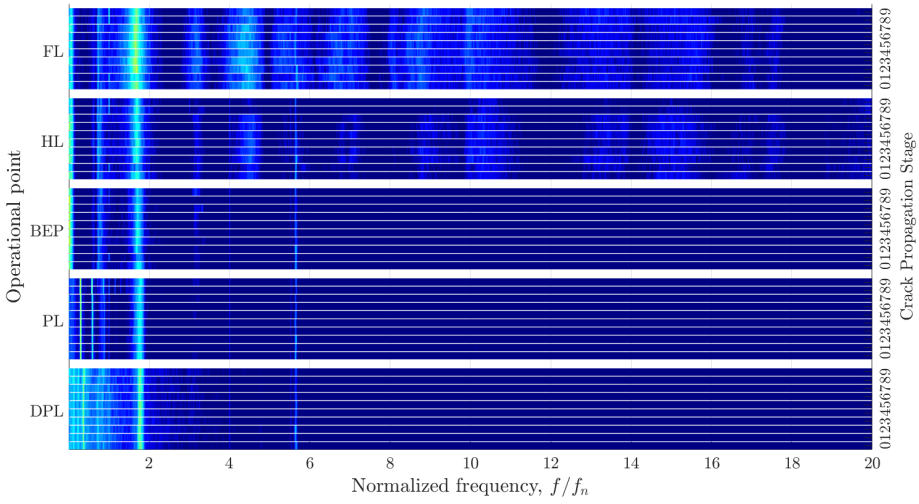

Figure 4.21: Frequency analysis measured by PDT3 at H=30m. Data from all crack propagation stages (0-9) are structured together at a given operating point.

Several frequencies are observed from the frequency spectra. The blade passing frequency, $f_{bp}/f_n = 30$, is prominent for PGV3, PTC and PDT1 at all operating points. Also the $1/2nd$ and $2nd$ harmonics are present with lower intensities. The Rheingans frequency, $f_{re}/f_n \simeq 0.278$, appears at PL on both upper and lower plane of the draft tube cone (PDT1 and PDT3). It can be seen that the amplitude of the rotating frequency $f/f_n = 1$ increases at stage 8 and 9, relative to stage 0-7. This is seen as distinct red lines and is observed for sensor PTC and PGV2, and less distinctly for PDT2. Several additional harmonics are also identified.

A comparison of the frequency spectra of PGV2 at stage 0 and 9 is presented in Figure 4.22. The data is shown for H = 30m at BEP. Note the significant increase in amplitude of the rotating frequency at stage 9, with several harmonics of decreasing intensity.

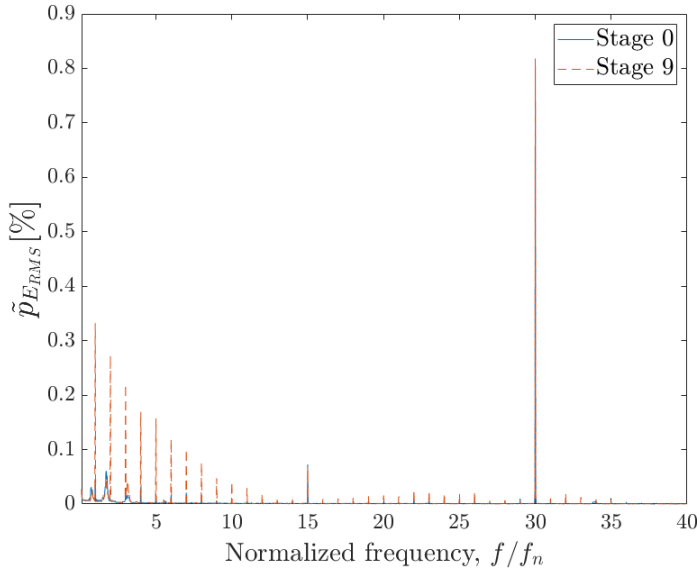

Figure 4.22: Frequency spectrum for PGV2 at BEP and H=30m, shown for stage 0 and 9

To assess the development of the rotating frequency and the amplitudes at all stages, a frequency band of $f_n \pm 0.1 f_n$ is extracted. Figure 4.23 shows the evolution at different operating points measured by sensor PTC and PGV1-3. The amplitudes remain approximately unchanged during the crack growth (stage 1-7), before a sudden increase at stage 8 and 9 occurs. In addition, the increase in amplitudes at stage 8 and 9, increases towards higher loads.

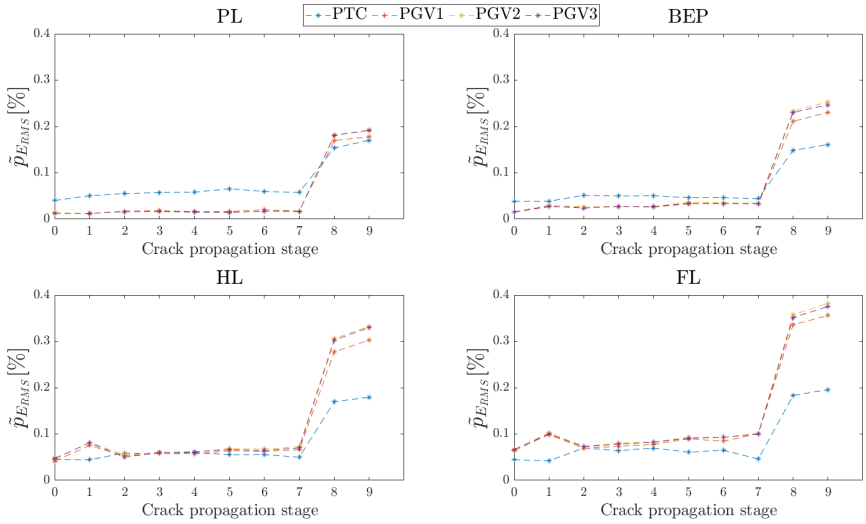

Figure 4.23: Amplitude variation of extracted f_n-band for stage 0-9. Operating point PL, BEP, HL and FL are shown for PTC, PGV1-3 at H=30m.

Vibration sensors

Figure 4.24 and 4.25 present the frequency spectra measured by the accelerometer in radial and axial directions on the turbine bearing. All stages are structured together at a given operating point and the vibration amplitudes are presented on a logarithmic scale. The amplitudes are based on the same colour-legend given in Figure 4.24. FFT-analysis for AGV is given in appendix A.2.

The blade passing frequency, f_{bp}, is present for all operating points in ATBR (radial direction) and less distinctly in ATBA (axial direction). The amplitudes are based on the color-reference presented in Figure 4.18.

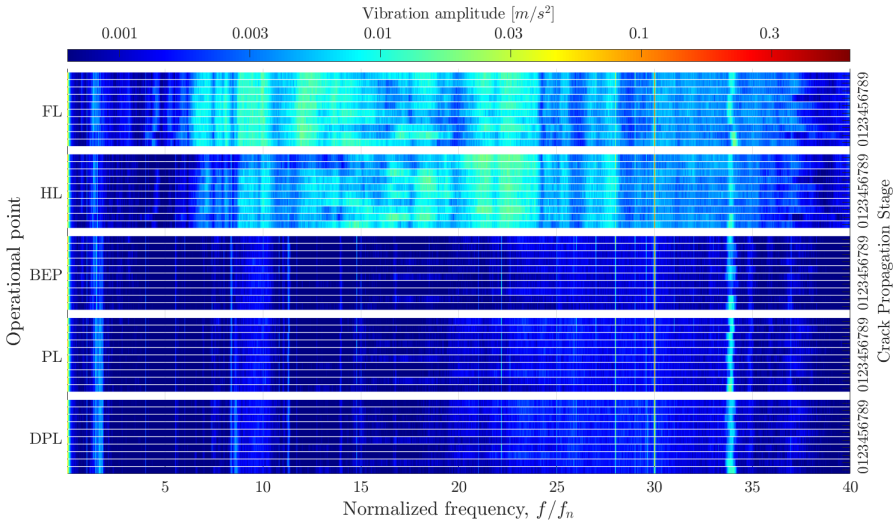

Figure 4.24: Frequency analysis of ATBR (radial direction) at H=30m. Data from all crack propagation stages (0-9) are structured together at a given operating point.

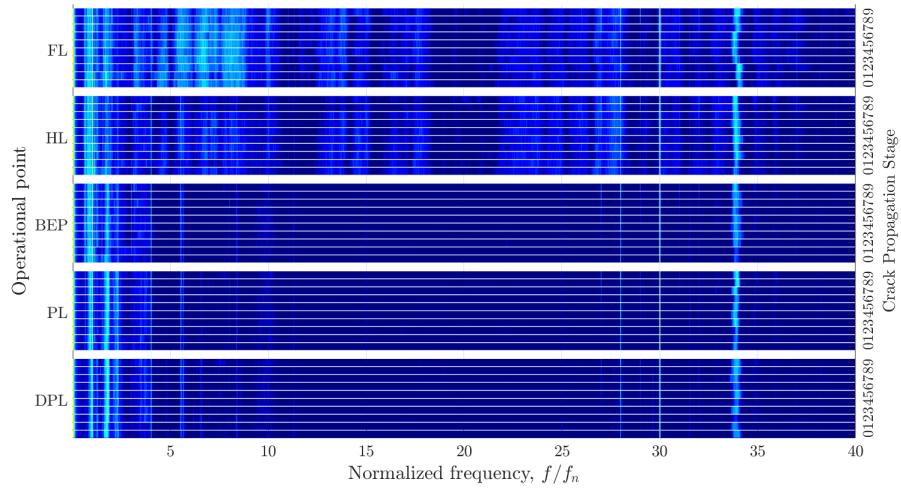

Figure 4.25: Frequency signature of ATBA (axial direction) at H=30m. Data from all crack propagation stages (0-9) are structured together at a given operating point.

A comparison of the frequency spectra at stage 0 and 9 is presented in Figure 4.26. The rotating frequency is only prominent in axial direction. Also note the increase in frequency peaks on each side of the blade passing frequency, f_{bp}, at stage 9.

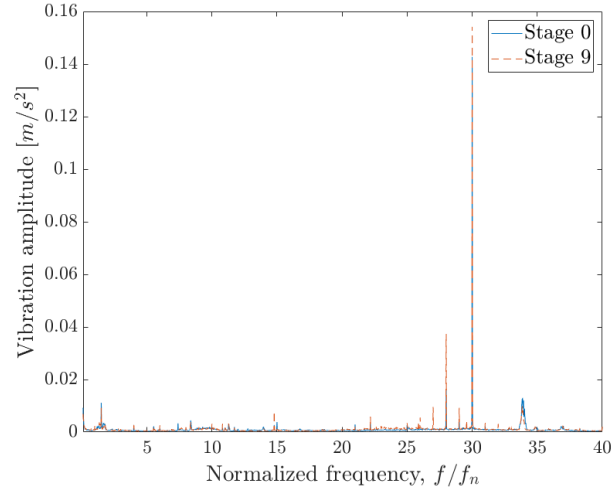

(a) ATBR (radial direction)

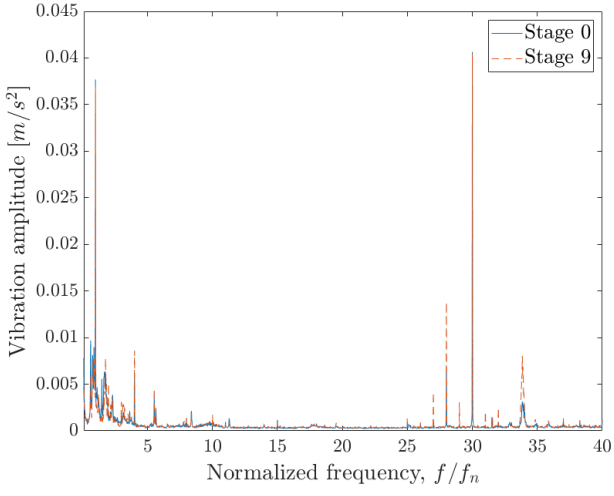

(b) ATBA (axial direction)

Figure 4.26: Comparison of the frequency spectra measured by the accelerometers in radial direction (a) and axial direction (b), at stage 0 and 9 (BEP, H=30m)

4.4 Turbine performance

To evaluate how the turbine performance is affected by the crack growth, the hydraulic efficiency evolution at H=12m was found and is presented in Figure 4.27. The different colours indicate the operational points. Due to uncalibrated operating sensors, as mentioned in section 3.5, the absolute hydraulic efficiency cannot be examined accurately. The values are therefore related to stage 0, to assess the efficiency trend during the crack growth. The grey dotted lines present the uncertainty band for all operating points at stage 0. The calculations are given in appendix B.2, where the systematic uncertainty is based on the calibration conducted by Langleite, spring 2020 [47], and the random uncertainties are estimated from the conducted measurements of this study.

There is a significant variation of the hydraulic efficiencies relative to stage 0 at the different operating points during the crack growth, and the variations are larger than the uncertainty bound. The absolute uncertainty for all operating points at stage 0 corresponds to $e_{\eta_h} = \pm 0.11\%$.

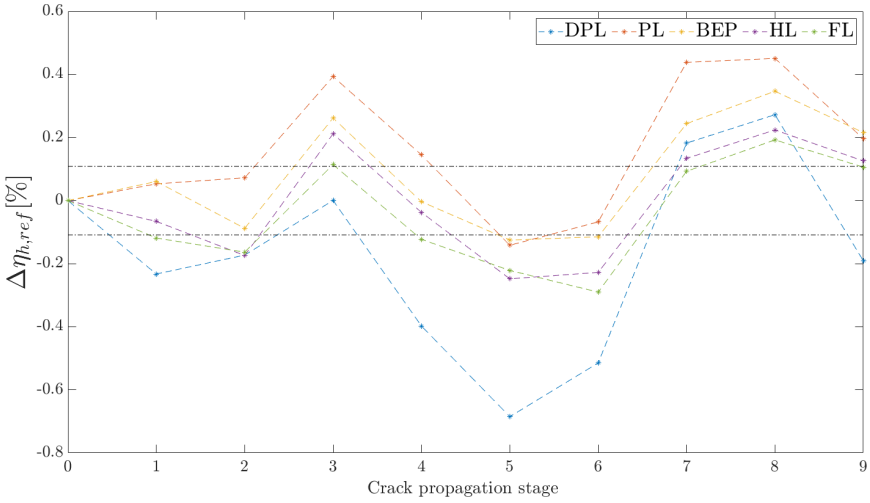

Figure 4.27: Evolution of the hydraulic efficiencies for all stages relative to stage 0 at H=12m. The different colours indicate the operating points, and the grey dotted lines present the absolute uncertainty band at stage 0.

4.5 Reference measurement

A measurement with the Francis-99 reference runner was conducted to analyse the impact of the weight difference of the two blades, as mentioned in section 3.6. The vibration measurements in time domain of the new blade at stage 0 and the reference blade are shown in Figure 4.28 for ATBA and ATBR. Figure 4.29 shows the frequency analysis of ATBA for the two blades. All measurement are taken from BEP at H=30m. Note the increase in amplitude of the rotational frequency in case of the new blade.

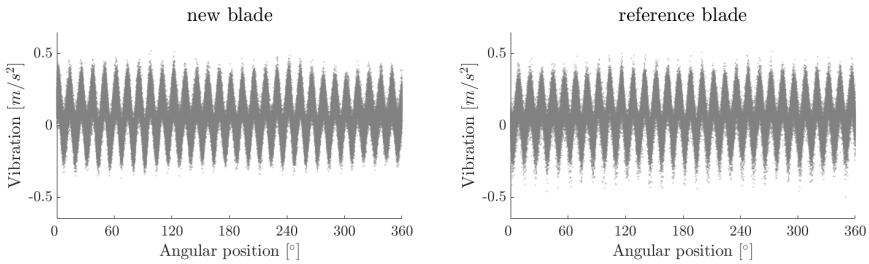

(a) ATBA

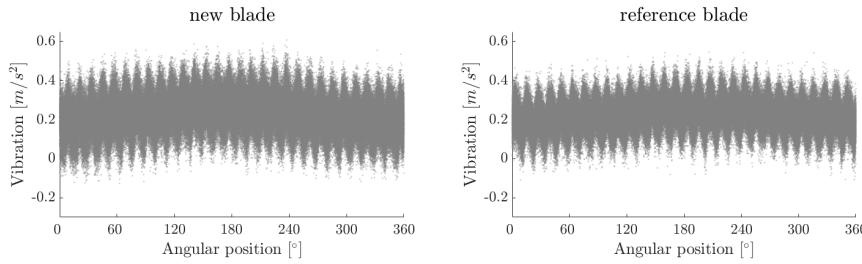

(b) ATBR

Figure 4.28: Vibration measurements of the new blade (stage 0) in 4.28(a) and the reference Francis-99 runner blade in 4.28(b), at BEP and H=30m.

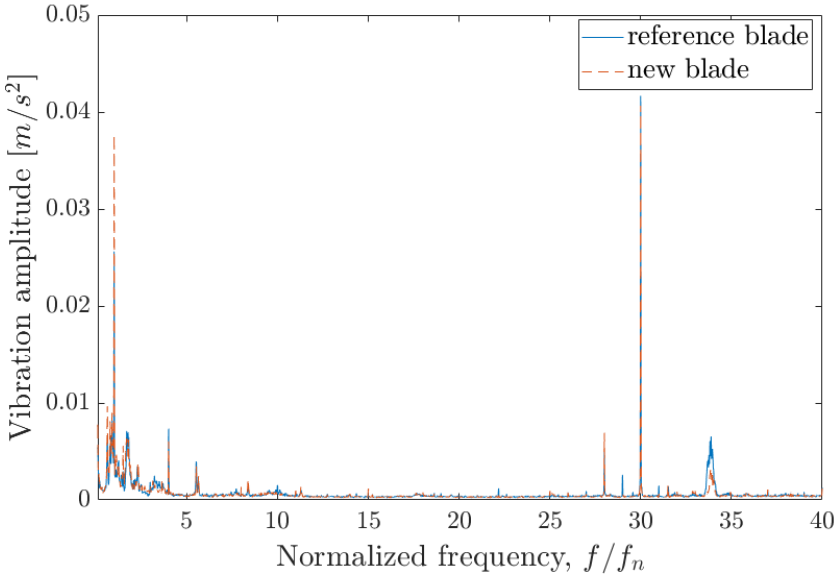

Figure 4.29: Frequency spectra measured by ATBA (axial direction) for the new blade (stage 0) and the reference blade, at BEP and H=30m.

Chapter V

Discussion

■ In this chapter the results from the experimental work will be discussed. In general, the results that demonstrate a signature change will be emphasized. The first and second parts deal with the pressure signature in the time and frequency domains. The third part involves the vibration signature and reference measurements. Finally, the transferability of the measurements and methods that were tested in this study to a possible prototype will be discussed.

5.1 Pressure signature in time domain

Both the raw data and the post-processed data reveal a change in the overall pressure trend at stage 8 and 9, after the fragment was detached from the blade. Generally, the change corresponds to a reduction in the local static pressure and appears in every runner revolution. This tendency is most prominent for the sensors close to the runner, PTC, PGV1-3, and PDT1-2.

5.1.1 Upstream of the runner

The pressure change in the vaneless space (PGV2) is characterized by distinct spikes as seen in the raw data in Figure 4.2. A similar trend is observed in the upper turbine cover (PTC) in Figure 4.1, but is less pronounced, as could be be expected due to the greater distance from the damaged blade. The pressure trend is not evident for the inlet sensor (PIN).

The local reduction in static pressure at stage 8 and 9 in the averaged runner revolution occurs immediately after the damaged blade passes the sensors in the vaneless space, and the pressure recovers quickly, as seen in Figure 4.4 - 4.6.

This difference is evidently larger than the standard deviations of the pressure oscillations. Hence, this indicates that the local pressure reduction is a direct consequence of the detached fragment, affecting only the blade channels close to the damaged blade. A similar tendency is evident in the upper turbine cover in Figure 4.8.

Small variations in the pressure signals during the crack growth (stage 1-7) can be observed in the vaneless space. As seen in Figure 4.4 - 4.6, there is a small increase in static pressure in the two preceding channels of the damaged blade (-1 and -2), followed by a local reduction in the two succeeding channels. Starting from stage 3, the rise increases with crack growth, before it suddenly decreases at stage 8. This tendency is only observed in the vaneless space. A possible reason for the pressure increase in channel -1 and -2, can be a leakage from the pressure side to the suction side of the damaged blade through the crack aperture created by the dremel.

The LE of the damaged blade passes the sensors in the vaneless space at different angular positions corresponding to the sensor locations, as seen in Figure 4.4 - 4.6. Moreover, by looking at the three averaged runner revolutions at stage 9 in the same plot in Figure 4.7, the periodic pressure oscillation passes the sensors differently relative to the position of the damaged blade. This may be explained by the fluctuating pressure field in the vaneless space with zones of higher and lower pressure caused by the guide vanes (GV). As illustrated by Agnalt, PGV1 is located in a high pressure zone close to the TE stagnation zone of the GV, PGV2 in a low pressure zone close to the suction side of the GV, while PGV3 in a slightly higher pressure zone [49]. In addition, the stationary sensors are prone to a rotating pressure field created by the runner. Consequently, the damaged blade passes PGV1 following a pressure peak, PGV2 on a pressure minimum and PGV3 right before the subsequent pressure peak. Based on this observation, the position of the damaged blade where the maximum pressure is measured by respectively PGV1, PGV2 and PGV3 is illustrated in Figure 5.1.

Furthermore, another observation from Figure 4.7, is the variation in the magnitudes of the pressure amplitudes in the vaneless space. The amplitude of the mean pressure measured by PGV1 is substantially lower than PGV2 and PGV3. Moreover, PGV1 and PGV2 exhibit a phase fluctuation, whereas PGV3 is lagging. This is most likely to be a consequence of the throttling effect created by the guide vane cascade and the splitter blade design, which was observed by Agnalt [50].

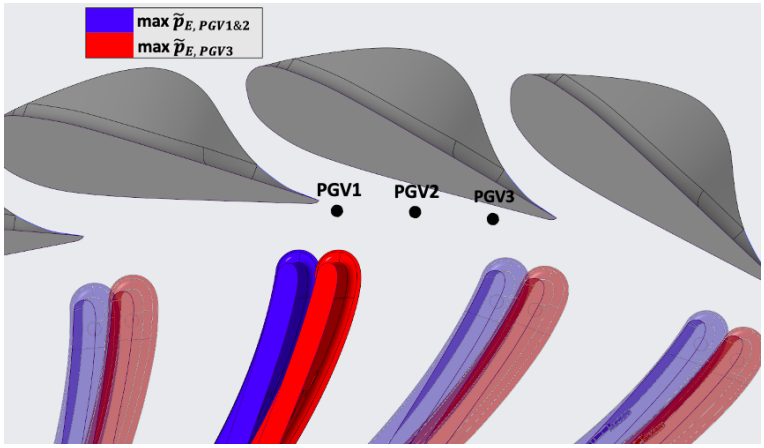

Figure 5.1: The position of the damaged blade where the maximum pressure is measured by PGV1, PGV2 and PGV3.

5.1.2 Downstream of the runner

The change in static pressure observed in the raw signal and the average runner revolution on the upper draft tube cone, in Figure 4.3 and 4.9, is recognized by a rapid reduction followed by an increase. This tendency is registered in both sensors on the upper plane (PDT1 and PDT2), but is not captured by the dynamic sensors on the lower plane (PDT3 and PDT4). This could indicate that the phenomenon caused by the damaged blade is quickly diffused. No other signature changes are observed during the crack growth (stage 1-7).

The standard deviations at each angle of the 530 combined runner revolutions measured by the sensors on the upper draft tube cone, seen in Figure 4.9, appears to be greater than the sensors upstream of the runner. A possible explanation could be that PDT1 and PDT2 are not flush-mounted, and a small column of water between the inner wall and the sensor diaphragm may disturb and dampen the fluctuations. This could also explain the poor quality of the raw signal in Figure 4.3 compared to the flush-mounted sensors in the vaneless space and upper turbine cover.

5.1.3 Possible sources of the local change in static pressure

In this section, hypotheses that may relate the local change in static pressure to the detached fragment will be presented. These aim to explain physical reasons to the observed results and are based on several assumptions.

Local channel effects

As a consequence of the detached fragment at stage 8 and 9, the TE will be situated further towards the LE, when examining a streamline crossing the opening. Considering the Francis-99 design, the shift of the TE corresponds to a small increase in the outlet diameter (D_2) and the outlet angle (β_2). As a result, the relative velocity triangles will exhibit a small change. Firstly, the peripheral velocity (u_2) will increase, due to the dependence of the outlet diameter. Secondly, the tangential component of the absolute velocity (c_{u2}) will increase, because the meriodial component (c_{m2}) remains approximately constant along a streamline [51]. A simplified illustration that demonstrates the shift in the velocity triangles at BEP is shown in Figure 5.2.

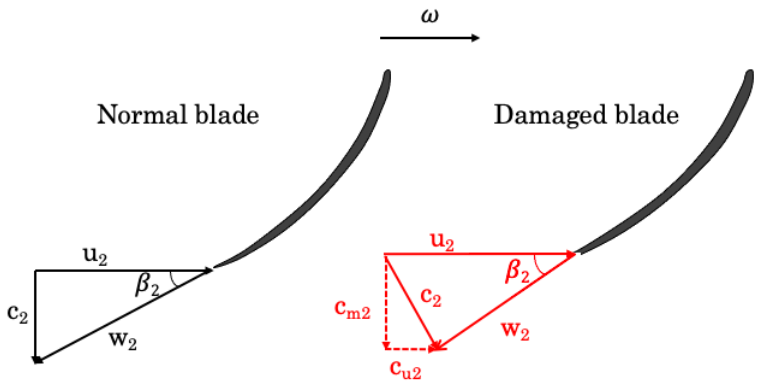

Figure 5.2: Illustration of the shift in velocity triangles from a normal blade to a damaged blade with a detached fragment

An increase in the tangential velocity component reflects a loss in extracted energy, and kinetic energy will be discharged through the draft tube. As a consequence, the dynamic pressure in the channels succeeding the damaged blade (1,2) may increase. At the same time, more shedding and secondary flows may be created as a consequence of the detached fragment, which could also contribute to a local increase in dynamic pressure. As the total pressure at the runner outlet is set by the level in the draft tube tank, this will result in a local decrease in static pressure, as seen in Equation 5.1. The reduction in static pressure observed in the vaneless space in Figure 4.5, is most evident in channels (1,2), the two channels succeeding the damaged blade. This could indicate that the effect caused by the damaged blade is an acoustic phenomena.

$$h_{total} = h_{static} + h_{dynamic} \tag{5.1}$$

The reduction in static mean pressure is greater in the vaneless space than on the upper draft tube cone. This could be explained by the proximity of the sensors in the vaneless space to the affected blade channels, whereas for the sensors on the upper draft tube cone, the local channel effect may be dampened by the neighbouring channels.

It may also be discussed whether the detached fragment causes a small local increase in discharge. In accordance to the local reduction in static pressure identified upstream of the runner, there should be a local increase in velocity. This is seen by applying the Bernoulli principle along a streamline from the spiral casing to the runner inlet, where the energy is conserved. Consequently, the respective blade channels may exhibit a small local increase in discharge, which in turn will increase the c_m-component in the velocity triangles. The flow meter did not measure any changes, and a possible local increase in discharge is assumed to be too small to be captured by the sensor.

Redistribution of loads

If the pressure reduction was purely a consequence of increased discharged kinetic energy, one would assume a slight change in the hydraulic efficiency. Due to uncalibrated operating sensors as mentioned in section 3.5, the absolute hydraulic efficiency cannot be examined accurately. However, as it appears from the efficiency evolution in Figure 4.27, variations between the stages are clearly identified and larger than the uncertainty bound, while no clear trends can be correlated to the damage. Besides, the dynamic sensors on the draft tube cone do not exhibit any pressure change, which may indicate that a possible increase in discharged kinetic energy is not substantial. Therefore, by assuming the total efficiency to be intact, the neighbouring blades may compensate the loss in extracted energy from the damaged blade, by locally increasing their load.

The opening at stage 8 and 9 will cause an earlier pressure equalization between the pressure side (PS) and suction side (SS) along a streamline crossing the detached fragment, than elsewhere. As a consequence, the two neighbouring blades may balance this equalization, seen as a pressure reduction on the neighbouring SS and a pressure increase on the neighbouring PS. An illustration of this hypothesis is presented in Figure 5.3. The distance between the two overloaded blades corresponds to 48°, which is in the same range as the local pressure change identified from Figure 4.9. In this way, the total energy extraction from the runner remains unchanged, but is extracted differently close to the damaged blade.

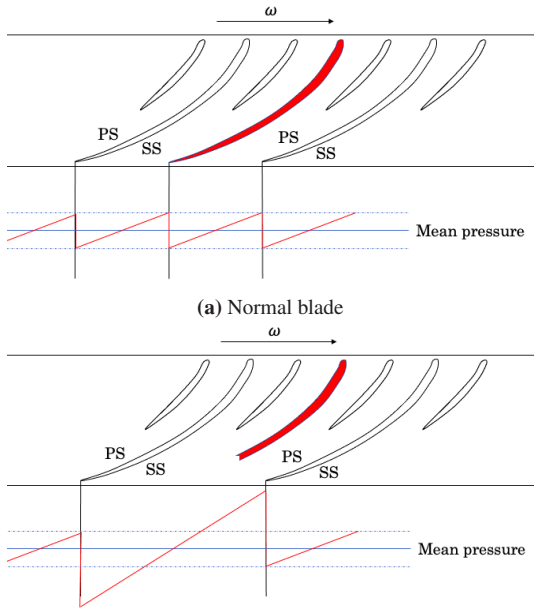

(a) Normal blade

(b) Damaged blade

Figure 5.3: Illustration of a redistribution of loads of the damaged blade, when assuming the total efficiency to be intact: pressure field at the runner outlet for normal blade (a) and damaged blade (b).

5.1.4 Variation with operating point

Several observations can be made when comparing the pressure signatures for the different operating points. Firstly, the peak-to-peak analysis seen in Figure 4.14, demonstrates that the intensity of the pressure pulsation follows a similar trend over the operating range for all sensors in normal conditions. The intensities of the pulsations are highest at loads away from BEP, characterized by unfavourable flow conditions, and reaches a minimum close to BEP. This is also recognized in the average runner revolutions at different operating points in Figure 4.10 and 4.11, where the observed standard deviations are greater outside BEP.

When comparing the local reduction in static mean pressure at different operating points, the pressure reduction exhibit an increase towards higher loads, both upstream and downstream of the runner, as seen in Figure 4.10 and 4.11. This is also evident in the peak-to-peak analysis, shown in Figure 4.14, where the relative increase in the peak-to-peak value from stage 0 to stage 8 and 9 remains unchanged

at low loads and increases significantly towards higher loads. A possible reason could be the overall blade loading, which is proportional to the torque, thereby increases with discharge. Thus, the effect from the compensating neighbouring blades should be higher with higher loads, which strengthens the hypothesis describing the redistribution of loads.

Furthermore, the reduction in static mean pressure observed on the upper draft tube cone in Figure 4.11 seems to increase more rapidly at loads lower than BEP than above. In Figure 5.4, the $\Delta\tilde{p_E}$ is plotted for varying discharge. It can be seen that the relative reduction is higher from DPL-BEP than from BEP-FL. This trend is not present in the vaneless space, which could indicate that the local variation in pressure reduction is affected by the swirling component occurring at the runner outlet when operating outside BEP, as mentioned in subsection 2.2.1. At loads lower than BEP, this swirling component will rotate with the runner, adding to the already existing c_{u2}-component, caused by the altered TE, as shown in Figure 5.2. Contrary, at loads above BEP, the swirling component will have opposite sign, and may counteract the existing c_{u2}-component.

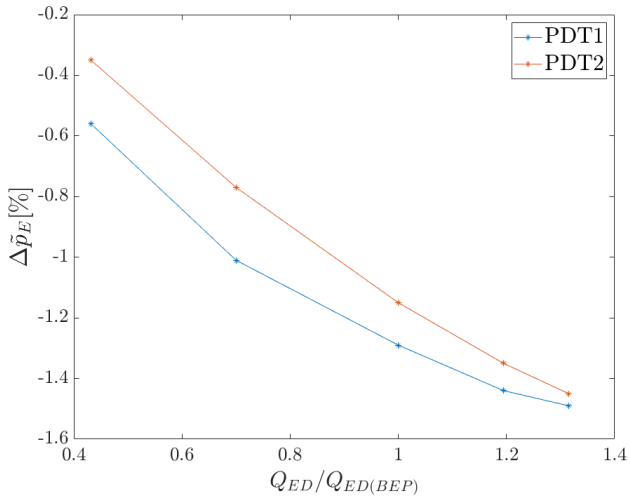

Figure 5.4: Variation in local pressure reduction $\Delta\tilde{p_E}$ at the different operating points. The flow is normalized on the discharge measured at BEP.

It can be seen from Figure 4.11, that the local pressure reduction measured by the sensor on the upper draft tube cone, is phase shifted relative to the damaged blade. This delay corresponds to 12.5 ms, substantially larger than any acoustic phenomena, and remains unchanged over the operating range. Unfortunately, no

clear trends can be found when comparing the pressure signals at different stages, as a consequence of the signal quality of the recessed sensors. However, previous CFD-analysis conducted by Iliev on the Francis-99 runner presented in Figure 5.5, reveal that the streamlines from the TE of the blades at BEP are not purely axial, which causes a lag in the pressure field relative to the sensor line [14]. This could suggest that the overall pressure signal is phase shifted, and may contribute to the lag measured by PDT1 and PDT2.

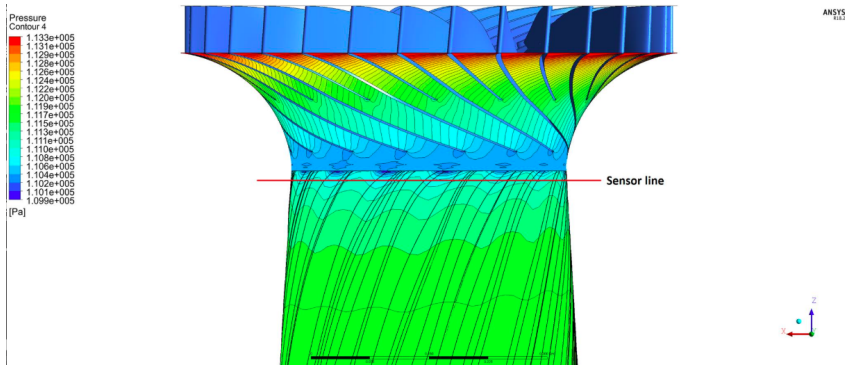

Figure 5.5: Rotating pressure field at BEP obtained from CFD-analysis of Francis-99 by Iliev [14]. Note the lag in pressure field relative to the sensor line.

5.1.5 Variation with head

Most of the results presented in section 4.1 are shown for H=30 m, as these measurements are expected to show the greatest effect of the damaged blade. Nevertheless, when comparing the pressure signature at stage 9 for different heads in Figure 4.12 and 4.13, the local pressure reduction is recognizable for all heads, with only negligible variations. The turbine is operated at homologous conditions with constant N_{ed} and Q_{ed} for all heads, and the velocity triangles therefore remain approximately constant. This supports the hypothesis of a local channel effect, with an increased c_{u2}-component being the dominant cause of the pressure reduction.

Another interesting observation from Figure 4.12 and 4.13, is the low frequency oscillation occurring at H=18 m, with 4 wave crests in one revolution. The same tendency is evident for all pressure sensors located on the turbine. This may indicate a resonance, where the runner is vibrating with nodal diameter equal to 4, which has previously been observed on the Francis-99 during resonance tests conducted by Agnalt [48]. In Figure 5.6, the averaged runner revolution at 18 m is presented for stage 0, 3, 6 and 9. The figure demonstrates that the resonance is not affected by the crack growth nor the detached fragment.

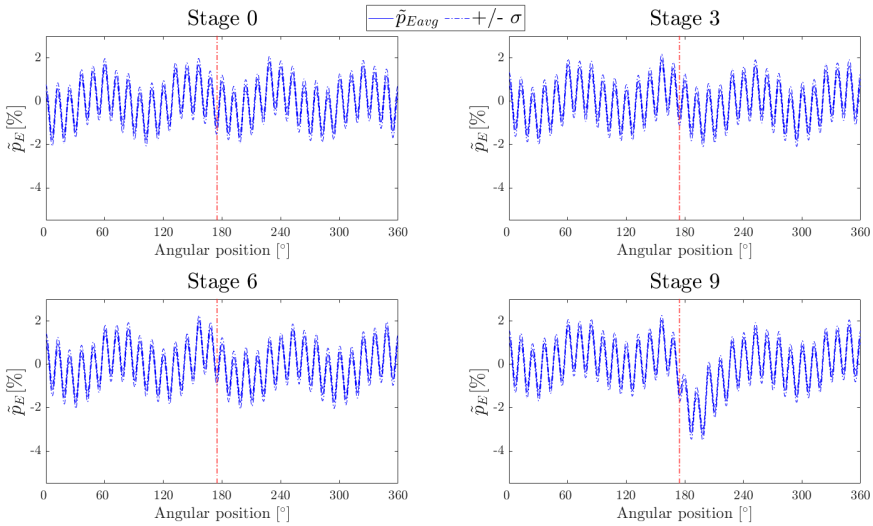

Figure 5.6: The averaged runner revolution at stage 0, 3, 6 and 9, measured by PGV2 at BEP and H=18 m. The red line indicates where the damaged blade (LE) passes the sensor.

5.2 Pressure signature in frequency domain

Stage 0 in Figure 4.19 - 4.21 show the frequency spectrum pertaining to an undamaged runner. Several of the expected frequencies explained in section 2.2 are identified. The blade passing frequency, f_{bp}/f_n = 30, and its second harmonic appears at all operating points, and is most prominent in the vaneless space (PGV2). It can also be found in the upper turbine cover (PTC) with a smaller amplitude. Due to the splitter-blade design, the frequency from the 15 full-length blades is also evident in the draft tube cone and vaneless space. The Rheingans frequency, $f_{re}/f_n \simeq 0.278$, is observed at part load in the draft tube cone, on both upper and lower plane. None of these frequencies, nor their respective amplitudes, exhibit any significant changes during the crack propagation stages.

It can be seen from the frequency spectrum of PGV2 in Figure 4.19, that the amplitude of the rotating frequency, f/f_n = 1, reaches high values at stage 8 and 9 relative to the earlier stages. Similar behaviour was also identified in PTC and PDT1-2, but less distinctly. By further analyzing the FFT from PGV2 in Figure 4.22, the amplitude increase equals to 8 times the amplitude in normal conditions. Additionally, several harmonics with decreasing amplitudes are clearly visible. A possible source can be a hydrodynamic imbalance caused by the de-

tached fragment. The flow field through the runner will no longer be symmetrical, and the irregularity may induce an impact on the stationary sensors during each revolution. This effect is expected to be more prominent at higher loads, which is identified in Figure 4.23, where the f_n-band is extracted for different operating points. By examining the amplitude at all crack propagation stages in the same figure, the amplitude remains unchanged during the crack growth (stage 1-7). This may indicate that the crack does not induce an imbalance.

A frequency measured by all sensors occurs at $f/f_n \sim 1.86$ (16-17 Hz), independent of crack growth and rotational speed, as seen in Figure 4.18. This suggests that it may originate from acoustic resonance due to standing waves in the inlet water conduit, which has previously been detected to lie in the same frequency range on the Francis rig by Trivedi [52]. The intensity is varying with operating point and is most prominent at DPL and FL, which may be due to higher fluctuations in the level of the pressure tank during the measurements.

No prominent frequencies above $f/f_n = 40(\sim$353 Hz) can be identified from the frequency analysis. This may indicate that any change in vortex shedding or possible vibrations of the damaged blade are not captured by the sensors. Furthermore, the measured frequencies are generally characterized by higher noise intensities at loads above BEP as a result of higher forces, and at low loads in the draft tube cone due to unfavourable flow conditions in the draft tube. The grid frequency at $f/f_n \sim 5.7$ (50 Hz) is most evident in the upper turbine cover. In addition, several unexpected frequencies appears. None of these exhibit any evident change during the crack growth, thus, possible sources have not been investigated.

5.3 Vibration signature

Time domain

There are no significant changes in the overall vibration levels measured by ATBR (radial direction) and ATBA (axial direction) on the turbine bearing during the crack growth, as seen in Figure 4.15 and 4.16. As it appears from Figure 4.17, the accelerometers exhibit a strong dependence on the operating pressure, and no clear trends in the signal are evident at heads below H=30m. At this head, the blade passing frequency (f_{bp}) is recognized for both sensors, in addition to a low frequency oscillation. For ATBA this corresponds to the rotational frequency, f_n, whereas for ATBR, it seems that f_{bp} is modulating the second harmonic of f_n.

Frequency domain

From the frequency spectra of ATBR and ATBA seen in Figure 4.24 and 4.25, the blade passing frequency (f_{bp}) is clearly identified, most prominent in radial

direction, as a result of the origin of the pulsation. The intensities in the frequency spectra are generally higher in radial direction than axial. Furthermore, the rotational frequency, f/f_n = 1, is present at all stages and all operating points, with slightly higher amplitude in axial direction as seen in Figure 4.26. Additionally, the frequency is more prominent for higher heads, which could indicate an existing structural instability in the Francis-99 runner, most likely a consequence of several previous measuring campaigns involving assembling and dissembling of the runner blades [4, 29]. A structural instability in the runner will affect the forces applied on the shaft and the turbine bearing and the intensity will increase with higher rotational speed. The amplitude does not seem to be affected by the detached fragment, which could indicate that the corresponding reduction in weight, is not sufficient to affect the structural instability of the runner.

By looking at the frequency spectrum at BEP in Figure 4.26, more peaks occurs on each side of f_{bp} at stage 9 relative to stage 0, in both axial and radial direction. The amplitude of these are slightly higher for higher loads. These could be side-bands of f_n, which is a symptom of a damaged runner, as discussed by Egusquiza et al. [24]. This assumes that any changes in low frequency components are modulated with the frequency of highest intensity, the carrier frequency, and occur as side-bands around this frequency in the vibration spectrum [16]. In this case, the blade passing frequency will be the carrier frequency. This could indicate that the accelerometers are slightly capturing the hydraulic imbalance created by the detached fragment.

Another observation in the frequency analysis of ATBA in Figure 4.26(b), is an increase in amplitude of $f/f_n \sim 34(\sim$300Hz) at stage 9 relative to stage 0. The frequency is also observed in the radial direction, but the amplitude remains constant throughout the crack growth. The frequency seems to be independent of the rotational speed, and could be the $6th$ harmonic of the grid frequency. A possible source is the rectifier that supplies DC-current to the generator and pump, as discussed by Kobro [53]. With a 3-phase power supply, the rectifier will create a current with a 300 Hz ripple component on the DC-side, which could excite natural frequencies in the structure.

Reference measurement

The effect of the weight reduction of the new blade on the vibration signature has been investigated. As mentioned, the new blade (stage 0) is 260 g lower than the reference blade in the Francis-99 runner. The overall vibration trend and levels remain virtually unchanged, as seen in Figure 4.28. However, as it appears from the frequency analysis in Figure 4.28(b), the amplitude of the rotational frequency is increased by 15 times when the new blade is installed. This indicates that the weight difference is clearly affecting the structural stability of the runner, which

may explain the high amplitudes of f_n which appear in all stages, identified in Figure 4.24 and 4.25.

5.4 Transferability to a prototype

The experimental findings from this work may be applicable for prototypes. This is especially true when it comes to the pressure signature recognized by the local reduction in static pressure. Several of the pressure sensor measured the change, where the sensor in the upper turbine cover (PTC) is easiest to install on a potential prototype. As the pressure reduction appears to be independent of head, there is a possibility that it may be applicable for both low and high-head turbines. However, several aspects should be taken into account when discussing the transferability of this project.

Firstly, the induced crack in this study is created to simulate a realistic case. Nevertheless, a natural crack growth will be affected by a more random nature, including local properties in the material and the operating history of the blade. Moreover, as a consequence of the cutting tool size, an air gap, with orders of magnitude larger than what can be expected in a natural crack, was present. Therefore, the pressure increase observed during the crack growth (stage 3-7) in the vaneless space, is not expected to be as evident in a realistic case of a natural crack growth.

Secondly, the Francis rig is dimensioned to withstand a pressure of 10 bar, however the maximum pressure obtained in the experiment was 3 bar. Also, the size of the shaft relative to the runner is larger than for a prototype. Consequently, the rig was rather stiff for the measurements that were made, and possible runner deformation would not be expected to produce substantial vibrations in the structure. This coincides with the vibration measurements, where only small changes were recognized in the accelerometers. A prototype will run closer to the dimensioned water pressure and possible runner instabilities are expected to produce larger vibrations relative to the structure. On the other hand, the total weight reduction due to the detached fragment will be considerably lower in a prototype relative to a model turbine.

The runner blade was inspected for possible natural crack growths between each measurement and no indications were found. A possible explanation can be the round geometry of the crack-end as a result of the ball nose cutter used by the dremel. A sharper endpoint may induce higher local stresses, thereby increasing the possibility of further fracturing. Besides, the runner blade used for this study was recently produced with high quality brass alloy. Therefore, the blade should not be prone to any wear or local weaknesses that could affect the crack growth. This will not be the case for a prototype that has been in operation for over 20 years.

Chapter VI

Conclusion

Ten measurement campaigns have successfully been performed on the Francis turbine test rig at the Waterpower Laboratory, each including five operating points at four different heads. Nine stationary pressure sensors and three accelerometers were located on different parts of the turbine. Between each campaign, a crack was manually developed along a semi-elliptical path on the trailing edge of one blade close to the shroud, resulting in a fully realised fragment being cut out. The presence of the detached fragment, simulating a so-called shark-bite fatigue failure, was successfully identified by use of the sensors. Analyses of the pressure and vibration signatures in the time and frequency domains, suggest a number of key findings:

- A local reduction in static pressure occurred for each runner revolution after the fragment was detached. This reduction was prominent in the vaneless space and on the upper draft tube cone, and to some extent in the upper turbine cover. The reduction was greater with higher loads, and remained unaffected by the head. The maximum reduction in static mean pressure was 4.4% of the specific hydraulic energy. A combination of local flow effects in the channel and a redistribution of the loads of the damaged blade, is believed to be the cause.
- In the frequency analysis of the pressure signals, the amplitude of the rotational frequency and several harmonics increased after the fragment was detached. The amplitudes increased towards higher loads, and is probably a consequence of a hydraulic imbalance caused by the damaged runner. The effect was observed both upstream and downstream of the runner.
- In the frequency analysis of the vibration signals, the rotational frequency was evident during all measurement campaigns, most likely due to an existing structural instability in the runner and a weight difference between the

new and the reference blade. In addition, an increase in side-bands around the blade passing frequency occurred after the fragment was detached, probably a consequence of a hydraulic imbalance.

- The prominent frequencies observed under normal conditions are consistent with the characteristic frequencies occurring on a Francis turbine. The RSI blade passing frequency was prominent at all operating points for all pressure sensors upstream of the runner and the accelerometers, while the Rheingans frequency was evident in the draft tube cone during part load operation. None of these were correlated with the crack growth.

- Only a minor change in the static pressure occurred during the crack growth, before the fragment was detached. This is believed to be caused by the crack aperture created by the cutting tool, which is not considered to occur in a realistic fatigue case. No changes in the overall vibration levels measured by the accelerometers were observed during the crack growth.

The flexible operation of hydropower plants is expected to continue in the future, which could give greater challenges concerning fatigue failure on Francis runners. The results of this study indicate that stationary pressure sensors and accelerometers can be used to identify a fractured fragment on a runner during operation. Even though no clear change in the signature during the crack growth was observed, the conducted measurement cannot exclude the possibility of being able to monitor crack development.

6.1 Further work

Numerical analysis is essential to obtain further insight in how the pressure and flow fields are affected by a crack growth. This could provide a more detailed basis when relating physical phenomena to the damage. To further investigate the change in dynamic behaviour of the runner with increasing crack length, modal analysis of the model runner is recommended.

The focus of this work has been to investigate if and how a damage on a runner blade is possible to identify with vibration and pressure measurements. To further examine the local and global signature changes, new measurement campaigns with a carefully designed measurement set-up are recommended. For this test, pressure sensors on-board the runner and flush mounted sensors on the upper draft tube cone, should be included. In addition, complete calibration of the operating sensors and a detailed uncertainty evaluation should be conducted, to more accurately assess the affect of a crack growth on the turbine performance. It is also recommended

to explore the use of finer cutting-tools, in order to recreate an even more realistic crack growth.

This study may provide example data and results for developing more advanced machine learning algorithms for fault detection on Francis runners.

References

[1] E, A., 2017, "HiFrancis - Final report WP1.3," Tech. rep., NTNU.

[2] NKVS, 2014, "Francis-99 First Workshop," https://www.ntnu.edu/nvks/f99-numerical-study

[3] IEC60193, 1999, *Hydraulic turbines, storage pumps and pump-turbines - Model acceptance tests*, 1st ed., International Electrotechnical Commission.

[4] Kobro, E., 2010, "Measurement of Pressure Pulsations in Francis Turbines," Ph.D. thesis, NTNU.

[5] Gogstad, P., 2017, "Experimental investigation and mitigation of pressure pulsations in Francis turbines," Ph.D. thesis, NTNU.

[6] Neidhardt, T., Jung, A., Hyneck, S., and Gummer, J., "An alternative approach to the Von Karman vortex problem in modern hydraulic turbines," .

[7] Sannes, D., 2017, "Pressure Pulsations and Stresses in a Francis Turbine Operating at Variable Speed," Master's thesis, NTNU.

[8] Bergan, C., 2019, "Dynamic Loads on Francis Turbines - An Experimental Study," Ph.D. thesis, NTNU.

[9] Liu, X., Luo, Y., and Wang, Z., 2016, "A review on fatigue damage mechanism in hydro turbines," Renewable and Sustainable Energy Reviews, **54**, pp. 1–14.

[10] Coutu, A., Roy, M. D., Monette, C., and Nennemann, B., 2008, "Experience with Rotor-Stator interactions in high head Francis runner," .

[11] Fjærvold, K.-T., "Sprekker i nye Francisløpehjul sett i lys av spenninger og trykkpulsasjonsmålinger," .

[12] Heinzel, R. and Schilling, 2002, "Spectrum and spectral density estimation by the Discrete Fourier transform DFT including a comprehensive list of window functions and some new flat tops windows," Tech. rep., Max Planck Institut fur Gravitationphysic Teilinstitut Hannover.

[13] Bergan, C., 2013, "Trykkpulsasjoner i Francisturbiner - Prosjektoppgave," .

[14] Igor, I., 2021-01-13, personal communication.

[15] Seidel, U., Mende, C., Hübner, B., Weber, W., and Otto, A., 2014, "Dynamic loads in Francis runners and their impact on fatigue life," IOP Conference Series: Earth and Environmental Science, **22**, p. 032054.

[16] Valentin, D., Presas, A., Valero, C., and Egusquiza, E., 2019, "Detection of Hydraulic Phenomena in Francis Turbines with Different Sensors," Sensors, **19**, p. 4053.

[17] Huang, X., Chamberland-Lauzon, J., Oram, C., Klopfer, A., and Ruchonnet, N., 2014, "Fatigue analyses of the prototype Francis runners based on site measurements and simulations," IOP Conference Series: Earth and Environmental Science, **22**, p. 012014.

[18] Trivedi, C., Agnalt, E., Dahlhaug, O., and Brandastro, B., 2019, "Signature analysis of characteristic frequencies in a Francis turbine," IOP Conference Series: Earth and Environmental Science, **240**, p. 072008.

[19] Zhang, M., Valentin, D., Valero, C., Egusquiza Montagut, M., and Egusquiza, E., 2019, "Failure investigation of a Kaplan turbine blade," Engineering Failure Analysis, **97**.

[20] Frunzaverde, D., Muntean, S., Marginean, G., Câmpian, V., Marsavina, L., Terzi, R., and Şerban, V., 2010, "Failure analysis of a Francis turbine runner," IOP Conference Series: Earth and Environmental Science, **12**, p. 012115.

[21] Gummer, J. and Etter, S., 2008, "Cracking of Francis runners during transient operation," **15**, pp. 81–85.

[22] Egusquiza, E., Valero, C., Huang, X., Jou, E., Guardo-Zabaleta, A., and Rodriguez, C., 2012, "Failure investigation of a large pump-turbine runner," Engineering Failure Analysis, **19**, pp. 27–34.

[23] Østby, P. T. K., "Dynamic stresses in High Head Francis Turbines," Ph.D. thesis, NTNU.

[24] Egusquiza, E., Valero, C., Valentin, D., Presas, A., and Rodriguez, C., 2015, "Condition monitoring of pump-turbines. New challenges," Measurement, **67**.

[25] Åsnes, A., 2018, "Condition Monitoring of Hydroelectric Power Plants," Master's thesis, NTNU.

[26] Welte, T., 2008, "Deterioriation and Maintenance Models for Components in Hydropower plants," Ph.D. thesis, NTNU.

[27] Welte, T. and Foros, J., 2019, "MonitorX - Final report," Tech. rep., Energi Norge AS.

[28] Støren, G., Dahlhaug, O., and Solemslie, B., 2020, "Signature Investigation of Typical Faults on Francis Turbines Signature Investigation of Typical Faults on Francis Turbines," Journal of Physics Conference Series, **1608**, p. 12003.

[29] Agnalt, E., 2019, "Rotor Stator Interaction in Low Specific Speed Francis Turbines," Ph.D. thesis, NTNU.

[30] Zhang, M., Valentin, D., Valero, C., Egusquiza Montagut, M., and Zhao, W., 2018, "Numerical Study on the Dynamic Behavior of a Francis Turbine Runner Model with a Crack," Energies, **11**, p. 1630.

[31] Georgievskaia, E., 2020, "Effect of cracks on dynamic parameters and lifetime of hydraulic units," **22**, pp. 229–234.

[32] Støren, G., 2020, "Analytics of data from hydropower turbines for anomality and condition prediction - Specialization Project," .

[33] Brekke, H., 2003, "Pumper og Turbiner," .

[34] Igor, I., 2020, "Francis Turbines for Variable Speed Operation," Ph.D. thesis, NTNU.

[35] Kjølle, A., 2001, "Hydropower in Norway - Mechanical Equipment," NTNU, Compendium.

[36] Tanaka, H., 2011, "Vibration Behavior and Dynamic Stress of Runners of Very High Head Reversible Pump-turbines," International Journal of Fluid Machinery and Systems, **4**, pp. 289–306.

[37] Döfler, P., Sick, M., and Coutu, A., 2013, *Flow-Induced Pulsation and Vibration in Hydroelectric Machinery*, Springer.

[38] Brekke, H., 2010, "A Review on Oscillatory Problems in Francis Turbines," .

[39] Dowling, N. E., *Mechanical Behavior of Materials: Engineering Methods for Deformation, Fracture, and Fatigue*, 4th ed., Pearson Education.

[40] Huth, H.-J., 2005, "Fatigue Design of Hydraulic Turbine Runners," Ph.D. thesis, NTNU.

[41] Schijve, J., *Fatigue of Structures and Materials*, 2nd ed., Springer.

[42] Proakis, J. and Manolakis, D., 2006, *Digital Signal Processing*, 4th ed., Pearson.

[43] Kjolle, A., 2003, "Hydraulisk Måleteknikk," .

[44] Solemslie, B., 2010, "Compendium in Instrumentation, Calibration and Uncertainty Analysis," .

[45] Wheeler, A. J. and Ganji, A. R., *Introduction to Engineering Experimentation*, 2nd ed., Pearson Education.

[46] Agnalt, E., Solemslie, B., and Dahlhaug, O., 2019, "Onboard measurements of pressure pulsations in a low specific speed Francis model runner," IOP Conference Series: Earth and Environmental Science, **240**, p. 022040.

[47] Langleite, G. M. K., "Test of Francis turbine with variable speed operation," Master's thesis.

[48] Agnalt, E., Østby, P., Solemslie, B., and Dahlhaug, O., 2018, "Experimental Study of a Low-Specific Speed Francis Model Runner during Resonance," Shock and Vibration, **2018**.

[49] Agnalt, E., Solemslie, B., Storli, P.-T., and Dahlhaug, O., 2020, "The Rotor-Stator Interaction Onboard A Low Specific Speed Francis Turbine," International Journal of Fluid Machinery and Systems, **13**, pp. 302–309.

[50] Agnalt, E., Iliev, I., Solemslie, B., and Dahlhaug, O., 2019, "On the Rotor Stator Interaction Effects of Low Specific Speed Francis Turbines," International Journal of Rotating Machinery, **2019**, p. 11.

[51] H, F., K, H., E, K., J, R., and P, S., 2009, "High Pressure Hydraulic Machinery," .

[52] Trivedi, C., Cervantes, M., Gandhi, B., and Dahlhaug, O., 2014, "Transient Pressure Measurements on a High Head Model Francis Turbine During Emergency Shutdown, Total Load Rejection, and Runaway," Journal of Fluids Engineering, **136**.

[53] Einar, K., 2006, "Trykkpulsasjoner i Francisturbiner," Master's thesis, NTNU.

Appendix - A

Additional results

A.1 Pressure measurements

A.1.1 Raw pressure data

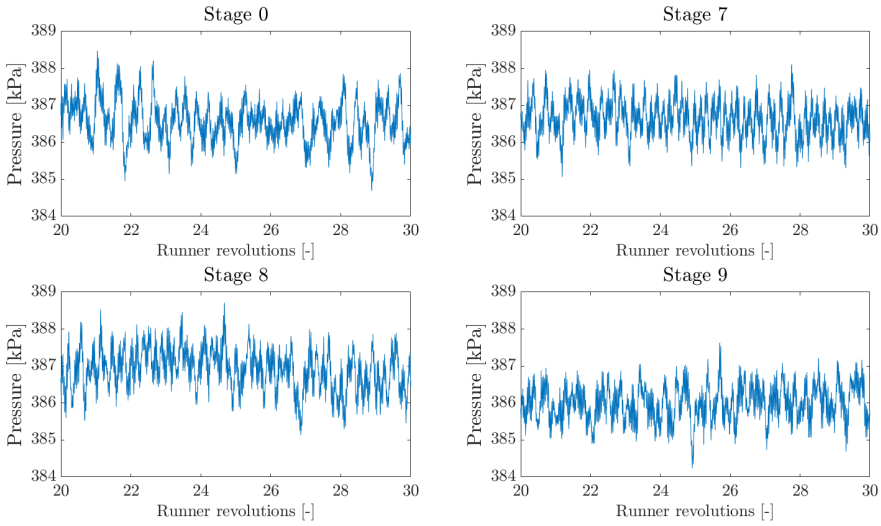

Figure A.1: Raw pressure data measured by PIN at BEP and H=30 m. 10 runner revolutions from stage 0, 7, 8 and 9 are shown

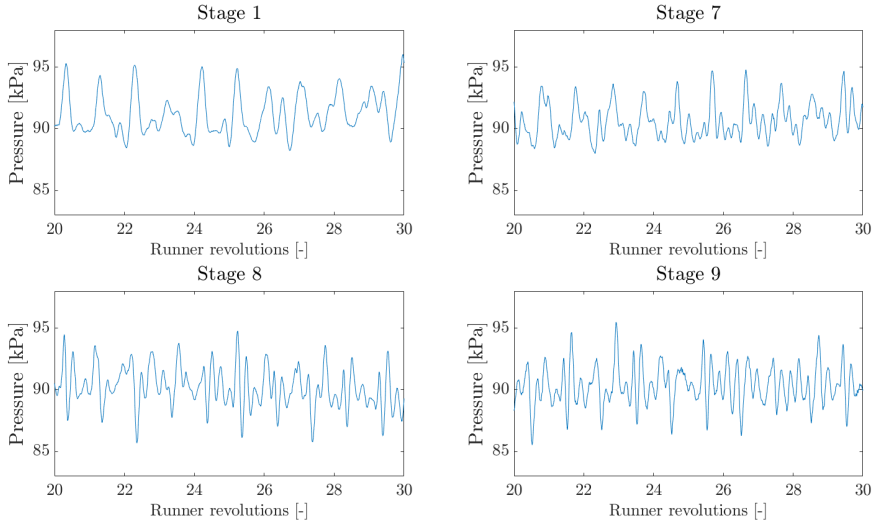

Figure A.2: Raw pressure data measured by PDT2 at BEP and H=30 m. 10 runner revolutions from stage 0, 7, 8 and 9 are shown

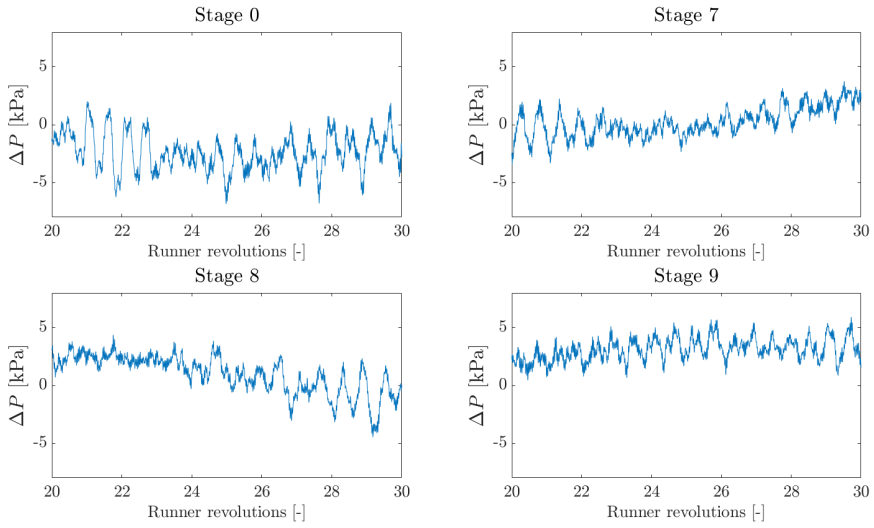

Figure A.3: Raw pressure data measured by PDT3 at BEP and H=30 m. 10 runner revolutions from stage 0, 7, 8 and 9 are shown

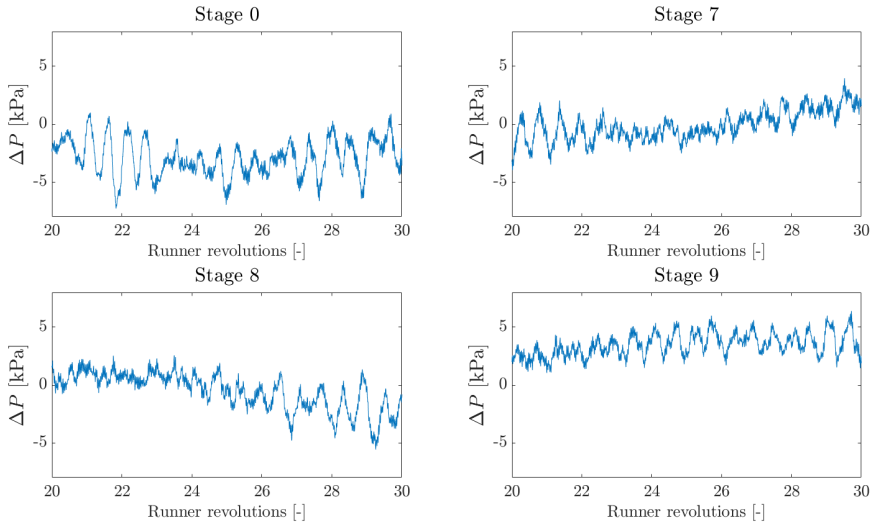

Figure A.4: Raw pressure data measured by PDT4 at BEP and H=30 m. 10 runner revolutions from stage 0, 7, 8 and 9 are shown

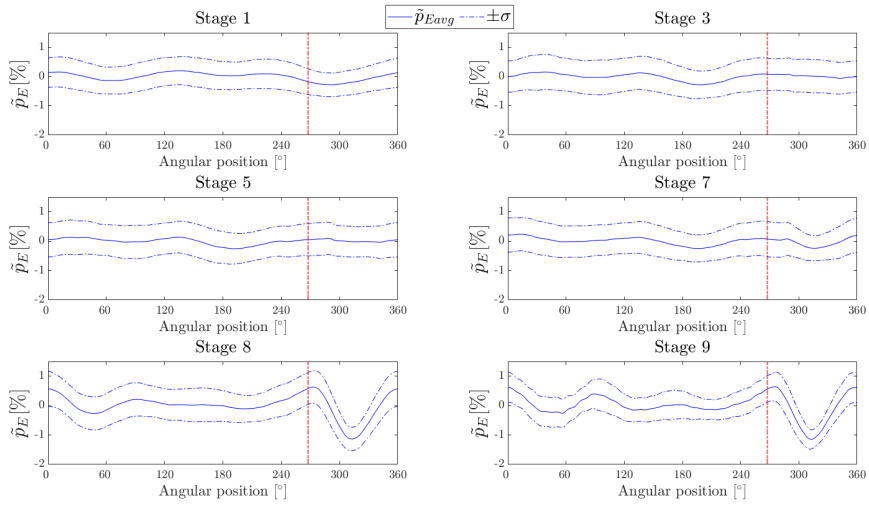

Figure A.5: Average runner revolution at stage 0, 3, 5 and 7-9, measured by PDT2 (BEP, H=30 m). The red line indicates where TE of the broken blade passes the sensor.

A.1.2 Variation with operating point

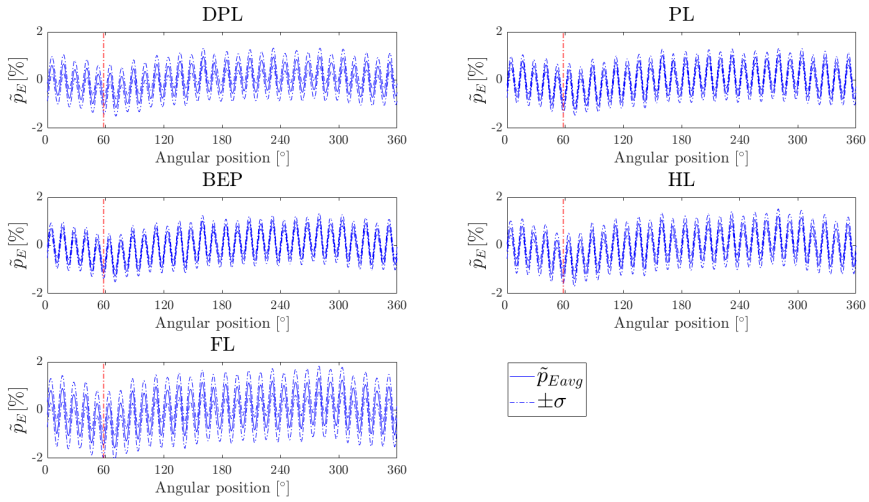

Figure A.6: Pressure variation with operating point, measured by PTC at stage 9, H=30m. The red dotted line indicates where the damaged blade (LE) passes the sensor.

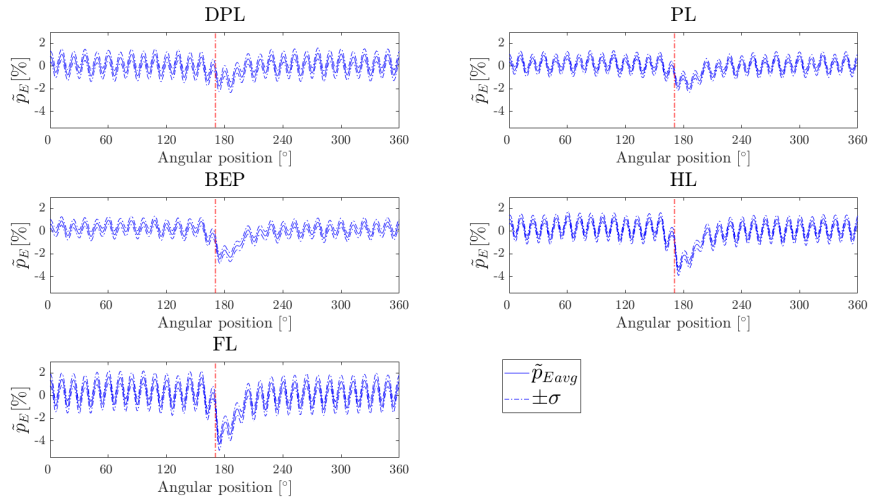

Figure A.7: Pressure variation with operating point, measured by PGV1 at stage 9, H=30m. The red dotted line indicates where the damaged blade (LE) passes the sensor.

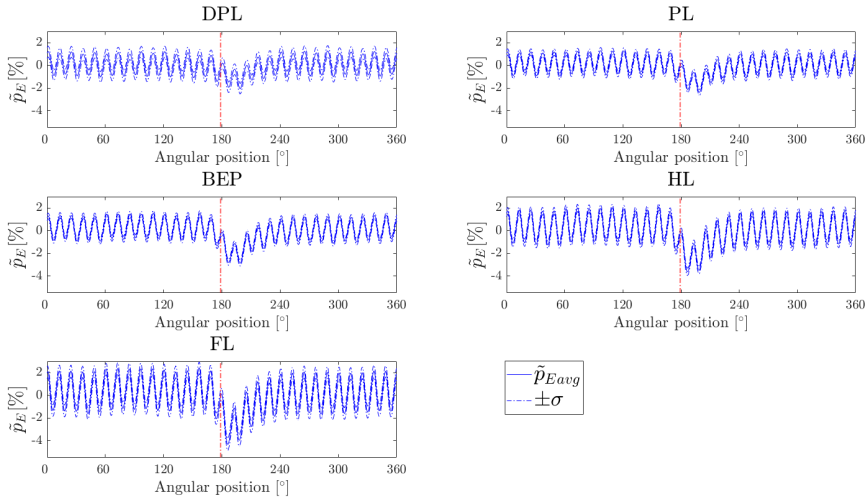

Figure A.8: Pressure variation with operating point, measured by PGV3 at stage 9, H=30m. The red dotted line indicates where the damaged blade (LE) passes the sensor.

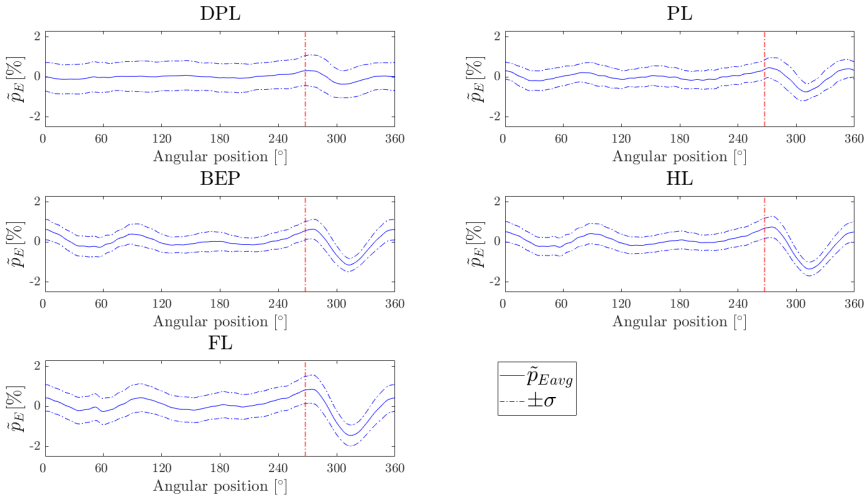

Figure A.9: Pressure variation with operating point, measured by PDT2 at stage 9, H=30m. The red dotted line indicates where the damaged blade (TE) passes the sensor.

A.1.3 Variation with head

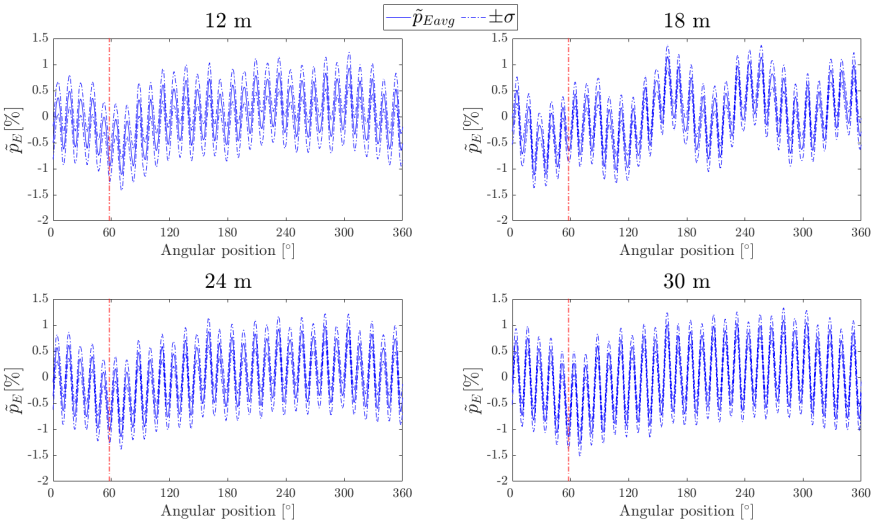

Figure A.10: Pressure variation with head, measured by PTC at stage 9, BEP. The red dotted line indicates where the damaged blade (LE) passes the sensor.

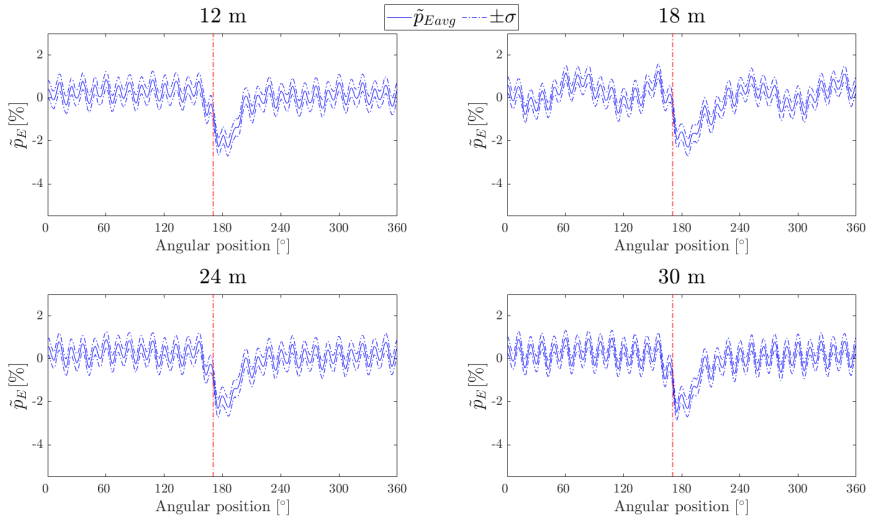

Figure A.11: Pressure variation with head, measured by PGV1 at stage 9, BEP. The red dotted line indicates where the damaged blade (LE) passes the sensor.

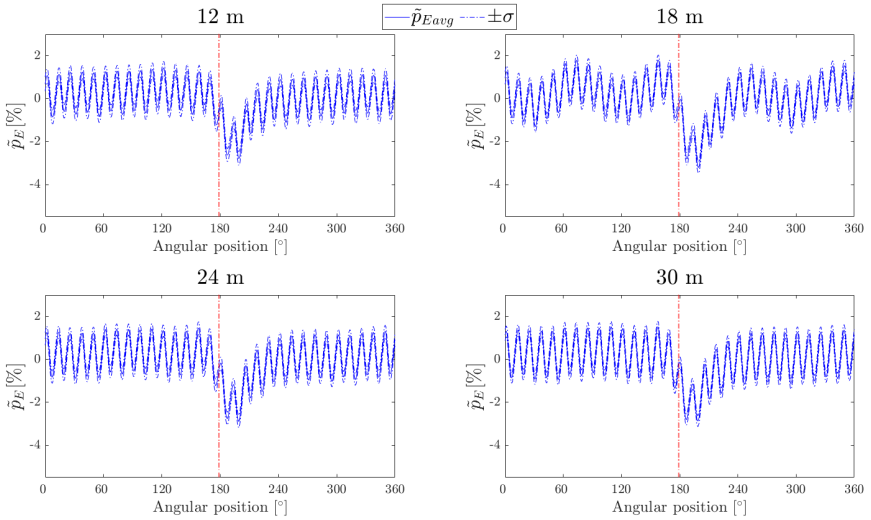

Figure A.12: Pressure variation with head, measured by PGV3 at stage 9, BEP. The red dotted line indicates where the damaged blade (LE) passes the sensor.

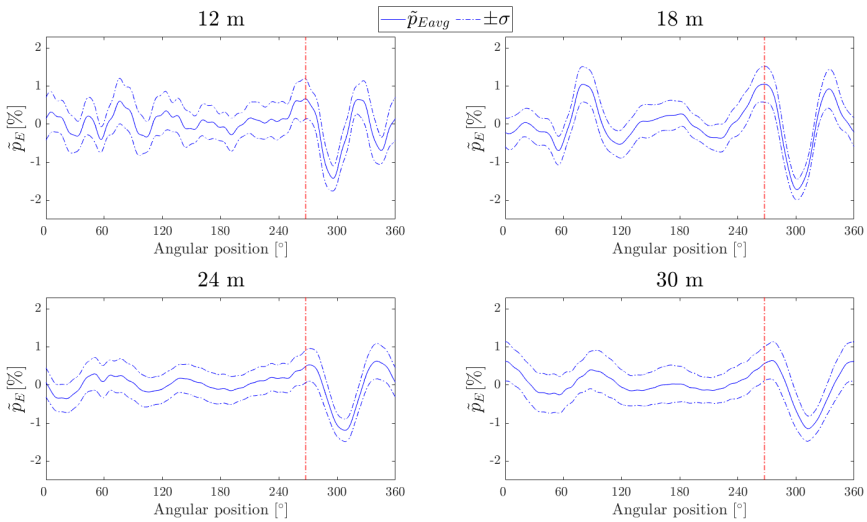

Figure A.13: Pressure variation with head, measured by PDT2 at stage 9, BEP. The red dotted line indicates where the damaged blade (TE) passes the sensor.

A.1.4 Frequency analysis

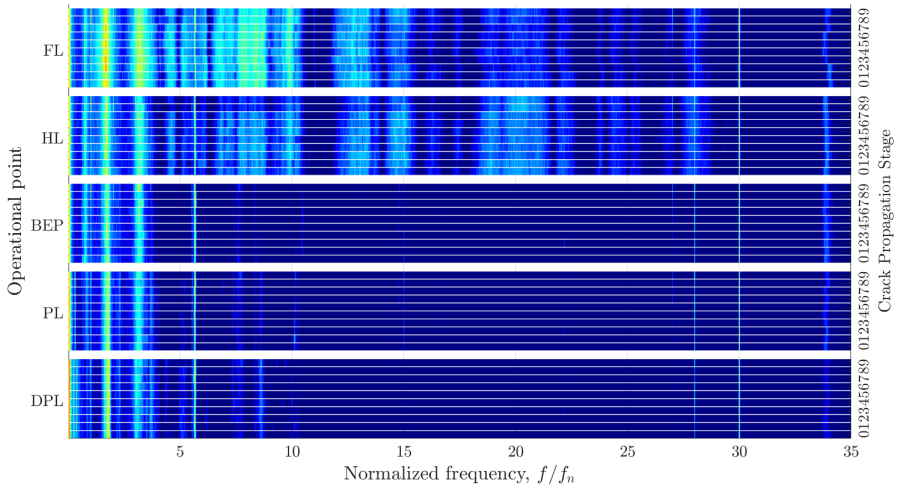

Figure A.14: Frequency analysis measured by PIN at H=30m. Data from all crack propagation stages (0-9) are structured together at a given operating point.

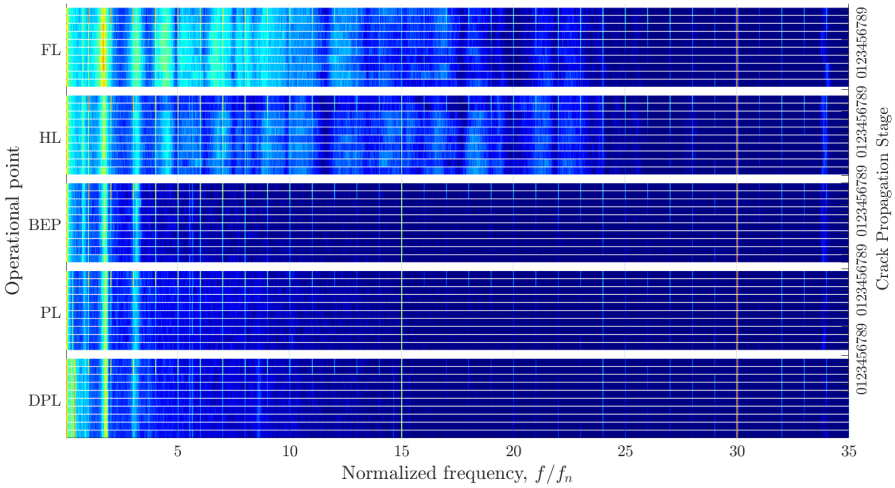

Figure A.15: Frequency analysis measured by PGV1 at H=30m. Data from all crack propagation stages (0-9) are structured together at a given operating point.

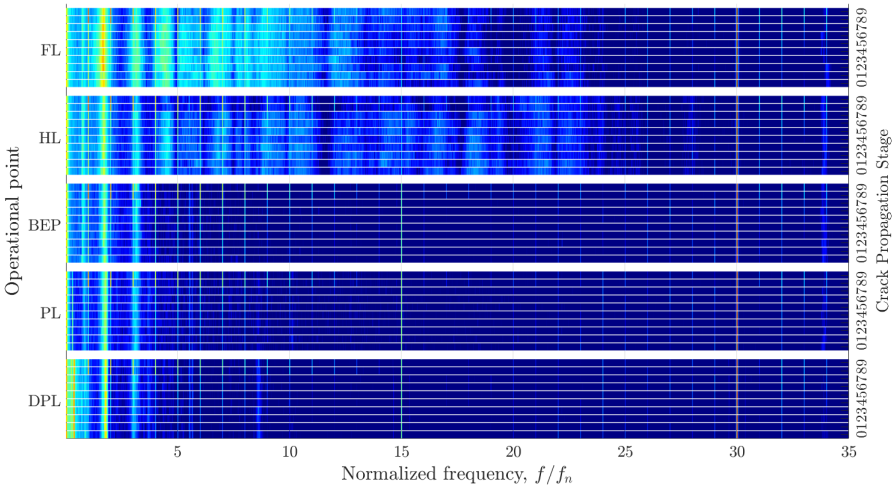

Figure A.16: Frequency analysis measured by PGV3 at H=30m. Data from all crack propagation stages (0-9) are structured together at a given operating point.

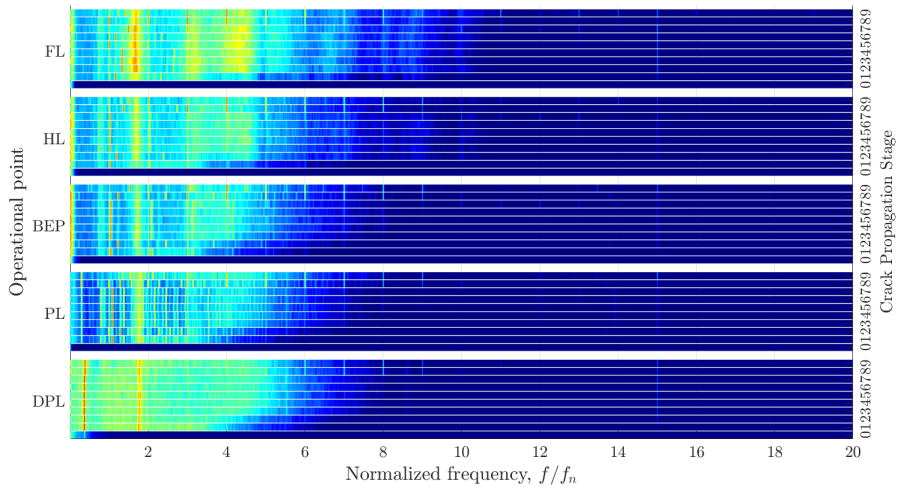

Figure A.17: Frequency analysis measured by PDT2 at H=30m. Data from all crack propagation stages (0-9) are structured together at a given operating point.

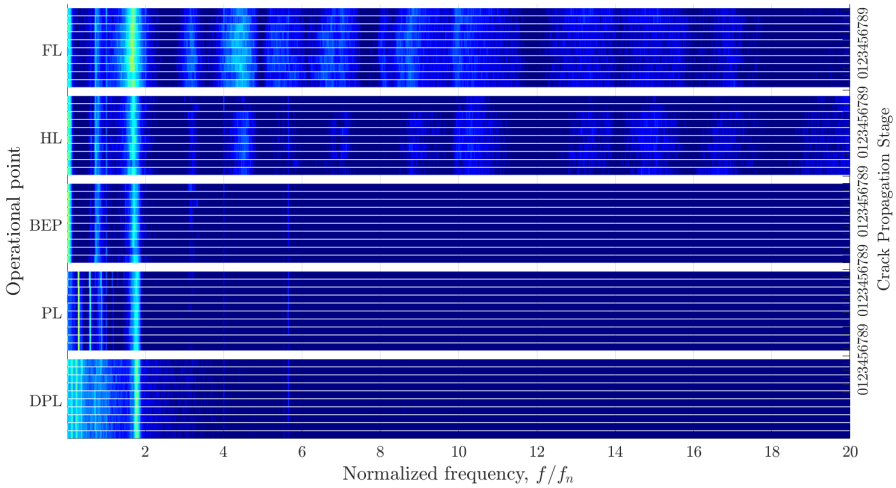

Figure A.18: Frequency analysis measured by PDT4 at H=30m. Data from all crack propagation stages (0-9) are structured together at a given operating point.

A.2 Vibration measurements

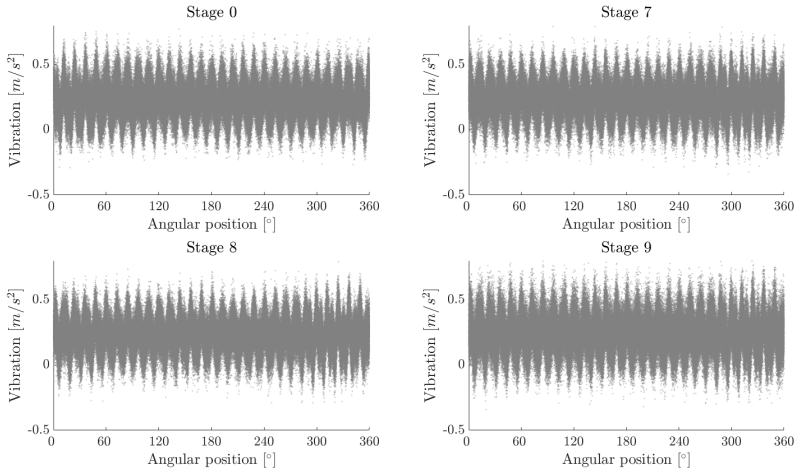

Figure A.19: Vibration measurements of AGV (guide vane shaft) at BEP and H=30m. 530 runner revolutions are overlaid and shown for stage 0, 7, 8 and 9.

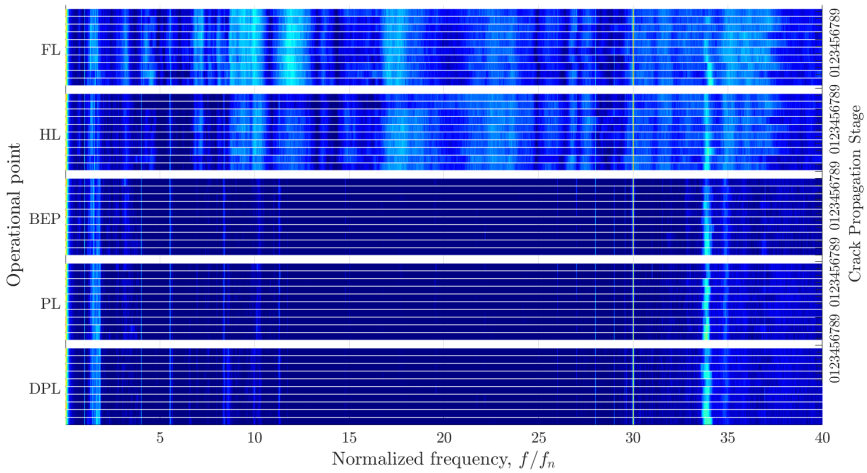

Figure A.20: Frequency analysis measured by AGV at BEP and H=30m. Data from all crack propagation stages (0-9) are structured together at a given operating point.

Appendix - B

Calculations

B.1 Rotational reference system

To indicate the position of the damaged runner blade in the pressure signals, the stationary sensors were related to the angular reference system of the damaged blade. The coordinates of the pressure sensors were collected from the HiFrancis project [1] and are listed in Table B.1. The z-coordinates are omitted as the sensors are related to an angular system.

Sensor	Description	X[mm]	Y [mm]	Uncertainty +/-[mm]
PTC	Upper turbine cover	-265.65	24.19	0.01
PGV1	Vaneless space	153.82	287.96	0.01
PGV2	Vaneless space	173.76	275.83	0.01
PGV3	Vaneless space	193.75	262.18	0.01
PDT1	Upper draft tube cone	- 161	-110	1
PDT2	Upper draft tube cone	110	161	1

Table B.1: Sensor coordinates [1]

Further on, the position of the trailing edge (TE) of the damaged blade, when the speed signal output -10V, was found. This corresponds to 0° in the angular reference system. Thus, by combining the radius of the runner outlet (R_2=173.5 mm) and the arc-length from (0,173.5) to 0°, the central angle θ was found. In this way, the sensor angles in the cartesian coordinate system could be calculated, and be related to the reference position of the damaged blade.

Figure B.1 shows the location of the pressure sensors in the angular reference system and Table B.2 lists the calculated angles from the sensors to the reference

position of the TE of the damaged blade. The sensors upstream of the runner were adjusted for the wrap angle, $\alpha_{wrap} = 70.18°$, which is the deflection from TE to LE of the blade.

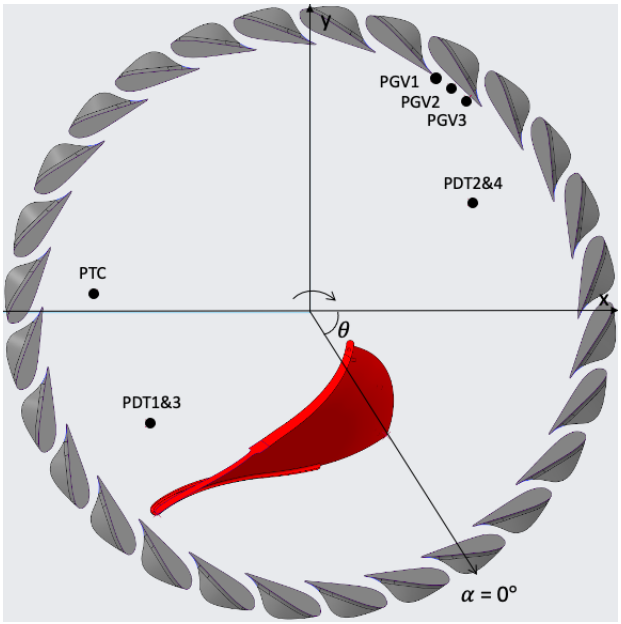

Figure B.1: Sensor location in the angular reference system

Description	$\alpha[°]$	Uncertainty +/-[°]
Damaged blade (TE)	0	0.05
Damaged blade (LE)	70.18	0.05
PTC	126.93	0.05
PGV1	239.83	0.05
PGV2	243.93	0.05
PGV3	248.18	0.05
PDT1/3	87.37	0.1
PDT2/4	267.37	0.1

Table B.2: Sensor angles from the reference position of the damaged blade (TE)

B.2 Calculation of the uncertainty of hydraulic efficiency

To evaluate how the efficiency trend varies during the crack growth and relate the variations to the uncertainty bound, the uncertainty of the hydraulic efficiency was estimated.

The relative systematic uncertainties from the operating sensors, f_{si}, were based on the calibration conducted by Langleite, spring 2020 [47]. The relative systematic uncertainties were then evaluated for the performed measurement in this study and the absolute systematic uncertainties, e_{si}, were found for each operating sensor.

The random errors were calculated from the conducted measurements of this study. The absolute uncertainties, e_{ri} and thus the relative uncertainties f_{ri}, were estimated based on the the student-t distribution from Equation 2.13 and 2.14, with a confidence interval of 95$\%$.

The main equations for calculating the relative uncertainty of the hydraulic efficiency are shown below, and details can be found in the matlab script attached in the electronic appendix.

The relative uncertainty of the hydraulic efficiency is given by

$$f_{\eta_h} = \sqrt{(f_Q)^2 + (f_E)^2 + (f_{\sum \tau})^2 + (f_n)^2 + (f_{\bar{\rho}})^2} \tag{B.1}$$

where Q denotes discharge, E denotes specific hydraulic energy, $\sum \tau$ denotes the sum of the friction and generator torque, n denotes rotational speed and ρ denotes the water density. Each component is a function of systematic and random uncertainty

$$f = \pm\sqrt{f_s^2 + f_r^2} \tag{B.2}$$

The relative uncertainty in the specific hydraulic energy is calculated as

$$f_E = \pm \frac{\sqrt{((\frac{\Delta P}{\bar{\rho}})f_{\Delta P})^2 + (v_1^2 f_{v_1})^2 + (v_2^2 f_{v_2})^2}}{\frac{\Delta P}{\bar{\rho}} + \frac{v_1^2 - v_2^2}{2}} \tag{B.3}$$

where the velocity uncertainty at turbine inlet and outlet are given by

$$f_{v_i} = \sqrt{f_Q^2 + 2(\frac{e_r}{r})^2} \tag{B.4}$$

The absolute and relative uncertainty in the torque measurements are calculated as

$$e_\tau = \pm \frac{\sqrt{e_{\tau_g}^2 + e_{\tau_f}^2}}{\tau_g + \tau_f} \tag{B.5}$$

$$f_\tau = \frac{e_\tau}{\tau} \tag{B.6}$$

The total relative and absolute uncertainty of the hydraulic efficiency at BEP and at stage 0 are estimated to be respectively

$$f_{\eta_h} = \pm 0.1183\% \tag{B.7}$$

$$e_{\eta_h} = \pm 0.0011 \tag{B.8}$$

Appendix - C

Equipment

C.1 Sensor documentation

MINIATURE HIGH PRESSURE PRESSURE TRANSDUCER

HKM-375 (M) SERIES

- Excellent Stability
- All Welded Construction
- Silicon on Silicon Integrated Sensor **VIS**®
- Robust Construction
- High Natural Frequencies
- 3/8-24 UNJF or M10 X 1 Thread
- Intrinsically Safe Applications Available (i.e. IS-HKM-375)

The HKM-375 is a miniature threaded pressure transducer. The hexagonal head and o-ring seal make it easy to mount and simple to apply.

The HKM-375 utilizes a flush metal diaphragm as a force collector. A solid state piezoresistive sensing element is located immediately behind this metal diaphragm which is protected by a metal screen. Force transfer is accomplished via non-compressible silicone oil. This sensing sub assembly is welded to a stainless steel body.

This advanced construction results in a highly stable, reliable and rugged instrument with all the advantages of significant miniaturization, excellent repeatability, low power consumption, etc. The miniaturization process also yields a marked increase in the natural frequencies of the transducers, making them suitable for use even in shock pressure measurements.

Kulite recommends the KSC Series of signal conditioners to maximize the measurement capability of the HKM-375 transducer.

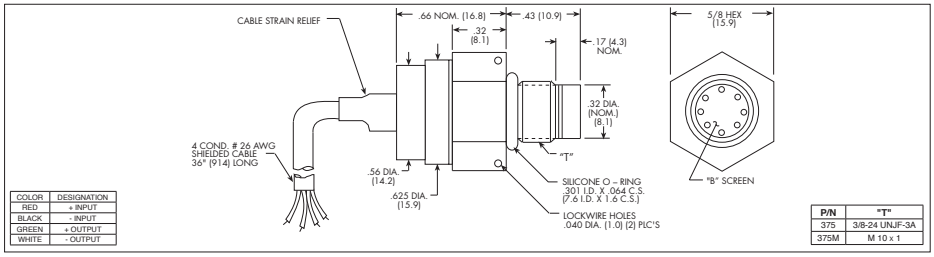

COLOR	DESIGNATION
RED	+ INPUT
BLACK	- INPUT
GREEN	+ OUTPUT
WHITE	- OUTPUT

P/N	"T"
375	3/8-24 UNJF-3A
375M	M 10 x 1

INPUT	Pressure Range	17 250	35 500	70 1000	170 2500	350 5000	700 10000	1400 BAR 20000 PSI
	Operational Mode	Absolute, Sealed Gage						
	Over Pressure	2 Times Rated Pressure to 1000 PSI (70 BAR) 1.5 Times Rated Pressure Above 1000 PSI to a Max. of 30000 PSI (2100 BAR)						
	Burst Pressure	3 Times Rated Pressure to a Max. of 35000 PSI (2400 BAR)						
	Pressure Media	Any Liquid or Gas Compatible With 15-5 PH or 316 Stainlesss Steel (All Media May Not Be Suitable With O-Ring Supplied)						
	Rated Electrical Excitation	10 VDC/AC						
	Maximum Electrical Excitation	12 VDC/AC						
	Input Impedance	1000 Ohms (Min.)						
OUTPUT	Output Impedance	1000 Ohms (Nom.)						
	Full Scale Output (FSO)	100mV (Nom.)						
	Residual Unbalance	± 5 mV (Typ.)						
	Combined Non-Linearity, Hysteresis and Repeatability	± 0.1% FSO BFSL (Typ.), ± 0.5% FSO (Max.)						
	Resolution	Infinitesimal						
	Natural Frequency of Sensor Without Screen (KHz) (Typ.)	Greater Than 400 KHz						
	Acceleration Sensitivity % FS/g Perpendicular	$2.2x10^{-4}$	$1.1x10^{-4}$	$6.2x10^{-5}$	$2.6x10^{-5}$	$1.5x10^{-5}$	$1.3x10^{-5}$	$8.0x10^{-6}$
	Insulation Resistance	100 Megohm Min. @ 50 VDC						
ENVIRONMENTAL	Operating Temperature Range	-65°F to +250°F (-55°C to +120°C)						
	Compensated Temperature Range	+80°F to +180°F (+25°C to +80°C) Any 100°F Range Within The Operating Range on Request						
	Thermal Zero Shift	± 1% FS/100° F (Typ.)						
	Thermal Sensitivity Shift	± 1% /100° F (Typ.)						
	Linear Vibration	10-2,000 Hz Sine, 100g. (Max.)						
	Mechanical Shock	20g half Sine Wave 11 msec. Duration						
PHYSICAL	Electrical Connection	4 Conductor 26 AWG Shielded Cable 36" Long						
	Weight	17 Grams (Max.) Excluding Cable						
	Pressure Sensing Principle	Fully Active Four Arm Wheatstone Bridge Dielectrically Isolated Silicon on Silicon						
	Mounting Torque	80 Inch-Pounds (Max.) 9 Nm						

Note: Custom pressure ranges, accuracies and mechanical configurations available. Dimensions are in inches. Dimensions in parenthesis are in millimeters. All dimensions nominal. (N)

Kulite miniature pressure transducers are intended for use in test and research and development programs and are not necessarily designed to be used in production applications. For products designed to be used in production programs, please consult the factory.

KULITE SEMICONDUCTOR PRODUCTS, INC. • One Willow Tree Road • Leonia, New Jersey 07605 • Tel: 201 461-0900 • Fax: 201 461-0990 • http://www.kulite.com

MINIATURE RUGGEDIZED HIGH TEMPERATURE IS® PRESSURE TRANSDUCER

XTE-190 (M) SERIES

- Easy Installation
- Silicon on Silicon Integrated Sensor **VIS®**
- High Natural Frequency
- High Temperature Up To 525°F

The ruggedness of this sensor has not compromised its performance. It was designed for ease of installation and will operate in temperatures up to 525°F (273°C). Its wide operating range (-65°F to +525°F) makes it ideal for numerous applications in Aerospace and other areas of industry.

OPTIONAL CONNECTOR VERSION

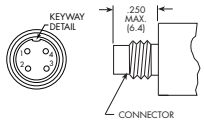

ORDER AS: XTE-100-190(M)

NOT AVAILABLE ON DIFFERENTIAL UNIT

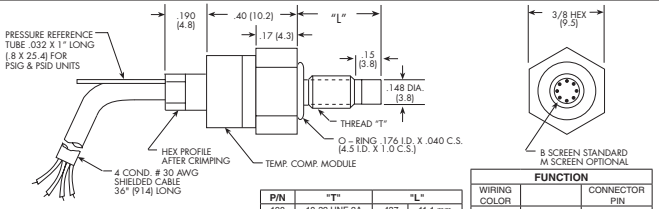

P/N	"T"		"L"
190	10-32 UNF-2A	.437	11.1 mm
190M	M5 x .8	.437	11.1 mm
190	10-32 UNF-2A	.760	19.3 mm
190M	M5 x .8	.760	19.3 mm

CONSULT FACTORY FOR SPECS. ON SEALED GAGE

FUNCTION		
WIRING COLOR		CONNECTOR PIN
RED	+ INPUT	1
WHITE	- OUTPUT	2
BLACK	- INPUT	3
GREEN	+ OUTPUT	4

INPUT Pressure Range	0.35 5	0.7 10	1.7 25	3.5 50	7 100	17 250	35 500	70 1000	140 BAR 2000 PSI
Operational Mode	Absolute, Gage, Sealed Gage, Differential					Absolute, Sealed Gage			
Over Pressure	2 Times Rated Pressure to a Maximum of 3000 PSI (210 BAR)								
Burst Pressure	3 Times Rated Pressure to a Maximum of 5000 PSI (350 BAR)								
Pressure Media	All Nonconductive, Noncorrosive Liquids or Gases								
Rated Electrical Excitation	10 VDC/AC								
Maximum Electrical Excitation	15 VDC/AC								
Input Impedance	1000 Ohms (Min.)								
OUTPUT Output Impedance	1000 Ohms (Nom.)								
Full Scale Output (FSO)	100 mV (Nom.)								
Residual Unbalance	± 5 mV (Typ.)								
Combined Non-Linearity, Hysteresis and Repeatability	± 0.1% FSO BFSL (Typ.), ± 0.5% FSO (Max.)								
Resolution	Infinitesimal								
Natural Frequency (KHz) (Typ.)	150	175	240	300	380	550	700	1000	1400
Acceleration Sensitivity % FS/g Perpendicular Transverse	$1.5x10^{-3}$ $2.2x10^{-4}$	$1.0x10^{-3}$ $1.4x10^{-4}$	$5.0x10^{-4}$ $6.0x10^{-5}$	$3.0x10^{-4}$ $4.0x10^{-5}$	$1.5x10^{-4}$ $2.0x10^{-5}$	$1.0x10^{-4}$ $9.0x10^{-6}$	$6.0x10^{-5}$ $6.0x10^{-6}$	$4.5x10^{-5}$ $3.0x10^{-6}$	$1.7x10^{-5}$ $1.8x10^{-6}$
Insulation Resistance	100 Megohm Min. @ 50 VDC								
ENVIRONMENTAL Operating Temperature Range	-65°F to +525°F (-55°C to +273°C)								
Compensated Temperature Range	+80°F to +450°F (+25°C to +232°C)								
Thermal Zero Shift	± 1% FS/100°F (Typ.)								
Thermal Sensitivity Shift	± 1% /100°F (Typ.)								
Steady Acceleration	10,000g. (Max.)								
Linear Vibration	10-2,000 Hz Sine, 100g. (Max.)								
PHYSICAL Electrical Connection	4 Conductor 30 AWG Shielded Cable 36" Long								
Weight	4 Grams (Nom.) Excluding Cable								
Pressure Sensing Principle	Fully Active Four Arm Wheatstone Bridge Dielectrically Isolated Silicon on Silicon								
Mounting Torque	15 Inch-Pounds (Max.) 1.7 N-m								

Note: Custom pressure ranges, accuracies and mechanical configurations available. Dimensions are in inches. Dimensions in parenthesis are in millimeters.
Continuous development and refinement of our products may result in specification changes without notice - all dimensions nominal. (H)

KULITE SEMICONDUCTOR PRODUCTS, INC. • One Willow Tree Road • Leonia, New Jersey 07605 • Tel: 201 461-0900 • Fax: 201 461-0990 • http://www.kulite.com

KISTLER

Quarz-Hochdrucksensor
Capteur de haute pression a quartz
Quartz High Pressure Sensor

701A

Quarz Drucksensor zum Messen dynamischer und quasistatischer Drücke bis 250 bar bei Temperaturen bis 200 °C.

Capteur de pression à quartz pour mesurer des pressions dynamiques et quasistatiques jusqu'à 250 bar à des températures jusqu'à 200 °C.

Quartz pressure sensor for measuring dynamic and quasistatic pressures up to 250 bar at temperatures up to 200 °C.

- hohe Empfindlichkeit
  haute sensibilité
  hight sensitivity
- Temperaturen bis zu 200 °C
  Températures jusqu'à 200 °C
  Temperatures up to 200 °C

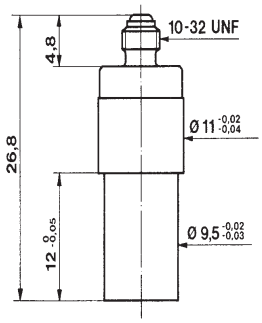

2:1

Technische Daten	Données techniques	Technical Data		
Bereich **Kalibrierte Teilbereiche**	**Gamme** **Gammes partielles étalonnées**	**Range** **Calibrated partial ranges**	bar bar bar	0 ... 250 0 ... 25 0 ... 2,5
Überlast	**Surcharge**	**Overload**	bar	400
Empfindlichkeit	**Sensibilité**	**Sensitivity**	pC/bar	≈ –80
Eigenfrequenz	**Fréquence propre**	**Natural frequency**	kHz	≈70
Linearität	**Linéarité**	**Linearity**	%FSO	≤ ±0,5
Beschleunigungsempfindlichkeit	**Sensibilité aux accélérations**	**Acceleration sensitivity**	bar/*g*	<0,001
Betriebstemperaturbereich	**Gamme de température d'utilisation**	**Operating temperature range**	°C	-150 ...200
Temperaturkoeffizient der Empfindlichkeit	**Coefficient de température de la sensibilité**	**Temperature coefficient of sensitivity**	$°C^{-1}$	$<10^{-4}$
Isolationswiderstand	**Résistance d'isolement**	**Insulation resistance**	Ω	$\geq 10^{13}$
Stossfestigkeit	**Résistance au choc**	**Shock resistance**	*g*	5000
Kapazität	**Capacité**	**Capacitance**	pF	9
Gewicht	**Poids**	**Weight**	g	8,5
Stecker, Teflon-Isolator	**Connecteur,** isolateur en téflon	**Connector,** teflon insulator		10-32 UNF

1 N (Newton) = 1 kg·m·s^{-2} = 0,1019... kp = 0,2248... lbf; 1 kp = 1 kgf = 9,80665 N; 1 inch = 25,4 mm; 1 kg = 2,2046... lb; 1 Nm = 0,73756... lbft

Beschreibung

Der zu messende Druck wirkt über die Membrane auf das Quarzkristall Messelement, das den Druck p (bar) in eine elektrische Ladung Q (pC = pico-Coulomb) umwandelt. Die Membrane aus rostfreiem Stahl ist mit dem Sensorgehäuse aus rostfreiem Stahl hermetisch und bündig verschweisst. Die Quarze sind in hochempfindlicher Anordnung (Transversaleffekt) in der Quarzkammer eingebaut, die mit dem Gehäuse hermetisch verschweisst ist.

Der Stecker-Anschluss ist mit dem Gehäuse verschweisst, jedoch ist sein Teflon-Isolator nicht dicht.

Description

Par l'intermédiaire du diaphragme, la pression agit sur l'élément de mesure à quartz qui transforme la pression p (bar) en charge électrique Q (pC = pico-Coulomb). Le diaphragme en acier inoxydable est soudé hermétiquement, au ras du front, au boîtier en acier inoxydable. Les éléments à quartz sont montés en un ensemble de haute sensibilité (effet transversal) dans la chambre à quartz, elle-même soudé hermétiquement au boîtier.

La prise électrique est soudée au boîtier, cependant son isolateur en téflon n'est pas rigoureusement étanche.

Description

The measured pressure acts through the diaphragm on the quartz crystal measuring element, which transforms the pressure p (bar) into an electrostatic charge Q (pC = pico-Coulomb). The stainless steel diaphragm is welded flush and hermetically to the stainless steel sensor body. The quartz elements are mounted in a highly sensitive arrangement (transversal effect) in the quartz chamber, which is welded hermetically to the body.

The connector is welded to the body, but its teflon insulator is not absolutely tight.

000-050m-06.95 (DB03.701Am-06.95)

Anwendung

Der Drucksensor 701A eignet sich besonders für die Messung schneller Druckverläufe. Bei besonders beschränkten Einbauverhältnissen oder sehr hohen Messfrequenzen ist der Drucksensor 601 zu verwenden.

Typische Anwendungen:
Druckmessungen an Verbrennungsmotoren, Kompressoren, pneumatischen und hydraulischen Anlagen (ausgenommen Einspritzpumpen).

Application

Le capteur 701A est adapté à la mesure de variations rapides de pression. On choisit le capteur miniature 601 pour des dispositifs à dimensions réduites ou pour les fréquences très élevées.

Exemples d'application:
Mesure de pressions de moteurs à combustion interne, compresseurs, installations pneumatiques et hydrauliques (à l'exception des pompes à injection).

Application

The quartz pressure sensor 701A is suited for dynamic pressure measurements. For very high frequencies or reduced mounting space the sensor 601 is used.

Typical applications:
Pressure measurements on combustion engines, compressors, pneumatic and hydraulic installations (except injection pumps).

Montage

Der Sensor kann mittels eines Montagenippels (Fig. 1) oder eines Steckernippels (Fig. 2) im Messobjekt oder dem Adapter montiert werden. Bei der Montage nach Fig. 2 werden Sensor und Steckernippel zu einer Montageeinheit zusammengeschraubt. Die Trennfläche kann mit "Loctite" gedichtet werden.

Siehe auch Datenblätter für:

Werkzeuge	4.012
Adapter	4.015
Steckernippel	4.014
Kabel	15.035

Montage

Le capteur peut être monté directement dans le dispositif de mesure ou dans l'adaptateur à l'aide d'un écrou de montage (fig. 1) ou d'un écrou connecteur (fig. 2). Pour le montage selon fig. 2, le capteur et l'écrou connecteur forment une unité. La jonction capteur - écrou connecteur peut être rendue étanche avec du "Loctite".

Voir aussi les notices techniques suivantes:

Outillage	4.012
Adaptateurs	4.015
Ecrous connecteurs	4.014
Câbles	15.035

Mounting

The sensor can be mounted directly into the measuring object or the adapter by means of a mounting nut (fig. 1) or a connecting nipple (fig. 2). When mounted with a connecting nipple, the latter is preassembled with the sensor to a mounting unit. The junction between nipple and sensor can be sealed with "Loctite".

See also datasheets for:

Tools	4.012
Adapters	4.015
Connecting nipples	4.014
Cables	15.035

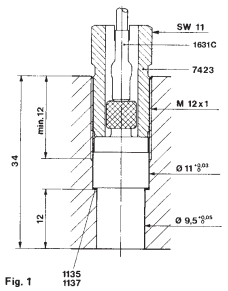

Fig. 1

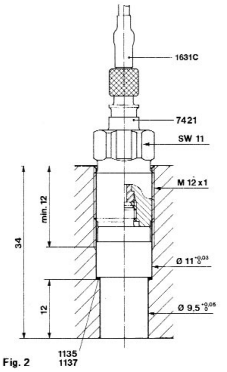

Fig. 2

Zubehör	*Typ*	Accessoires	*Type*	Accessories	*Type*
Cu-Dichtung	1135	Joint en cuivre	1135	Copper seal	1135
Ni-Dichtung	1135A	Joint en nickel	1135A	Nickel seal	1135A
Teflon-Dichtung	1137	Joint en téflon	1137	Teflon seal	1137
Schlüssel für Steckernippel 7421	1303	Clé pour écrou connecteur 7421	1303	Key for connecting nipple 7421	1303
Stufenbohrer	1333	Aléseuse progressive	1333	Step drill	1333
Ausziehwerkzeug für 10-32 UNF	1311	Outil extracteur pour 10-32 UNF	1311	Extraction tool 10-32 UNF	1311
Montagenippel SW8	7423	Ecrou de montage OCW8	7423	Mounting nut WS8	7423
Steckernippel 10-32UNF/10-32UNF	7421	Ecrou connecteur 10-32UNF/10-32UNF	7421	Connecting nipple 10-32UNF/10-32UNF	7421
Steckernippel 10-32UNF/BNC	7401	Ecrou connecteur 10-32UNF/BNC	7401	Connecting nipple 10-32UNF/BNC	7401
Steckernippel 10-32UNF/TNC	7411	Ecrou connecteur 10-32UNF/TNC	7411	Connecting nipple 10-32UNF/TNC	7411
Steckernippel luftgekühlt 10-32UNF/10-32UNF	7461	Ecrou connecteur refroidi par air 10-32UNF/10-32UNF	7461	Connecting nipple air cooled 10-32UNF/10-32UNF	7461
Schrumpfschlauch für Stecker	1021	Gaine thermorétractable pour connecteur	1021	Heat-shrink tubing for connector	1021
Montageadapter M14 x 1,25	7501	Adaptateur de montage M14 x 1,25	7501	Mounting adapter M14 x 1,25	7501
Montageadapter M5	7503	Adaptateur de montage M5	7503	Mounting adapter M5	7503
Kühladapter M18 x 1,5	7505	Adaptateur refroidi M18 x 1,5	7505	Cooling adapter M18 x 1,5	7505
Kühladapter M14 x 1,25	7507	Adaptateur refroidi M14 x 1,25	7507	Cooling adapter M14 x 1,25	7507

000-050m-06.95 (D803.701Am-06.95)

Calibration Chart for DeltaTron® Accelerometer Type 4397

Brüel & Kjær

Serial No.: 33995

Reference Sensitivity [1] at 159.2 Hz (ω = 1000 s^{-1}), 20 ms^{-2} RMS, 4 mA supply current and 24.1 °C: 0.9947 mV/ms^{-2} (9.754 mV/g)

Frequency Range:

Amplitude (±10%):	1 Hz to 25 kHz
Phase (± 5°):	4 Hz to 2.2 kHz

Mounted Resonance Frequency: 53 kHz

Transverse Sensitivity [2]:
Maximum (at 30 Hz, 100 ms^{-2}): 1.2 % re Reference Sensitivity
Angle of minimum, α: (see drawing) 171 °

Transverse Resonance Frequency: 17 kHz

Calculated values for TEDS [3]:

Resonance frequency:	52.0 kHz
Quality factor @ f_{res}:	102
Amplitude slope:	-2.3 %/decade
High pass cut-off frequency:	0.11 Hz
Low pass cut-off frequency:	39 kHz

Measuring Range:

T < 100°C:	± 7500 ms^{-2} peak (± 750 g peak)
T < 125°C:	± 5000 ms^{-2} peak (± 500 g peak)

Polarity of the electrical signal is positive for an acceleration in the direction of the arrow on the drawing.

Electrical:

Bias Voltage:	at 25°C and 4 mA:	+ 12 V ± 0.5 V
	at full temperature and current range:	+ 8 V to + 15 V
Power Supply requirements:	Constant Current: T < 100°C:	+ 2 to + 20 mA
	T < 125°C:	+ 2 to + 10 mA
	Unloaded Supply Voltage:	+ 24 V to + 30 V
Output Impedance:		10 Ω
Start-up time (to final bias ± 10%):		5 s
Inherent Noise (RMS):		< 15 µV
Broadband (1 Hz to 22 kHz):	corresponding to < 0.015 ms^{-2}	(< 1500 µg)
Spectral: 10 Hz:	7.9x10^{-4} ms^{-2}/√Hz	(79 µg/√Hz)
100 Hz:	2.1x10^{-4} ms^{-2}/√Hz	(21 µg/√Hz)
1000 Hz:	1.4x10^{-4} ms^{-2}/√Hz	(14 µg/√Hz)

Ground Loops can introduce error signals. These can be avoided by insulating the accelerometer from the mounting surface using Insulating Stud UA 1216.

Recommended cable: AO 1381

Environmental:

Temperature Range:	- 50 to + 125°C (- 58 to + 257°F)
Temperature Coefficient of Sensitivity:	+ 0.05%/°C
Temp. Transient Sensitivity (3 Hz Low. Lim. Frq. (-3 dB, 6 dB/oct)):	2 ms^{-2}/°C
Magnetic Sensitivity (50 Hz, 0.038 T):	50 ms^{-2}/T
Acoustic Sensitivity (154 dB SPL):	0.01 ms^{-2}
Base Strain Sensitivity (at 250 µε in base plane):	0.005 ms^{-2}/µε
Max. Non-destructive Shock: Axial:	100 kms^{-2} peak (10000 g peak)
Transverse:	50 kms^{-2} peak (5000 g peak)
Humidity:	90 % RH non-condensing

Mechanical:

Case Material:	Titanium ASTM Grade 2
Sensing Element:	Piezoelectric, Type PZ 23
Construction:	Delta Shear®
Sealing:	Welded
Weight:	2.4 gram (0.085 oz)
Electrical Connector:	Coaxial M3
Mounting Thread:	M3, Depth 2.4 mm
Mounting Surface Flatness:	< 3 µm
Mounting Torque:	Max. 0.6 Nm (5.3 lbf-in). Min. 0.2 Nm (1.8 lbf-in)

[1] This calibration is obtained on a modified Brüel & Kjær Calibration System Type 9610 System No.: 2501275 and is traceable (amplitude only) to the National Institute of Standards and Technology, USA and Physikalisch-Technische Bundesanstalt, Germany.
The expanded uncertainty 5 Hz to 4 kHz: 1.0%, 4 kHz to 7 kHz: 1.4% and 7 kHz to 10 kHz: 2.0% is determined in accordance with EAL-R2. A coverage factor k=2 is used. This corresponds to a coverage probability of 95% for a normal distribution.

[2] The uncertainty is 0.3% of Reference Sensitivity and 5° on the angle.

[3] Transducer Electronic Data Sheet according to IEEE P1451.4. Built-in ID-information not included.

[4] Deviation from Reference Sensitivity.

For further information, please see http://www.bksv.com and Product Data Sheet BP 1288 and BP 1849.

Mounting Technique:
Examine the mounting surface for cleanliness and smoothness.
If necessary, machine surface to a flatness < 10 µm and a roughness < 2 µm.
Fasten the accelerometer using the appropriate stud. Take care not to exceed the recommended mounting torque and that the stud does not bottom in the mounting hole.
A thin film of oil or grease between the accelerometer and the mounting surface helps achieve good contact and improves mounting stiffness.
See also ISO 5348. For other types of mounting, see the Brüel & Kjær handbook "Piezoelectric Accelerometers and Vibration Preamplifiers" (available from your local Brüel & Kjær representative).

Individual Frequency Response [1]

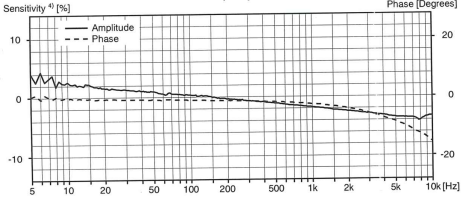

Typical Low Frequency Response

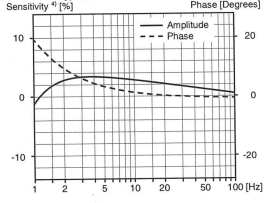

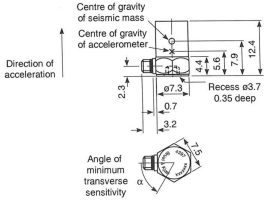

Date 02 apr 2020, 13:47 Operator LP

Specifications obtained in accordance with ANSI S2.11-1969 and parts of ISO 5347.

All values are typical at 25°C (77°F) unless measurement uncertainty is specified.

BC 0325-13

Serial No.: 33995

C.2 Calibration reports

CALIBRATION REPORT

CALIBRATION PROPERTIES
Calibrated by: Gine Kirkebøen Støren
Type/Producer: Kulite HKM-375MCO
SN: 8344-6-20
Range: 0-7 bar g
Unit: kPa
test
Druck PTX 1830
2867610
0-10 bar a
kPa

CALIBRATION SOURCE PROPERTIES
Type/Producer: Pressurements deadweight tester P3223-1
SN: 66256
Uncertainty [%]: 0.008

POLY FIT EQUATION:
Y= -13.87995589E+0X^0 + 86.35505636E+3X^1

CALIBRATION SUMARY:
Max Uncertainty : 9.969301 [%]
Max Uncertainty : 0.043353 [kPa]
RSQ : 1.000000
Calibration points : 28

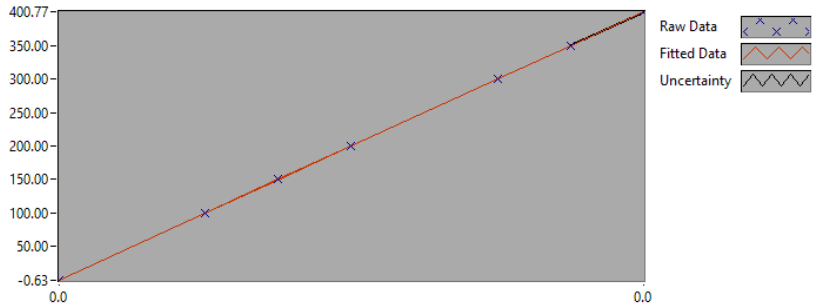

Figure 1 : Calibration chart (The uncertainty band is multiplied by 10)

Gine Kirkebøen Støren

CALIBRATION VALUES

Value [kPa]	Voltage [V]	Best Poly Fit [kPa]	Deviation [kPa]	Uncertainty [%]	Uncertainty [kPa]
-0.317777	0.000158	-0.263251	-0.054526	9.966404	-0.031671
99.833293	0.001317	99.884212	-0.050918	0.025499	0.025456
149.908829	0.001897	149.916693	-0.007864	0.014988	0.022469
199.984364	0.002476	199.967109	0.017255	0.011780	0.023557
300.135435	0.003636	300.139994	-0.004559	0.010618	0.031869
350.210971	0.004217	350.241309	-0.030339	0.010621	0.037195
400.286506	0.004797	400.340841	-0.054335	0.010804	0.043249
400.286506	0.004797	400.340742	-0.054235	0.010804	0.043247
350.210971	0.004217	350.242095	-0.031124	0.010587	0.037075
300.135435	0.003636	300.130520	0.004916	0.010594	0.031796
199.984364	0.002477	199.981442	0.002923	0.011778	0.023555
149.908829	0.001896	149.878197	0.030632	0.014835	0.022239
99.833293	0.001317	99.840778	-0.007485	0.023665	0.023625
-0.317777	0.000157	-0.313532	-0.004245	9.969301	-0.031680
-0.317777	0.000157	-0.313580	-0.004197	9.969301	-0.031680
99.833293	0.001317	99.831235	0.002059	0.023553	0.023514
149.908829	0.001896	149.857078	0.051751	0.014854	0.022268
199.984364	0.002476	199.916638	0.067726	0.011836	0.023670
300.135435	0.003636	300.101834	0.033602	0.011118	0.033370
350.210971	0.004216	350.178864	0.032106	0.010658	0.037325
400.286506	0.004796	400.288748	-0.002241	0.010820	0.043313
400.286506	0.004796	400.288772	-0.002266	0.010831	0.043353
350.210971	0.004216	350.206016	0.004955	0.010626	0.037214
300.135435	0.003636	300.097813	0.037622	0.010572	0.031732
199.984364	0.002476	199.942034	0.042331	0.011834	0.023666
149.908829	0.001896	149.880283	0.028546	0.014785	0.022164
99.833293	0.001317	99.868747	-0.035454	0.023500	0.023461
-0.317777	0.000157	-0.305143	-0.012635	9.969301	-0.031680

COMMENTS:

The uncertainty is calculated with 95% confidence. The uncertainty includes the randomness in the calibrated instrument during the calibration, systematic uncertainty in the instrument or property which the instrument under calibration is compared with (dead weight manometer, calibrated weights etc.), and due to regression analysis to fit the calibration points to a linear calibration equation.The calculated uncertainty can be used as the total systematic uncertianty of the calibrated instrument with the given calibration equation.

CALIBRATION REPORT

CALIBRATION PROPERTIES
Calibrated by: Gine Kirkebøen Støren
Type/Producer: Kulite HKM-375MCO
SN: 8344-6-21
Range: 0-7 bar g
Unit: kPa
test
Druck PTX 1830
2867610
0-10 bar a
kPa

CALIBRATION SOURCE PROPERTIES
Type/Producer: Pressurements deadweight tester P3223-1
SN: 66256
Uncertainty [%]: 0.008

POLY FIT EQUATION:
Y= -9.10634490E+0X^0 + 87.17219869E+3X^1

CALIBRATION SUMARY:
Max Uncertainty : 12.477934 [%]
Max Uncertainty : 0.049044 [kPa]
RSQ : 1.000000
Calibration points : 28

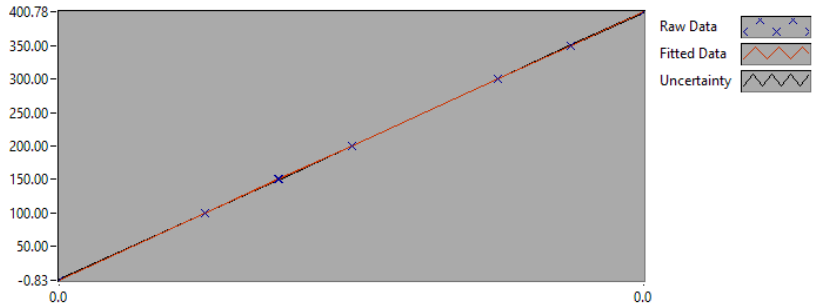

Figure 1 : Calibration chart (The uncertainty band is multiplied by 10)

Gine Kirkebøen Støren

CALIBRATION VALUES

Value [kPa]	Voltage [V]	Best Poly Fit [kPa]	Deviation [kPa]	Uncertainty [%]	Uncertainty [kPa]
-0.317777	0.000101	-0.340139	0.022361	12.474276	-0.039640
99.833293	0.001251	99.910632	-0.077339	0.029645	0.029596
149.908829	0.001825	149.961656	-0.052827	0.019137	0.028688
199.984364	0.002399	200.021363	-0.036999	0.013526	0.027050
300.135435	0.003548	300.141670	-0.006234	0.012222	0.036682
350.210971	0.004122	350.219406	-0.008435	0.011862	0.041541
400.286506	0.004696	400.292671	-0.006164	0.012252	0.049044
400.286506	0.004696	400.292159	-0.005653	0.012244	0.049012
350.210971	0.004122	350.196969	0.014001	0.011838	0.041458
300.135435	0.003547	300.111288	0.024147	0.011904	0.035728
199.984364	0.002399	199.995082	-0.010718	0.014315	0.028628
149.908829	0.001825	149.948205	-0.039376	0.018026	0.027022
99.833293	0.001251	99.923348	-0.090054	0.029636	0.029587
-0.317777	0.000100	-0.388391	0.070613	12.477934	-0.039652
-0.317777	0.000100	-0.388462	0.070684	12.477934	-0.039652
99.833293	0.001251	99.936349	-0.103056	0.029377	0.029328
149.908829	0.001824	149.928085	-0.019256	0.018093	0.027123
199.984364	0.002398	199.965538	0.018827	0.013706	0.027409
300.135435	0.003547	300.102417	0.033019	0.011679	0.035053
350.210971	0.004122	350.186903	0.024068	0.011832	0.041437
400.286506	0.004696	400.278397	0.008109	0.012172	0.048723
400.286506	0.004696	400.278746	0.007760	0.012170	0.048716
350.210971	0.004122	350.193310	0.017661	0.011991	0.041993
300.135435	0.003547	300.076598	0.058838	0.011621	0.034879
199.984364	0.002398	199.968760	0.015604	0.013552	0.027103
149.908829	0.001824	149.915636	-0.006808	0.017791	0.026670
99.833293	0.001250	99.869298	-0.036005	0.029372	0.029323
-0.317777	0.000100	-0.431007	0.113230	12.477933	-0.039652

COMMENTS:

The uncertainty is calculated with 95% confidence. The uncertainty includes the randomness in the calibrated instrument during the calibration, systematic uncertainty in the instrument or property which the instrument under calibration is compared with (dead weight manometer, calibrated weights etc.), and due to regression analysis to fit the calibration points to a linear calibration equation.The calculated uncertainty can be used as the total systematic uncertianty of the calibrated instrument with the given calibration equation.

CALIBRATION REPORT

CALIBRATION PROPERTIES
Calibrated by: Gine Kirkebøen Støren
Type/Producer: Kulite XTE-190 SM
SN: 8317-1-201
Range: 0-3.5 bar a
Unit: kPa

CALIBRATION SOURCE PROPERTIES
Type/Producer: Pressurements deadweight tester P3223-1
SN: 66256
Uncertainty [%]: 0.008

POLY FIT EQUATION:
Y= -442.56191628E+0X^0 + 36.20285756E+3X^1

CALIBRATION SUMARY:
Max Uncertainty : 0.272435 [%]
Max Uncertainty : 0.270262 [kPa]
RSQ : 0.999990
Calibration points : 28

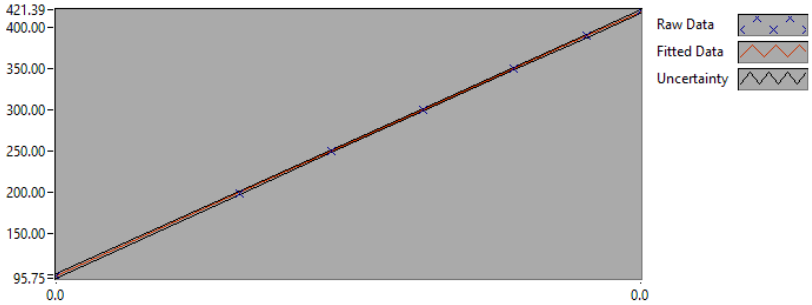

Figure 1 : Calibration chart (The uncertainty band is multiplied by 10)

Gine Kirkebøen Støren

CALIBRATION VALUES

Value [kPa]	Voltage [V]	Best Poly Fit [kPa]	Deviation [kPa]	Uncertainty [%]	Uncertainty [kPa]
99.202200	0.014951	98.690817	0.511383	0.272435	0.270262
199.353271	0.017737	199.562994	-0.209724	0.086116	0.171675
249.428806	0.019123	249.734531	-0.305725	0.056419	0.140725
299.504342	0.020506	299.802287	-0.297946	0.044928	0.134562
349.579877	0.021884	349.702403	-0.122525	0.044611	0.155951
389.640305	0.022983	389.491954	0.148351	0.047964	0.186888
419.685627	0.023804	419.226194	0.459433	0.051171	0.214756
419.685627	0.023804	419.225441	0.460185	0.051171	0.214756
389.640305	0.022983	389.480241	0.160064	0.047964	0.186886
349.579877	0.021885	349.735177	-0.155300	0.044615	0.155963
299.504342	0.020507	299.853325	-0.348983	0.044930	0.134568
249.428806	0.019125	249.802706	-0.373899	0.056406	0.140694
199.353271	0.017738	199.603809	-0.250538	0.086101	0.171646
99.202200	0.014951	98.706423	0.495777	0.272435	0.270262
99.202200	0.014951	98.706342	0.495858	0.272435	0.270262
199.353271	0.017738	199.615858	-0.262587	0.086101	0.171646
249.428806	0.019125	249.800397	-0.371591	0.056407	0.140694
299.504342	0.020507	299.840966	-0.336624	0.044931	0.134569
349.579877	0.021885	349.733509	-0.153632	0.044615	0.155966
389.640305	0.022983	389.500708	0.139598	0.047962	0.186878
419.685627	0.023805	419.243532	0.442095	0.051180	0.214795
419.685627	0.023805	419.243451	0.442176	0.051180	0.214795
389.640305	0.022984	389.531611	0.108694	0.047970	0.186910
349.579877	0.021886	349.768272	-0.188395	0.044621	0.155986
299.504342	0.020508	299.874466	-0.370124	0.044932	0.134573
249.428806	0.019125	249.803215	-0.374409	0.056408	0.140698
199.353271	0.017738	199.590012	-0.236742	0.086101	0.171646
99.202200	0.014951	98.707070	0.495130	0.272435	0.270262

COMMENTS:

The uncertainty is calculated with 95% confidence. The uncertainty includes the randomness in the calibrated instrument during the calibration, systematic uncertainty in the instrument or property which the instrument under calibration is compared with (dead weight manometer, calibrated weights etc.), and due to regression analysis to fit the calibration points to a linear calibration equation.The calculated uncertainty can be used as the total systematic uncertianty of the calibrated instrument with the given calibration equation.

CALIBRATION REPORT

CALIBRATION PROPERTIES
Calibrated by: Gine Kirkebøen Støren
Type/Producer: Kulite XTL-190
SN: 8317-1-202
Range: 0-3.5 bar a
Unit: kPa

CALIBRATION SOURCE PROPERTIES
Type/Producer: Pressurements deadweight tester P3223-1
SN: 66256
Uncertainty [%]: 0.008

POLY FIT EQUATION:
Y= + 7.37240266E+0X^0 + 34.65479510E+3X^1

CALIBRATION SUMARY:
Max Uncertainty : 0.293255 [%]
Max Uncertainty : 0.290535 [kPa]
RSQ : 0.999987
Calibration points : 28

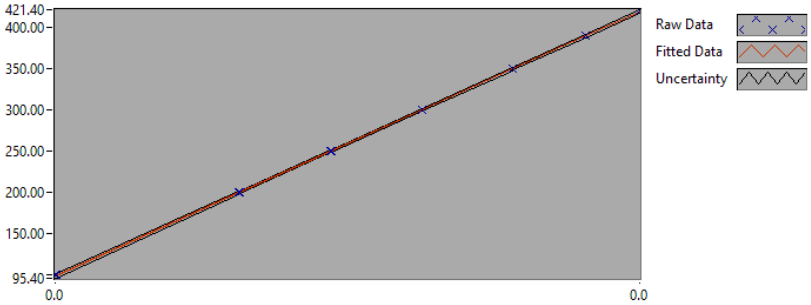

Figure 1 : Calibration chart (The uncertainty band is multiplied by 10)

Gine Kirkebøen Støren

CALIBRATION VALUES

Value [kPa]	Voltage [V]	Best Poly Fit [kPa]	Deviation [kPa]	Uncertainty [%]	Uncertainty [kPa]
99.072200	0.002624	98.301819	0.770381	0.293255	0.290535
199.223271	0.005537	199.273236	-0.049965	0.092567	0.184415
249.298806	0.006987	249.502520	-0.203714	0.060562	0.150981
299.374342	0.008431	299.556158	-0.181816	0.048167	0.144200
349.449877	0.009870	349.404826	0.045051	0.047795	0.167021
389.510305	0.011019	389.226596	0.283710	0.051411	0.200252
419.555627	0.011880	419.071222	0.484405	0.054896	0.230321
419.555627	0.011880	419.071244	0.484383	0.054896	0.230318
389.510305	0.011025	389.441651	0.068655	0.051451	0.200409
349.449877	0.009878	349.696924	-0.247047	0.047846	0.167198
299.374342	0.008439	299.831137	-0.456796	0.048178	0.144233
249.298806	0.006994	249.749228	-0.450421	0.060518	0.150871
199.223271	0.005545	199.533728	-0.310457	0.092448	0.184179
99.072200	0.002633	98.613674	0.458526	0.292885	0.290168
99.072200	0.002633	98.613332	0.458868	0.292885	0.290168
199.223271	0.005545	199.519705	-0.296435	0.092447	0.184175
249.298806	0.006992	249.689088	-0.390282	0.060530	0.150900
299.374342	0.008437	299.740224	-0.365882	0.048177	0.144229
349.449877	0.009875	349.590120	-0.140243	0.047826	0.167127
389.510305	0.011023	389.369784	0.140521	0.051448	0.200395
419.555627	0.011881	419.093483	0.462144	0.054895	0.230313
419.555627	0.011881	419.093576	0.462051	0.054894	0.230313
389.510305	0.011025	389.431207	0.079098	0.051502	0.200607
349.449877	0.009878	349.694142	-0.244265	0.047850	0.167210
299.374342	0.008439	299.839491	-0.465149	0.048181	0.144241
249.298806	0.006994	249.764604	-0.465798	0.060520	0.150875
199.223271	0.005546	199.573344	-0.350073	0.092432	0.184146
99.072200	0.002634	98.651649	0.420550	0.292844	0.290127

COMMENTS:

The uncertainty is calculated with 95% confidence. The uncertainty includes the randomness in the calibrated instrument during the calibration, systematic uncertainty in the instrument or property which the instrument under calibration is compared with (dead weight manometer, calibrated weights etc.), and due to regression analysis to fit the calibration points to a linear calibration equation.The calculated uncertainty can be used as the total systematic uncertianty of the calibrated instrument with the given calibration equation.

CALIBRATION REPORT

CALIBRATION PROPERTIES
Calibrated by: Gine Kirkebøen Støren
Type/Producer: Kulite XTE-190 SM
SN: 8317-1-204
Range: 0-3.5 bar a
Unit: kPa

CALIBRATION SOURCE PROPERTIES
Type/Producer: Pressurements deadweight tester P3223-1
SN: 66256
Uncertainty [%]: 0.008

POLY FIT EQUATION:
Y= -3.55575536E+0X^0 + 34.83526007E+3X^1

CALIBRATION SUMARY:
Max Uncertainty : 0.279475 [%]
Max Uncertainty : 0.277888 [kPa]
RSQ : 0.999989
Calibration points : 28

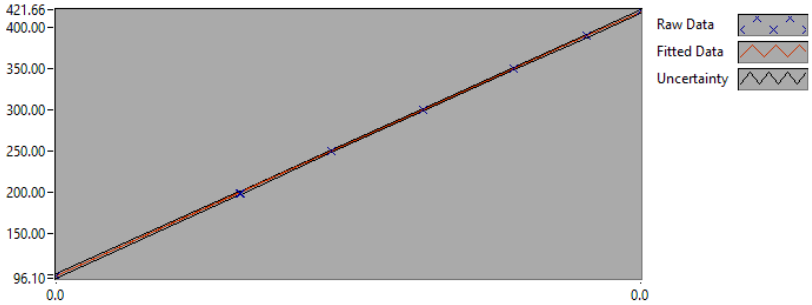

Figure 1 : Calibration chart (The uncertainty band is multiplied by 10)

Gine Kirkebøen Støren

CALIBRATION VALUES

Value [kPa]	Voltage [V]	Best Poly Fit [kPa]	Deviation [kPa]	Uncertainty [%]	Uncertainty [kPa]
99.432200	0.002941	98.878213	0.553986	0.279475	0.277888
199.583271	0.005837	199.794554	-0.211283	0.088420	0.176471
249.658806	0.007278	249.987180	-0.328374	0.057920	0.144603
299.734342	0.008715	300.048550	-0.314208	0.046118	0.138232
349.809877	0.010147	349.932463	-0.122586	0.045791	0.160180
389.870305	0.011289	389.696497	0.173808	0.049243	0.191983
419.915627	0.012143	419.437082	0.478545	0.052554	0.220684
419.915627	0.012143	419.436983	0.478643	0.052554	0.220683
389.870305	0.011290	389.727313	0.142993	0.049253	0.192023
349.809877	0.010149	349.993182	-0.183305	0.045805	0.160229
299.734342	0.008718	300.128945	-0.394603	0.046127	0.138258
249.658806	0.007281	250.069091	-0.410285	0.057902	0.144558
199.583271	0.005839	199.847857	-0.264587	0.088391	0.176414
99.432200	0.002942	98.918926	0.513274	0.279436	0.277849
99.432200	0.002942	98.918641	0.513558	0.279436	0.277849
199.583271	0.005837	199.794139	-0.210868	0.088421	0.176473
249.658806	0.007279	250.000798	-0.341992	0.057914	0.144589
299.734342	0.008716	300.071612	-0.337270	0.046121	0.138240
349.809877	0.010148	349.956574	-0.146697	0.045800	0.160214
389.870305	0.011289	389.711388	0.158918	0.049270	0.192087
419.915627	0.012143	419.453613	0.462014	0.052576	0.220774
419.915627	0.012143	419.453680	0.461947	0.052575	0.220772
389.870305	0.011290	389.748154	0.122152	0.049264	0.192067
349.809877	0.010150	350.009547	-0.199670	0.045812	0.160255
299.734342	0.008717	300.114521	-0.380179	0.046122	0.138242
249.658806	0.007281	250.066015	-0.407209	0.057904	0.144561
199.583271	0.005841	199.900023	-0.316752	0.088363	0.176357
99.432200	0.002942	98.922170	0.510029	0.279435	0.277849

COMMENTS:

The uncertainty is calculated with 95% confidence. The uncertainty includes the randomness in the calibrated instrument during the calibration, systematic uncertainty in the instrument or property which the instrument under calibration is compared with (dead weight manometer, calibrated weights etc.), and due to regression analysis to fit the calibration points to a linear calibration equation.The calculated uncertainty can be used as the total systematic uncertianty of the calibrated instrument with the given calibration equation.

CALIBRATION REPORT

CALIBRATION PROPERTIES
Calibrated by: Gine Kirkebøen Støren
Type/Producer: Kulite HEM-375
SN: 6293-6A-408
Range: 0-1,7 bar a
Unit: kPa
test
Druck PTX 1830
2867610
0-10 bar a
kPa

CALIBRATION SOURCE PROPERTIES
Type/Producer: Pressurements deadweight tester P3023-6-P
SN: 66611
Uncertainty [%]: 0.008

POLY FIT EQUATION:
Y= -9.24361982E+0X^0 + 24.71024924E+3X^1

CALIBRATION SUMARY:
Max Uncertainty : 0.065591 [%]
Max Uncertainty : 0.030638 [kPa]
RSQ : 1.000000
Calibration points : 28

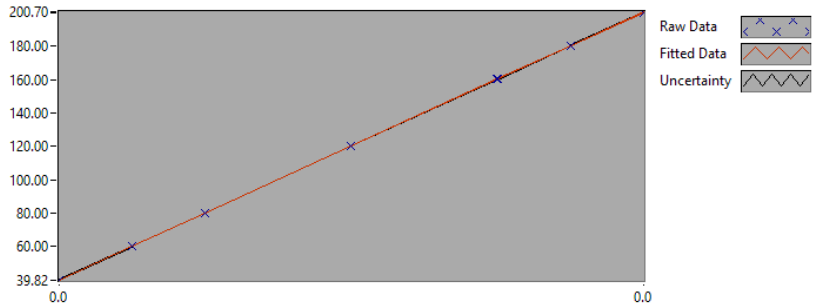

Figure 1 : Calibration chart (The uncertainty band is multiplied by 10)

Gine Kirkebøen Støren

CALIBRATION VALUES

Value [kPa]	Voltage [V]	Best Poly Fit [kPa]	Deviation [kPa]	Uncertainty [%]	Uncertainty [kPa]
40.091214	0.002000	40.166138	-0.074924	0.065540	0.026276
60.121428	0.002809	60.162424	-0.040996	0.037472	0.022529
80.151643	0.003618	80.168618	-0.016976	0.024502	0.019638
120.212071	0.005239	120.211063	0.001008	0.014994	0.018025
160.272499	0.006861	160.285807	-0.013308	0.014078	0.022563
180.302714	0.007672	180.333712	-0.030998	0.014601	0.026327
200.332928	0.008484	200.389684	-0.056756	0.015293	0.030638
200.332928	0.008484	200.389679	-0.056752	0.015293	0.030637
180.302714	0.007672	180.330916	-0.028202	0.014601	0.026327
160.272499	0.006860	160.271571	0.000928	0.014076	0.022560
120.212071	0.005238	120.190559	0.021512	0.014994	0.018024
80.151643	0.003617	80.139696	0.011946	0.024506	0.019642
60.121428	0.002808	60.130686	-0.009258	0.037479	0.022533
40.091214	0.001998	40.129761	-0.038547	0.065566	0.026286
40.091214	0.001998	40.129598	-0.038384	0.065566	0.026286
60.121428	0.002807	60.117965	0.003463	0.037486	0.022537
80.151643	0.003616	80.120344	0.031299	0.024511	0.019646
120.212071	0.005237	120.159474	0.052597	0.014994	0.018024
160.272499	0.006859	160.238611	0.033888	0.014074	0.022556
180.302714	0.007670	180.286577	0.016136	0.014597	0.026318
200.332928	0.008482	200.338244	-0.005316	0.015289	0.030628
200.332928	0.008482	200.338245	-0.005317	0.015289	0.030628
180.302714	0.007670	180.277595	0.025118	0.014597	0.026318
160.272499	0.006858	160.227665	0.044834	0.014072	0.022553
120.212071	0.005236	120.146297	0.065774	0.014993	0.018024
80.151643	0.003615	80.094229	0.057414	0.024514	0.019648
60.121428	0.002806	60.083049	0.038379	0.037496	0.022543
40.091214	0.001996	40.079780	0.011434	0.065591	0.026296

COMMENTS:

The uncertainty is calculated with 95% confidence. The uncertainty includes the randomness in the calibrated instrument during the calibration, systematic uncertainty in the instrument or property which the instrument under calibration is compared with (dead weight manometer, calibrated weights etc.), and due to regression analysis to fit the calibration points to a linear calibration equation.The calculated uncertainty can be used as the total systematic uncertianty of the calibrated instrument with the given calibration equation.

CALIBRATION REPORT

CALIBRATION PROPERTIES
Calibrated by: Gine Kirkebøen Støren
Type/Producer: Kulite HEM-375
SN: 6293-6A-410
Range: 0-1,7 bar a
Unit: kPa
test
Druck PTX 1830
2867610
0-10 bar a
kPa

CALIBRATION SOURCE PROPERTIES
Type/Producer: Pressurements deadweight tester P3023-6-P
SN: 66611
Uncertainty [%]: 0.008

POLY FIT EQUATION:
Y= -4.59067954E+0X^0 + 24.70672968E+3X^1

CALIBRATION SUMARY:
Max Uncertainty : 0.045810 [%]
Max Uncertainty : 0.024170 [kPa]
RSQ : 1.000000
Calibration points : 28

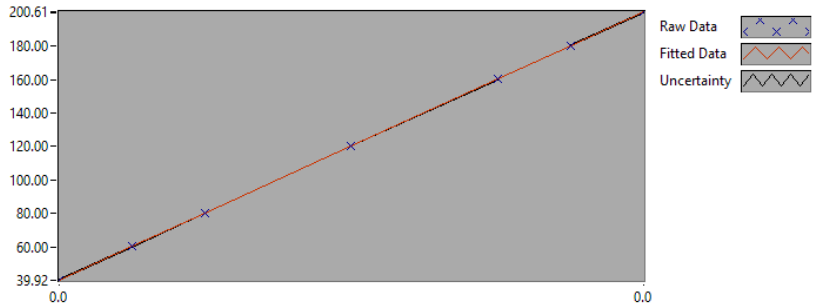

Figure 1 : Calibration chart (The uncertainty band is multiplied by 10)

Gine Kirkebøen Støren

CALIBRATION VALUES

Value [kPa]	Voltage [V]	Best Poly Fit [kPa]	Deviation [kPa]	Uncertainty [%]	Uncertainty [kPa]
40.091214	0.001811	40.148430	-0.057216	0.045790	0.018358
60.121428	0.002620	60.145898	-0.024470	0.026607	0.015996
80.151643	0.003430	80.157576	-0.005934	0.017933	0.014374
120.212071	0.005051	120.203469	0.008602	0.011885	0.014287
160.272499	0.006673	160.279223	-0.006724	0.011332	0.018163
180.302714	0.007484	180.325570	-0.022857	0.011647	0.020999
200.332928	0.008296	200.366961	-0.034034	0.012065	0.024170
200.332928	0.008296	200.366875	-0.033947	0.012064	0.024169
180.302714	0.007484	180.310055	-0.007342	0.011646	0.020999
160.272499	0.006672	160.259102	0.013398	0.011332	0.018162
120.212071	0.005050	120.178967	0.033104	0.011885	0.014287
80.151643	0.003429	80.126190	0.025453	0.017937	0.014376
60.121428	0.002619	60.119787	0.001642	0.026610	0.015999
40.091214	0.001810	40.121437	-0.030223	0.045799	0.018362
40.091214	0.001810	40.121649	-0.030435	0.045799	0.018361
60.121428	0.002619	60.122212	-0.000784	0.026613	0.016000
80.151643	0.003429	80.129074	0.022568	0.017935	0.014375
120.212071	0.005050	120.174789	0.037282	0.011884	0.014286
160.272499	0.006672	160.253668	0.018831	0.011331	0.018161
180.302714	0.007484	180.302950	-0.000236	0.011646	0.020999
200.332928	0.008295	200.350371	-0.017443	0.012064	0.024168
200.332928	0.008295	200.350283	-0.017356	0.012064	0.024167
180.302714	0.007483	180.296993	0.005720	0.011645	0.020996
160.272499	0.006672	160.241886	0.030613	0.011331	0.018161
120.212071	0.005050	120.166348	0.045723	0.011884	0.014286
80.151643	0.003428	80.110961	0.040681	0.017957	0.014393
60.121428	0.002618	60.102741	0.018688	0.026620	0.016004
40.091214	0.001809	40.104523	-0.013308	0.045810	0.018366

COMMENTS:

The uncertainty is calculated with 95% confidence. The uncertainty includes the randomness in the calibrated instrument during the calibration, systematic uncertainty in the instrument or property which the instrument under calibration is compared with (dead weight manometer, calibrated weights etc.), and due to regression analysis to fit the calibration points to a linear calibration equation.The calculated uncertainty can be used as the total systematic uncertianty of the calibrated instrument with the given calibration equation.

Appendix - D

Operating procedure

FO-04 - Procedure for operating the Francis turbine test rig - Semi-closed loop

? Ukjent vedlegg

Doc No:	Date: 14.10.2020	Classification: Open
Prepared by: Johannes Kverno	Approved by:	

Procedure for operating the Francis turbine test rig - Semi-closed loop

1 General

This procedure describes how the Francis turbine test rig is operated in a semi-closed loop. The water is pumped directly from the lower reservoir and into the pressure tank, from there through the turbine and to the draft tube tank and back to the lower reservoir.

1.1 Definitions and abbreviations

Abbreviation	Definition
HMI	Human machine interface
SCADA	Supervisory control and data acquisition
PLC/PLS	Programmable logic controller / Programerbar logisk styring
IGSS	A SCADA system for process control and supervision

2 The system

2.1 Description

The system in use is the Francis turbine test rig. It has a number of calibrated instruments connected to a data acquisition system, and a computer program written in LabVIEW records the data and performs all necessary calculations.
All calculations are performed according to IEC 60193. The Francis turbine test rig can be set up in different modes with various pressure, flow, generator rotational speed and guide vane angle. See FO-03 or FO-05 for other configuration modes.

3 Operation

3.1 Setting up the pipe system for a semi-closed loop

3.1.1 Setting up the system

Valves	Status
V4, To sump *(Do not open!)*	Closed
V12, Main valve from sump	Open
V18, Secondary valve from sump	Open
V13, Inlet pump 1	Open
V14, Inlet pump 2 *(Do not close!)*	Open
V5, Inlet pressure tank	Open
V6, To attic	Closed
V7, From attic	Open
V8, To pressure tank	Closed
V9, Francis turbine inlet	Open
V3, After draft tube tank	Open*
V2, Draft tube tank to weigh tank	Open
V27, Remote controlled draft tube tank bleed valve	Closed
V29, Auxiliary rigs valve	Closed
V18, Manual bleed valve on the pressure tank, *See picture 1a*	Open
Manual valve after the draft tube tank	Open
Other manual valves along the waterway	Closed

*For ordinary operation with atmospheric pressure in the draft tube tank.

3.1.2 Setting up for the pump to be used

Pump 1

Valve	Status
V15, Outlet pump 1	Open
V16, Pump 2 out Pump 1 in	Closed
V17, Outlet pump 2	Closed

Pump 2

Valve	Status
V15, Outlet pump 1	Closed
V16, Pump 2 out Pump 1 in	Closed
V17, Outlet pump 2	Open

3.2 Preparing the rig and filling the system

3.2.1 Setting up the system

1. Open for cooling water to the hydraulic system. *See picture 1b*
2. Start the hydraulic system. Check that the pressure gauges show the correct pressures, refer to the pressures written down above the gauges. *See picture 1c*
3. Turn on the ventilation fans (avtrekksvifte). *See picture 1d*
4. Turn on the frequency drive for the pump to be used. This is done in the basement. Turn the switch to *Start* and hold it there for a couple of seconds, then release it and leave the switch at position *1*. *See picture 1e*
5. Ensure that the bleed valve on the pressure tank is open. *See picture 1a*
6. Close the draft tube tank pump outlet valve. *See picture 1f*
7. Open the bleed valve (red handle) on the draft tube tank. *See picture 1g*
8. Close the drainage valve (black handle) on the draft tube tank. *See picture 1g*
9. Inspect the upper cover on the turbine for any foreign objects or tools that might interfere with the guide vane control.

3.2.2 Starting the pump and filling the pressure tank

1. Check that the waterway and valves are set up correctly, as described in 3.1.
2. Close the guide vanes as much as they can be.
3. Start the pump you've configured for at 100 RPM and increase the speed with a few increments to 330 RPM to start filling the pressure tank. With 330 RPM minimal flow through the turbine rig the tank should fill to the correct level, (marked by a line on the surveillance monitor). There will be some flow through the turbine though, as the guide vanes can't fully seal.
4. While waiting for the tank to fill up, check the pump seals in the basement. There should be at least one drop every 20 seconds, and no excessive continuous flow. If in doubt contact one of the lab technicians. The water cools the seal packings. *See picture 1m*
5. Once the level is correct, close the bleed valve on top of the pressure tank.

3.2.3 Filling the turbine

1. Increase the pump to by ~50RPM to increase the inlet pressure.
2. Open the guide vanes by a couple of degrees to start filling the draft tube tank.
3. Check the generator torque setpoint. Should be between 1000Nm and 1500NM and ensure that it's not a negative number. This is critical!
4. Make sure that the generator is set to **Turbine mode** and **not** pump mode. This is also critical.
5. If the turbine is not spinning, open the guide vanes until it does. Then set the setpoint RPM to be within ±4RPM of the actual speed of rotation.
6. Start the generator once the speeds are matched close enough.
7. Open the guide vanes to 9-10 degrees to expedite the filling of the draft tube tank.

3.2.4 Bleeding the system

1. Open the bleed valve to the inlet pipe (next to the metal stair case) and keep open until no more air is coming. *See picture 1h*
2. Close the drainage valve on the underside of the inlet pipe, if it hasn't already been closed. *See picture 1i*
3. Open the bleed valve on the plenum chamber above the rig. Wait until only water exits. It is a good idea to shake the hoses coming from the inlet pipe to get rid of bubbles that might be stuck inside them. *See picture 1j*
4. Close the draft tube tank bleed valve (red handle) when the level is between the two black tape marks on the level gauge.
5. Open the water tap valve to the differential pressure sensor. *See picture 1k*
6. Open the valves 1 and 3, keep them open for about 30 seconds and then close them. You can give the hoses going towards the draft tube a wiggle as well. *See picture 1l*
7. Open the valves 2 and 4 and keep them open for about 30 seconds. *While valve 4 is open, wiggle the inlet pressure sensor and hose a bit to try to get any trapped air out of the horizontal branch from the T-joint.*
8. Close the water tap valve to the differential pressure sensor.
9. Check for any water or oil leaks on top of the turbine cover.
10. Check the pump seals in the basement again, as done in 3.2.2 point 4. This should be repeated once or twice per hour during the operation/test to ensure that the seals are sufficiently cooled.

3.3 Run the test/procedure

Adjust the pump speed to get to the inlet pressure.

Some tests or procedures will require you to change certain steps and/or add additional equipment. How this is done should be mentioned in that test/procedure.

3.4 Shut down and draining

3.4.1 Stopping the generator

1. Reduce the pump RPM to somewhere between 330 and 430 RPM to reduce the pressure at the inlet.
2. Close the guide vanes as required to reduce the generator torque.
3. Stop the generator when the average torque is oscillating around 0Nm. ±50Nm is fine.

3.4.2 Draining the pressure- and draft tube tanks

1. Reduce the pump RPM to 330.
2. Close the guide vanes further. Keeping them between 0,5° and 1° will speed up the draining of the spiral casing without spinning the runner too much.
3. Check that the pressure in the pressure tank *PT8* is ~0mvs, and if it is open the manual bleed valve (V18) on top of it.
4. Reduce the pump speed to 100 RPM.
5. Open the inlet pipe bleed valve.
6. Open the drainage valve on the underside of the turbine inlet pipe.
7. Open the draft tube tank pump outlet valve half way to start draining the tank. *(Picture)*
8. Open the draft tube tank bleed valve (red handle) fully, and the drainage valve (black handle) half way.
9. Check the level of the pressure tank, and if it is below ~30%, stop the pump.
10. Open the guide vanes by a degree or two to speed up the draining even more.

3.4.3 Shutting down

1. Turn off the hydraulic system and the cooling water for the hydraulic system once the spiral casing is mostly drained and the runner has stopped rotating.
2. Turn off the pump frequency drive in the basement.
3. Do an inspection round in the basement and the lab.
4. Turn off the ventilation fans (*avtrekksvifte*).

4 Figures

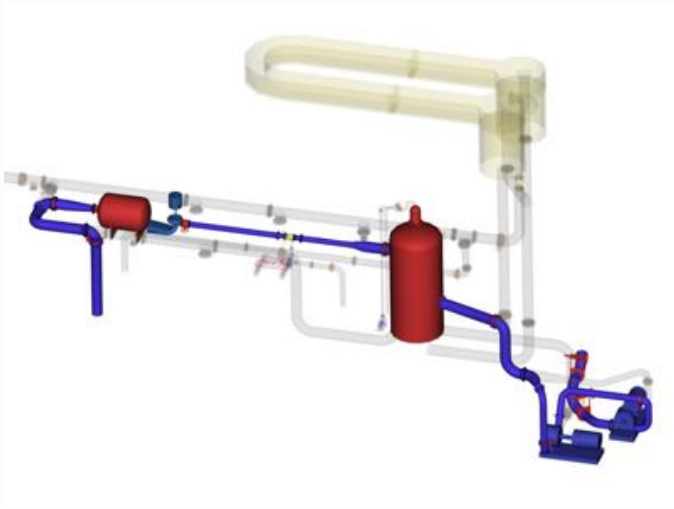

Figure 1: 3D representation of a semi-closed loop configuration

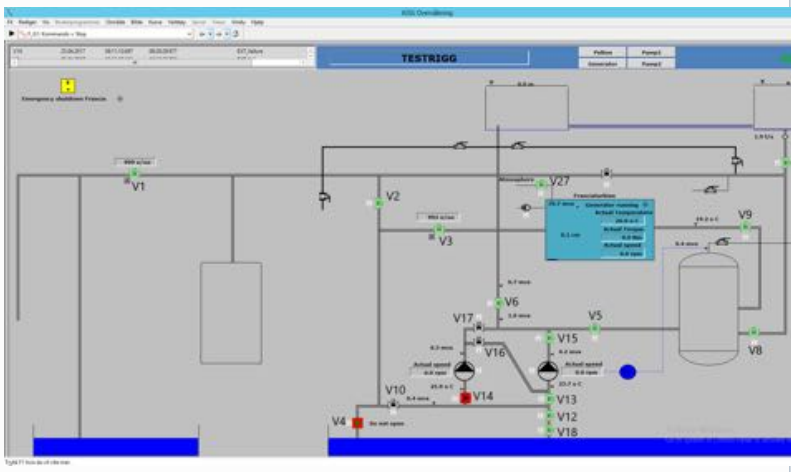

Figure 2: Overview of valves from the IGSS program on the computer in the control room

1a - Bleed valve on the pressure tank (V18)

1b - Water tap for the hydraulic system cooling water

1c - Hydraulic pump unit and pressure dials

1d - Ventilation fan switch

1e - Pump frequency drive and power switch

1f - Draft tube tank pump outlet valve

1g - Draft tube tank bleed- and drain valves

1h - Inlet (and outlet) pipe bleed valve

1i - Inlet pipe draining valve

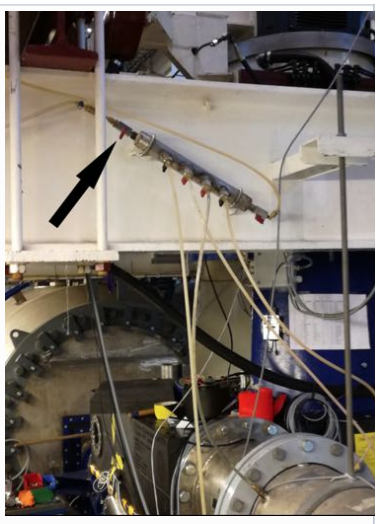

1j - Inlet pipe pressure manifold

1k - Water tap to prime the differential pressure tansducer

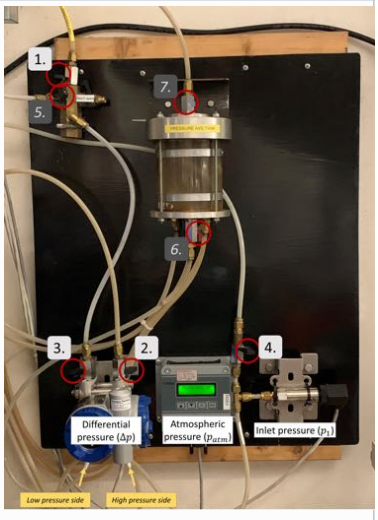

1l - Pressure transducers and bleeding valves

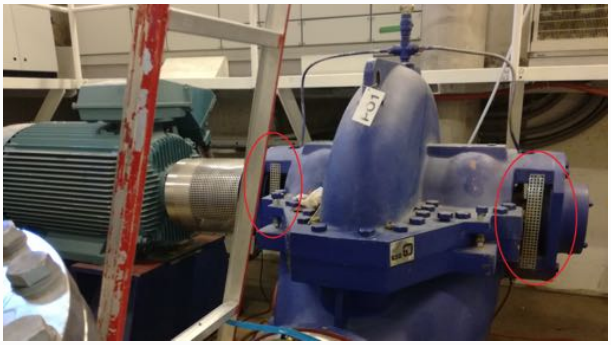

1m - Pump seal

5 References

- IEC 60193

Version	Date	Author	Comment
5	20.10.20	Johannes Opedal Kverno	Added pictures to the procedure
4	15.10.20	Johannes Opedal Kverno	
3	15.10.20	Johannes Opedal Kverno	Final touches to the procedure. Pictures still missing though.
2	15.10.20	Johannes Opedal Kverno	
1	15.10.20	Johannes Opedal Kverno	

Appendix - E

Risk assessment

NTNU SINTEF

VEDLEGG E: FORSØKSPROSEDYRE

	Dato/Signatur
Apparatur FRANCIS riggen	
Prosjektleder Ole Gunnar Dahlhaug	15/10-20 Ole G Dahlhaug

	Conditions for the experiment:	**Completed**
	Experiments should be run in normal working hours, 08:00-16:00 during winter time and 08.00-15.00 during summer time. Experiments outside normal working hours shall be approved.	
	One person must always be present while running experiments, and should be approved as an experimental leader.	
	An early warning is given according to the lab rules, and accepted by authorized personnel.	
	Be sure that everyone taking part of the experiment is wearing the necessary protecting equipment and is aware of the shut down procedure and escape routes.	
	Preparations	**Carried out**
	Post the "Experiment in progress" sign.	
	Start up procedure	
	During the experiment	
	Control of temperature, pressure	
	End of experiment	
	Shut down procedure	
	Remove all obstructions/barriers/signs around the experiment.	
	Tidy up and return all tools and equipment.	
	Tidy and cleanup work areas.	
	Return equipment and systems back to their normal operation settings (fire alarm)	
	To reflect on before the next experiment and experience useful for others	
	Was the experiment completed as planned and on scheduled in professional terms?	
	Was the competence which was needed for security and completion of the experiment available to you?	
	Do you have any information/ knowledge from the experiment that you should document and share with fellow colleagues?	

Operatører

Navn	Dato	Signatur
Gine Kirkebøen Støren	15/10-2020	Gine K. Støren

NTNU SINTEF

VEDLEGG F: OPPLÆRINGSPLAN FOR OPPERATØRER

	Dato/Signatur
Apparatur FRANCIS riggen	
Prosjektleder Ole Gunnar Dahlhaug	15/10 20

	Kjennskap til EPT LAB generelt	
	Lab - adgang -rutiner/regler -arbeidstid	
	Kjenner til evakueringsprosedyrer	
	Aktivitetskalender	
	Innmelding av forsøk til: iept-experiments@ivt.ntnu.no	
	Kjennskap til forsøkene	
	Prosedyrer for forsøkene - Oppstart av pumpe - Sjekkrunde på forhånd - Oppstart av rigg - Nedkjøring av rigg - Hydraulikkprosedyrer	
	Nødstopp I kontrollrom og ved rigg	
	Bruk av verneutstyr	
	Nærmeste brann/førstehjelpsstasjon	
	Oppstart og kjøreprosedyre foreligger	

Jeg erklærer herved at jeg har gjennomgått og forstått HMS-regelverket, har fått hensiktsmessig opplæring for å kjøre dette eksperimentet og er klar over mitt personlige ansvar ved å arbeide i EPT laboratorier.

Operatører

Navn	Dato	Signatur
Gine Kirkebøen Støren	15/10 - 2020	Gine K. Støren